Jury Member Report – Doctor of Philosophy thesis

Name of Candidate: Anastasiia Merdalimova

PhD Program: Physics

Title of Thesis: Optical Sensors Based On Hollow-Core Microstructured Optical Waveguides: 2-In-1 Multispectral Refractometry And Raman Spectroscopy

Supervisor: Professor Dmitry Gorin
Co-supervisor: Associate Professor Alexey Yashchenok

Name of the Reviewer: Vassili Fedotov

I confirm the absence of any conflict of interest	
	Date: 20-11-2023

The purpose of this report is to obtain an independent review from the members of PhD defense Jury before the thesis defense. The members of PhD defense Jury are asked to submit signed copy of the report at least 30 days prior the thesis defense. The Reviewers are asked to bring a copy of the completed report to the thesis defense and to discuss the contents of each report with each other before the thesis defense.

If the reviewers have any queries about the thesis which they wish to raise in advance, please contact the Chair of the Jury.

Reviewer's Report

Reviewers report should contain the following items:

- Brief evaluation of the thesis quality and overall structure of the dissertation.
- The relevance of the topic of dissertation work to its actual content
- The relevance of the methods used in the dissertation
- The scientific significance of the results obtained and their compliance with the international level and current state of the art
- The relevance of the obtained results to applications (if applicable)
- The quality of publications

The summary of issues to be addressed before/during the thesis defense

This thesis gives an account of an important interdisciplinary research, which led to the development and demonstration of an arguably novel multi-functional optical sensor for bio-fluids based on a microstructured optical fibre. The underlining efforts represent a good amount of work carried out by the candidate, which has already resulted in 4 regular publications (+1 under review) in respected international journals, 1 review paper and 1 book chapter, and 4 oral talks accepted by national and international conferences and workshops. The candidate's work has also led to 1 patent application. The topic of the thesis is largely relevant to the thesis content, which is scientifically significant at both national and international levels. Overall, this is an interesting and, potentially, solid thesis yielding important results that will undoubtedly find applications in life sciences and medicine. However, in its present form the thesis leaves the distinct impression that it was put together in a rush, and therefore, requires a fair amount of mending and revision before it can be accepted for the defence. Below I append a summary of minor and major shortcomings, while the full list of comments, suggestions, recommendations and questions to address can be found in the attached copy of the thesis. The candidate is also invited to better convey the novelty aspect of her work in the thesis.

> Formatting

The titles of some chapters, sections or sub-secton appear at the bottom of a page with no text beneath. In such cases it is better to move them to a new page. Also, some of the titles appear centred, while some – aligned to the left.

Some parts of the thesis use single-line spacing (e.g., list of figures), while most of the thesis is formatted using double-line (or so) spacing.

> Writing style

In some places of the thesis the candidate refers to herself using royal "we". In most of such cases the candidate appear to have copied the relevant passages directly from the papers she co-authored. While "we" is perfectly acceptable for a scientific publication (which is typically authored by more than one person), a thesis can have only one author and so the use of "we" is not appropriate. Hence, my recommendation for the candidate is to re-phrase those passages using passive voice or refer to herself as "the author".

> Clarity

The candidate should explain better why she refers to the technique she has developed and demonstrated as "two-in-one". This term implies that the same setup was used for measuring both the refractive index and SERS signal of an analyte. However, it turns out that the candidate used two different setups for refractive index and SERS measurements. Hence, currently, it is quite difficult to accept that the candidate indeed demonstrated "two-in-one" sensing functionality.

The candidate must be consistent in the use of terminology and abbreviations. For example, the candidate refers to monolayers of gold nanoparticles using at least 3 different terms, namely "coating", "layer" and "substarte". However, using these terms interchangebly for describing monolayers of gold nanoparticles may be quite confusing. Some abbreviation (like RI = refractive index) are introduced several times throughout the thesis, some abbreviations are hardly used, while some are used without proper introduction and, hence, impossible to guess. Rather than introducing abbreviations in the text the candidate should take full advantage of the list of symbols and abbreviations on page 12, which is

currently poorly populated.

> **Content**

A fair chunk of Chapter 2 covers the fabrication of hollow—core microstructure optical waveguides (HC-MOW) in great detail, which, in my view, has absolutely no relevance to the work presented by the candidate. Indeed, her work involved neither the fabrication of such fibres nor the analysis of how different methods of HC-MW fabrication might affect/influence the obtained results. The same applies to the methods of isolation of nanovesicules from plasma covered by Chapter 2. At the same time, microbubbles (which suddenly appear in section 6.2) are missing completely in Chapter 2.

Chapter 3 contains very brief and, at times, vague descriptions of only a handful of methods/techniques/processes with no explanations of what they were used for. Moreover, none of those methods is properly referred to in the investigative chapters (as if they were completely irrelevant). At the same time, quite a number of other methods (e.g., asymmetric depth filtration approach to isolation of extracellular vesicles) are described in the investigative chapters. That begs the question of whether Chapter 3 is really needed, and, perhaps, it would be better/easier to dissolve the content of Chapter 3 in other chapters.

In any case, it would also help if the candidate added a synopsis to Chapters 1-3, which would briefly explain the relevance of the chapters' content to the research carried out by the candidate.

> **Experimental details**

The candidate needs to make sure that her thesis provides all the information required by others to repeat the described experiments and reproduce the reported results. At the moment many experimental details/parameters are either missing or appear too late in the text (see my comments in the attached copy of the thesis). For example, the completed detailed description of HC-MOW – one of the key elements of the developed sensing setup, is nowhere to be found. I would expect to see a whole section (or a sub-section) featuring a schematic of HC-MOWs used, their cross-section showing the pattern of the cladding, key dimension of the fibre and the pattern of the cladding, description of the material it was made of etc.

> **Plagiarism**

Some sub-sections (in particular, 2.1.2, 2.1.4, 2.2.2, 6.3.1, 7.1.2) are seemingly better composed and feature better English than others, which suggests that the text there was copied by the candidate from published sources. While self-plagiarism (i.e., the use of text from the publications co-authored by the candidate) is acceptable, the instances of plagiarism (i.e., the use of text from the publications of other groups) must be avoided all together, for example, by paraphrasing the respective sections of text.

> **Citing candidate's own papers**

The candidate does not have to and, in fact, should not refer to her published papers in the thesis (as if they represent the sources of additional information). This thesis is not a review of the candidate's own publications – it is the primary source of information for the work the candidate did in the course of her postgraduate research. The thesis is, in fact, expected to provide a much more detail account of the candidate's research than the papers she co-authored.

While it is very good that the candidate has managed to publish her work in a number of peer-reviewed

journals by now, that did not have to be the case. Hence, I recommend the candidate to provide at the beginning of each chapter a list of relevant papers she co-authored (e.g., like she has done so far) but, otherwise, treat her thesis as a **self-contained** (and the only) source of information on her research, pretending that her work has not been published. Correspondingly, rather than referencing her papers in the thesis, the candidate should refer to relevant chapters/sections instead.

> Figures

Since one's thesis should not be a review of one's own publications, I expect the candidate to use her original plots and diagrams (i.e., created by her) in the thesis rather than re-productions from her published papers. In this case the candidate does not need to refer to her publications in figure captions, state that they were reproduced and seek permission from the publisher for the reproduction. Moreover, this will also enable the candidate to re-arrange panels in the way that allows each figure to better fit the page, as well as change fonts in those (many) cases, when numbers and notations in the reproduced figures are too small to read (e.g., Figure 2-7).

Surprisingly, this thesis contains quite a few figures reproduced from papers published by other groups. Since one's thesis (in first place) is a testament to one's personal contribution to a particular field of science, the inclusion of that many figures from someone else's work must be justified/clearly explained. Also, in all such cases, the candidate needs to obtain copyright permissions from the publishers of those works and include the statement of permission and copyright notice (as it is done for Figure 2-3).

Provisional Recommendation

☐ *I recommend that the candidate should defend the thesis by means of a formal thesis defense*

☒ *I recommend that the candidate should defend the thesis by means of a formal thesis defense only after appropriate changes would be introduced in candidate's thesis according to the recommendations of the present report*

☐ *The thesis is not acceptable and I recommend that the candidate be exempt from the formal thesis defense*

Skolkovo Institute of Science and Technology

OPTICAL SENSORS BASED ON

HOLLOW-CORE MICROSTRUCTURED OPTICAL WAVEGUIDES:

2-IN-1 MULTISPECTRAL REFRACTOMETRY AND RAMAN SPECTROSCOPY

Doctoral Thesis

by

ANASTASIIA MERDALIMOVA

DOCTORAL PROGRAM IN PHYSICS

Supervisor
Prof. Dr. Dmitry Gorin
Co-supervisor
Prof. Dr. Alexey Yashchenok

Moscow - 2023

I hereby declare that the work presented in this thesis was carried out by myself at Skolkovo Institute of Science and Technology, Moscow, except where due acknowledgement is made, and has not been submitted for any other degree.

Anastasiia Merdalimova (Candidate)

Prof. Dmitry Gorin (Supervisor)

Abstract

Early diagnostics on biological liquids is one of the most prioritized topics in modern biomedical research, such as early diagnostics of cancer, as it allows for a better prognosis for the patient. Several objects can be chosen as biomarkers for early diagnostics, such as specific proteins and circulating tumor DNA, circulating tumor cells or the recently discovered extracellular vesicles. Extracellular vesicles are nanosized objects with a lipid bilayer and containing proteins and nucleic acids from the parental cells, that are released by cells and may be found in diverse biological liquids. The disease-specific extracellular vesicles appear in a bloodstream earlier and in a higher concentration that circulating tumor cells, and can provide more multifaceted information about the parental cell than single molecules. Thus, extracellular vesicles are perspective for early diagnostics.

However, their utilization require instrumentation for their isolation from biological liquids, and then detection and/or analysis. For that, their feature of a complex structure becomes a disadvantage, raising a need for a sensor capable to handle such type of objects.

To address this issue, the goal of the present project is to explore hollow-core microstructured optical waveguide (HC-MOW) opportunities for multifaceted characterization of complex fluids. In particular, the examples of such fluids used in the work are macromolecule structures as model analytes and then extracellular vesicles. HC-MOW possess a unique optical structure for light waveguiding, than can be used as a multiwavelength refractive index sensor, Raman scattering sensor and other. Previously these sensing modalities were explored separately, and the goal of the present project is reached by using combinations of several sensing modalities in the HC-MOW. Namely, it's implemented in the following ways: SERS substrate fabrication and the corresponding layer deposition control in HC-MOW; and 2-in-1 multispectral refractometry and Raman spectroscopy for complex macromolecular objects, namely protein-copolymer complexes and microbubbles and the finally extracellular vesicles.

Initially, it was shown that compared to measuring a larger volume drop on a planar substrate, the use of HC-MOW allows to increase the intensity of the observed Raman

3

scattering with a lower probe volume used, and different analytes provide different intensity improvement (fiber enhancement). This fiber-enhanced Raman is then combined with other sensing techniques. The first of these is building a SERS substrate in the HC-MOW, providing SERS sensing and layer deposition control during fabrication. However, the developed SERS sensing in HC-MOW didn't demonstrate a significant enhancement compared to previously reported values and turned out to be not that stable in liquid solution. The method of 2-in-1 multispectral refractometry and Raman spectroscopy demonstrated to be more promising, with linear dependencies of Raman peak intensity and refractive index on concentration and their sensitivities estimated, and an upper detection limit for highly scattering microbubbles was found.

These findings lead to a perspective of using HC-MOW for diagnostics on biological liquids for diagnostic needs. Moreover, it can be used for characterization of ultrasound contrast agents in real-time, specifically of protein-copolymer microbubbles and their parent complexes.

Publications

Research articles

1. **A.A. Merdalimova**, P.G. Rudakovskaya, T.I. Ermatov, A.S. Smirnov, S.S. Kosolobov, J.S.Skibina, P.A. Demina, B.N. Khlebtsov, A.M. Yashchenok, D.A. Gorin, SERS Platform Based on Hollow-Core Microstructured Optical Waveguide: Technology of UV-Mediated Gold Nanoparticle Growth. Biosensors, 2022, 12, 19. https://doi.org/10.3390/bios12010019 (IF=5.519, Q1)
Author's contribution: Research methodology, providing measurements, data analysis, manuscript writing

2. J. Cvjetinovic, **A. A. Merdalimova**, M. A. Kirsanova, P. A. Somov, D. V. Nozdriukhin, A. I. Salimon, A. M. Korsunsky and D. A. Gorin, A SERS platform based on diatomite modified by gold nanoparticles using a combination of layer-by-layer assembly and a freezing-induced loading method. Phys. Chem. Chem. Phys., 2022,24, 8901-8912. https://doi.org/10.1039/d2cp00647b (IF 3.7, Q1)
Author's contribution: SERS spectroscopy, writing corresponding chapters

3. M.A. Slyusarenko, N.S. Nikiforova, E. I. Sidina, I.V. Nazarova, V.V. Egorov, Y.P. Garmay, **A.A. Merdalimova**, N.P. Yevlampieva, D.A. Gorin, A.V. Malek, Formation and evaluation of a two-phase polymer system in human plasma as a method for extracellular nanovesicle isolation. Polymers (Basel), 2021, 13(3):1–16. https://doi.org/10.3390/polym13030458 (IF=3.426, Q1)
Author's contribution: Raman spectroscopy, nanoparticle tracking analysis, writing a corresponding paragraph

4. V.Chernyshev, R.Chuprov-Netochin, E.Tsydenzhapova, E.Svirshchevskaya, R.Poltavtseva, **A.Merdalimova**, A.Yashchenok, A.Keshelava, K.Sorokin, V.Keshelava, G.Sukhikh, D.Gorin, S.Leonov, M.Skliar. Asymmetric depth-filtration: A versatile and scalable method forhigh-yield isolation of extracellular vesicles with low contamination. Journal of Extracellular Vesicles, 11, e12256. https://doi.org/10.1002/jev2.12256 (IF 17.3, Q1)
Author's contribution: Raman spectroscopy, writing a corresponding paragraph

5. **A. Merdalimova**, V. Vorobev, R. Barmin, A.Aleksandrov, D. Terentyeva, T. Estifeeva, S. German, V. Chernyshev, O. Maslov, Y. Skibina, P.Rudakovskaya, D. Gorin, Two-in-One Sensor of Refractive Index and Raman Scattering using Hollow−Core Microstructured Optical Fibers for Colloid Characterization. Colloids and Surfaces B, 2023 (under revision, submission number COLSUB-D-23-02310)

   Author's contribution: Research methodology, providing measurements, data analysis, manuscript writing

Review article & book chapter

1. **A.A. Merdalimova**, V.V. Chernyshev, D. Nozdriukhin, P. Rudakovskaya, D. Gorin, A. Yashchenok, Identification and Analysis of Exosomes by Surface-Enhanced Raman Spectroscopy. Applied Sciences-Basel, 9,6,2019, 1135. https://doi.org/10.3390/app9061135 (IF=2.217, Q2)

2. **A. Merdalimova**, V. Vorobev, A. Zanishevskaya, S.Perevoschikov, A.Aleksandrov, P.Rudakovskaya, Y. Skibina, V. Tuchin, D. Gorin, Hollow-core microstructured optical fibers and their applications for biosensing. A chapter in a book "Specialty Optical Fibers", Elsevier, 2023 (under revision)

Patent

1. A. Yashchenok, V. Chernyshev, P. Rudakovskaya, **A. Merdalimova**, V. Shipunova, A. Schulga, S.Deev, D. Gorin. Nano- and microparticles for isolation of specific exosome subpopulations and their analysis. № RU2733884

Participation in scientific conferences

1. **A.Merdalimova**, A.Yashchenok, D.Gorin, "Application of Raman spectroscopy to exosomes: approaches and challenges", European Biosensor Symposium - Digital Seminar Series: Seminar on Raman-based Biosensors, headed by Leibniz Institute of Photonic Technology Jena, Germany, 2021 (oral talk)

2. **A.Merdalimova**, V.Chernyshev, R.Chuprov-Netochin, D.Gorin, "In vitro study of exosome secretion rate by nanoparticle tracking analysis", "Saratov Fall Meeting-2020" - VIII Symposium on Optics & Biophotonics, 2020 (oral talk)

3. **A. Merdalimova**, R. Barmin, V. Vorobev, D. Terentyeva, T. Estifeeva, S. German, V. Chernyshev, O. Maslov, Y. Skibina, P.Rudakovskaya, D. Gorin, Optical Sensors Based on Hollow-Core Microstructured Optical Waveguides, 17th International conference on Laser Applications in Life Sciences, 2023 (oral talk) – accepted, the event expected October 15-17th 2023

4. **A. Merdalimova**, R. Barmin, V. Vorobev, D. Terentyeva, T. Estifeeva, S. German, V. Chernyshev, O. Maslov, Y. Skibina, P.Rudakovskaya, D. Gorin, Two-in-One Optical Sensors Based on Hollow-Core Microstructured Optical Waveguides, Dianov's All-Rusian Conference on Fiber Optics 2023 (oral talk) – accepted, the event expected October 3-6th 2023

Acknowledgements

Table of Contents

11

List of Symbols, Abbreviations

AuNP, GNP – Gold Nanoparticles

BSA – Bovine Serum Albumin

EV – Extracellular Vesicles

HC-MOW – Hollow-Core microstructured Optical Waveguide

MB – Microbubble

SEM – Scanning Electron Microscopy

P(VP-AA) − copolymer of poly (N−vinylpyrrolidone−*co*−acrylic acid)

TEM – Transmission Electron Microscopy

List of Figures

16

List of Tables

Chapter 1. Introduction

Diagnostics in the early stages of diseases, especially cancer, is a critical area of research in biomedicine. Biomarkers in biological fluids, such as proteins, circulating tumor cells, and extracellular vesicles (EV) have been investigated as potential indicators for early disease detection[1,2]. Discovered only a few decades ago, EV are nanosized structures consisting of a lipid bilayer containing proteins and nucleic acids derived from cells. They are released into various biological fluids and provide valuable information about the parent cells by the proteins and nucleic acids they have received from the parent cells[3–6]. Compared to circulating tumor cells, disease-specific EVs appear earlier and at higher concentrations, making them promising candidates for early diagnostics[7]. However, the effective utilization of EVs for diagnostic purposes requires suitable instrumentation for their isolation, detection, and analysis, given the intricacies of their complex structure[8,9]. This makes their complex structure a disadvantage, so a sensor capable of handling this type of object is needed. Multimodal sensing for multifaceted liquid object characterization may be beneficial not only for EV, but also for other biological objects and complex synthesized structures.

Microstructured optical waveguides (HC-MOW) [10] are axis-symmetrical structures providing waveguiding on either photonic bandgap or inhibited coupling effect[11,12] – the phenomena depends on inner wall thickness. Our scope of interest is in the inhibited-coupling HC-MOW. Due to the provided light guiding as in the Fabri-Perot resonator[13], these waveguides may be used in a number of ways, as presented in: for multiwavelength refractive index [14], absorption on inner walls[14,15], Raman[16–18] and SERS (Surface Enhanced Raman Scattering)[15,19,20] sensing. A number of HC-MOW applications for sensing are known, including sensing of biological objects[21–23], inter alia extracellular vesicles[24].

The goal of the present project is to explore hollow-core microstructured optical waveguide (HC-MOW) opportunities for multifaceted characterization of complex fluids.

19
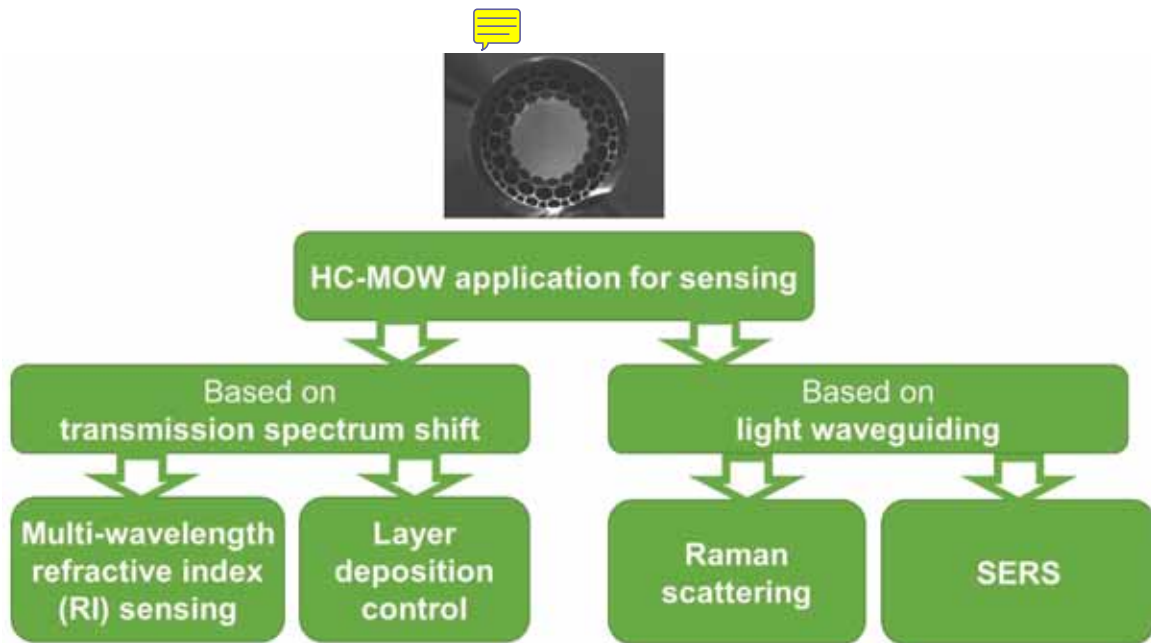
Figure 1-1. Hollow-core microstructured optical waveguides (HC-MOW) applications for sensing considered in the present work

Previously, the exploration of these sensing modalities used to be separate. This project explores the potential for integrating various sensing modalities using antiresonant HC-MOW, with the goal of enabling comprehensive characterization of complex fluids. The novelty of combination of several sensing modalities in HC-MOW to analyze complicated liquid analytes is suggested in the following way. SERS substrate fabrication and the corresponding layer deposition control in HC-MOW; and 2-in-1 multispectral refractometry and Raman spectroscopy for complex macromolecular objects, specifically protein-copolymer complexes/microbubbles and extracellular vesicles. The extracellular vesicles are taken because of their perspectivity for diagnostics, meanwhile protein-copolymer complexes and microbubbles made of them are, from one hand, models of biological solutions, and from another hand the microbubbles are used as ultrasound contrast agents and may benefit from a robust way of their real-time characterization. Thus, the potential of HC−MOW for diagnostic needs is estimated.

Therefore, the project tasks are the following:

1) To estimate the applicability of the present HC-MOW for improved Raman spectroscopy;

2) To implement SERS in HC-MOW, combining the Raman sensing capabilities with layer deposition control;

3) To estimate 2-in-1 refractive index and Raman sensing capabilities for protein-copolymer complexes and microbubbles;

4) To assist extracellular vesicles isolation using Raman spectroscopy;

5) To apply the developed 2-in-1 refractive index and Raman sensing for extracellular vesicles.

This set of tasks leads to the following thesis structure: Chapter 2 provides literature review on HC-MOW, their present and perspective applications, as well as determines the gap in using HC-MOW for extracellular vesicles sensing. The next chapters are experimental, supported by Chapter 3 describing the methods used in the work, initially explored, schematically summarizes analytical methods used for sensing in the present work with particular analytes they are applied to, thus describing visually what is discussed in future chapters. Chapter 4 provides invesigation of Raman scattering in HC-MOW, which benefits from light confinement and waveguiding, resulting in fiber-enhanced Raman spectroscopy (FERS). In the present work, Raman scattering was initially explored on bulk media, specifically solutions of the Raman-active dye Rhodamine 6G (R6G) [25] and protein BSA[26], to demonstrate FERS and compare performance across disparate liquids. Drawing from the results of Chapter 4, this study considers two avenues for combined sensing modalities in HC-MOW are considered. First, Chapter 5 describes the development of SERS substrate in HC-MOF [25], benefiting both from fiber enhancement and the capability to control layer deposition. Secondly, Chapter 6, and Chapter 7 detail two-in-one sensing of multispectral refractive index and Raman scattering
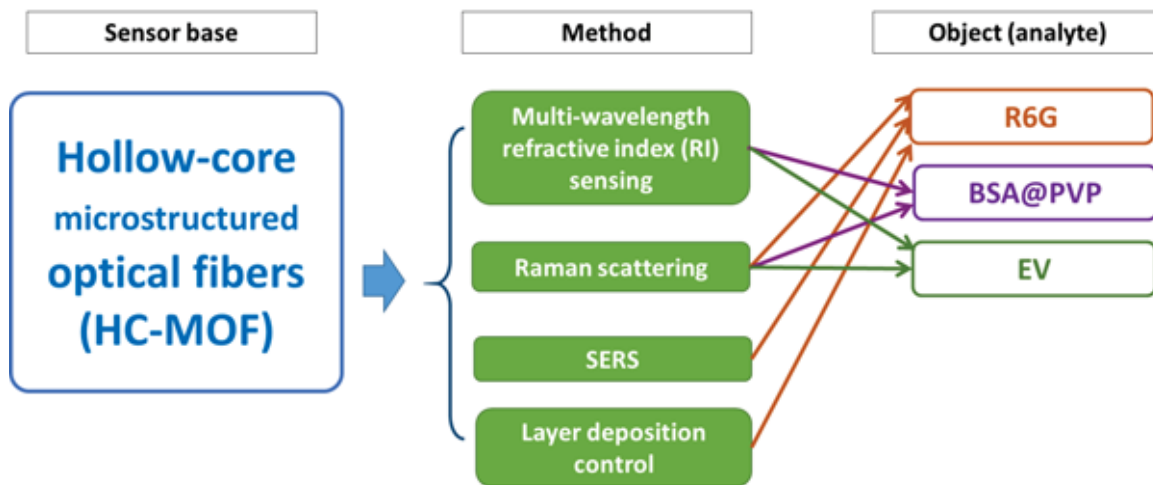
Figure 1-2. Combinations of analytical methods and analytes used in the experimental part of the present work

of liquids in HC-MOW[27], that is of interest for multicomponent systems with complex spectra. Chapter 6 demonstrates this 2-in-1 sensing on protein-copolymer complexes, and Chapter 7, namely paragraph 7.2, leads to sensing extracellular vesicles, preceded by paragraph 7.1 describing Raman spectroscopy application for extracellular vesicles isolation.

Chapter 2. Literature review

2.1. Hollow-core microstructured optical waveguides (HC-MOW)

2.1.1. HC-MOW work principle and classification

Microstructured optical waveguides (MOWs) is a novel class of optical fibers developed in the 1990s. Here, the light is guided through a complex microstructure, which in most cases contains air channels running along the entire waveguide length [28]. According to the structural architecture, MOWs may be classified to solid-core (SC) and hollow-core (HC) MOW. Meanwhile light guiding in a core of a SC-MOW may be based on conventional total internal reflection, as the core possesses a RI greater than cladding structures, it is not the case for HC-MOWs, as here the core is air or filled by gas or liquid, that implies a refractive index typically lower than surrounding glass. The light propagation in the core of HC-MOW depends on modes allowed for propagation in the cladding, which

22

in their turn in fact depend on the first inner wall thickness: in case of wall with thickness up to 150 nm, the mechanism is photonic bandgap (PBG) guiding; otherwise, with greater wall thickness, the mechanism is inhibited coupling (IC) guiding [12,29]. IC waveguides are also referred as broadband, or anti-resonant waveguides (ARF). According to structure, ARF include, in order of their development and optimization: Kagome, negative curvature, single-ring revolver waveguide, conjoined-tube and nested anti-resonant nodeless waveguides [12,21]. Also, chirped HC-MOWs were presented, whose cladding microstructure is formed by layers of holes, arranged in correspondence with a certain law[30,31].

From a computational point of view, fibers can be illustrated by a propagation diagram built on a numeric solution of Maxwell's equations [32]. The implementation for photonic crystal fibers is presented in Figure 2-1. In this diagram, axes are the dimensionless quantities $\beta\Lambda$ and $\omega\Lambda/c$, where Λ is the interhole spacing and c is the speed of light in vacuum. The diagram shows the frequency and axial wave vector component ranges where light is unable to propagate, or evanescent. When keeping optical frequency constant, the maximum possible value of is determined by $kn = \omega n/c$, where n is the refractive index of the region under consideration. Light is free to propagate when $\beta < kn,$ and is evanescent when $\beta > kn.$ For photonic crystal fibers, this diagram represents a band-edge or "finger" plot. In black regions, light is evanescent, including the regions with $\beta < k$ (free light propagation in vacuum), that provides a theoretical approval of light guidance in a silica-air structure.
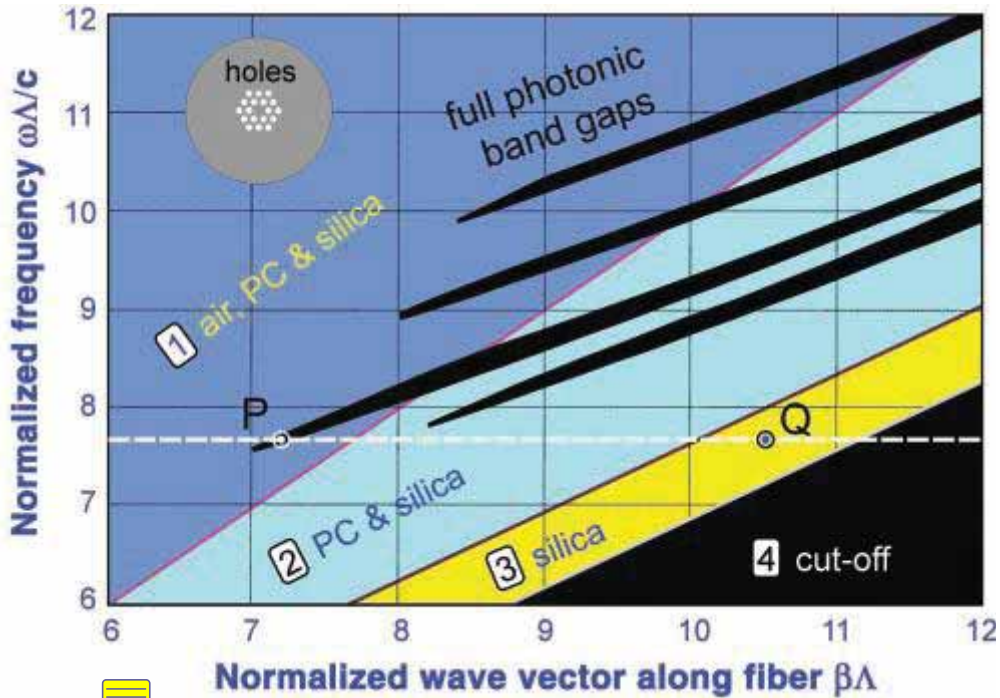
Figure 2-1. Propagation diagram for a triangular lattice of air channels in silica glass with 45% air-filling fraction. region (1), light is free to propagate in every region of the fiber [air, photonic crystal (PC), and silica]. In region (2), propagation is turned off in the air, and, in (3), it is turned off in the air and the PC. In (4), light is evanescent in every region. The black fingers represent the regions where full two-dimensional photonic band gaps exist. Guided modes of a solidcore PCF (see schematic in the top left-hand corner) form at points such as Q, where light is free to travel in the core but unable to penetrate the PC. At point P, light is free to propagate in air but blocked from penetrating the cladding by the PBG; these are the conditions required for a hollow-core mode. From P. Russel, 2003 [32]. Reprinted with permission from AAAS.

Below the work principles for the mentioned above subtypes of hollow-core fibers, namely PBG and AR waveguides, are briefly discussed. They are also illustrated and compared by their modal content on Figure 2-2.
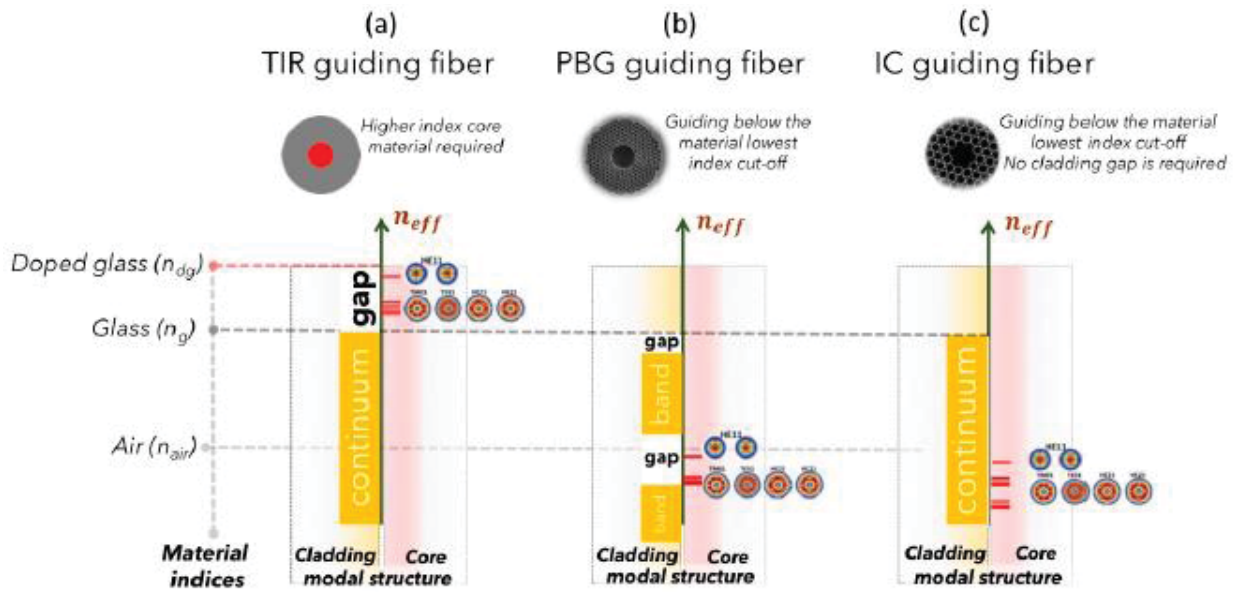
Figure 2-2. Modal content representation of optical waveguide with different guiding mechanisms: (a) total internal reflection; (b) photonic bandgap; (c) antiresonant, or inhibited coupling waveguide. Reproduced from Debord et al.[29]

Photonic bandgap (PBG) Waveguide work principle

In case of PBG, the cladding wall is thin enough (50-150 nm) and not to support modes for a certain range of wavelengths and propagation constants. Light in the core in those ranges (modes not supported in cladding) is not able to couple with cladding modes and guides in the core with low losses [33]. To get a PBG HC-MOW, the core geometry and refractive index must be so at least some of its supported modes lie in the cladding PBG range, i.e. are not allowed to propagate in the cladding; in this case, the core modes cannot leak out because there is cladding mode to couple to [29]. After filling the PBG waveguide with an analyte, the bandgap position shift is determined as [34]:

$$\lambda' = \lambda_0 \sqrt{\frac{1-\left(\frac{n_2'}{n_1}\right)^2}{1-\left(\frac{n_2}{n_1}\right)^2}} \quad , (2\text{-}1)$$

where λ_0 is an initial wavelength of the bandgap position, n_2 and n_2' are refractive indexes of low index (hollow) areas before and after filling, n_1 is refractive index of the

25

walls. On Figure 2-3, the transmitted power of a broadband supercontinuum light source after passing the PBG waveguide is presented. Light gray is for an empty waveguide, and dark gray is for a waveguide filled with D_2O.

However, to provide a broadened PBG transmission, the holes may be filled selectively: the hollow core is filled with a liquid, meanwhile hollow capillaries in the cladding remain air-filled[16]. Such filling configuration is called liquid-core waveguide.
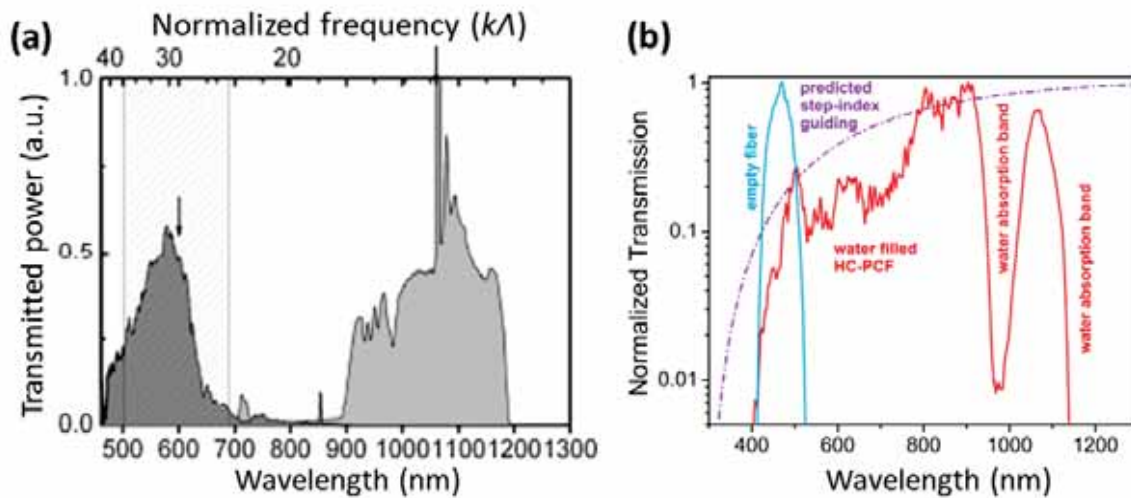
Figure 2-3. (a) Transmitted power spectra of the 1060 nm waveguide using a SC source. The spectra were taken before and after filling the holes of the PBG waveguide with liquid D2O (light and dark grey areas respectively). The vertical lines define the location of the new shifted bandgaps as predicted by the index scaling law. The arrows mark the position of the respective transmission peaks. Reprinted with permission from [Antonopoulos 10.1364/OE.14.003000] © The Optical Society. (b) Transmission spectra of an empty and liquid-core PBG waveguide. Reprinted with permission from Yan et al. [16]. Copyright 2017 American Chemical Society.

Inhibited coupling waveguide work principle

When inhibited coupling is the light guiding mechanism, the antiresonant reflecting optical waveguide (ARROW) model is commonly used to analytically describe its

behavior. The light propagation here is described similar to a Fabri-Perot resonator on parallel plates, with transmission spectrum with minima whose positions are described by the following equation[13,35]:

$$\lambda_{jmin} = \frac{2d}{j}\sqrt{n_2^2 - n_1^2} \quad , (2\text{-}2)$$

where j is an integer describing the capillary mode order ($j = 1, 2, 3, …$), n_1 indicates RI of an analyte filling the capillaries, n_2 is the RI of the waveguide material, and d describes its capillaries wall thickness.

This formula indicates that the transmission spectrum of the waveguide can be influenced by changing the wall thickness, or, when MOW is already manufactured, by applying various layers to the walls. Moreover, the refractive index of the substance inside the waveguide can also affect its transmission spectrum. These characteristics make microstructured optical waveguides suitable for measuring the refractive index of substances[14]. Also, additionally increasing wall thickness by functionalizing inner surface, e.g. by layer-by-layer technique, a set of HC-MOW with different minima positions may be obtained from HC-MOWs with initially identical parameters, as demonstrated in Figure 2-4. This may be beneficial for measuring refractive index dispersion curve.

27
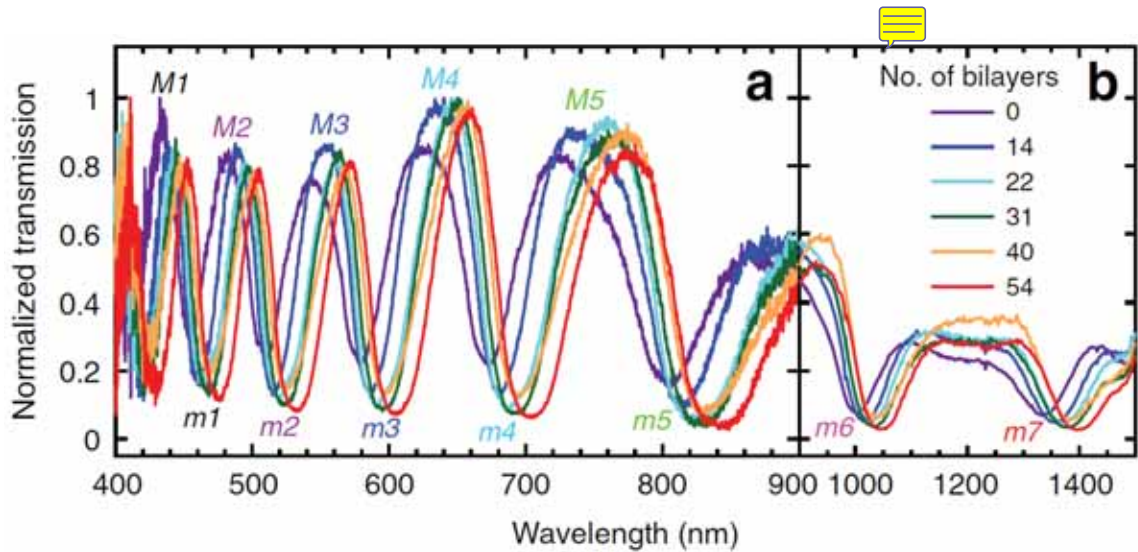
Figure 2-4. Optical characterization of HC-MOWs functionalized by layer-by-layer technique. a, b Transmission spectra in the visible (400–900 nm) and near-infrared (900–1500 nm) ranges, respectively. Note the different scales along the x axis for (a) and (b). Reproduced from Ermatov et al [14].

2.1.2. HC-MOW fabrication

The previous sections described how the spectral properties of microstructured waveguides are determined by the geometry of their cross-section, physical dimensions and material. The complexity of the waveguide geometry, the chosen material, as well as the potential field of application determine the advisability of choosing one or another method of its production. Existing technologies for manufacturing microstructured waveguides can be divided into two classes: single-step and two-step (Figure 2-5). In the first case, the process allows to obtain a finished fiber in one step directly from the source material (rod of the selected material or melt). Such methods include mold casting, 3D printing, and direct extrusion from a die. Multistage methods involve making a waveguide preform on a macro scale in one of the possible ways and pulling the preform into the waveguide of the desired size. The most well-known multi-step method is stack-and-draw.

28
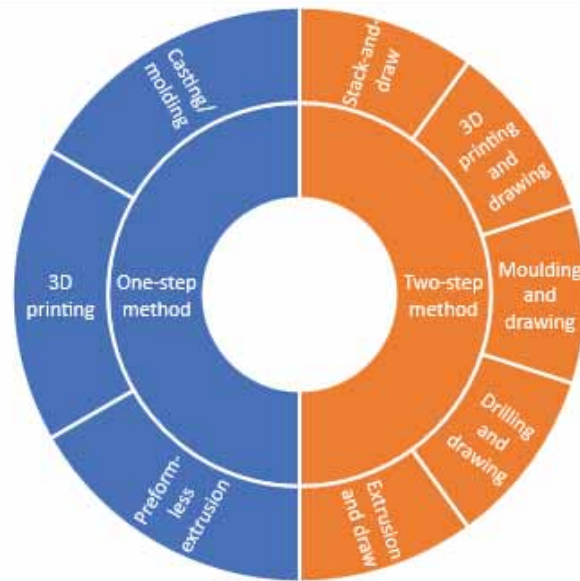
Figure 2-5. Methods of fabrication of hollow microstructured waveguides. Reproduced from [36]

One-step methods of manufacturing hollow microstructured waveguides

Casting/moulding

This method consists in pouring the selected material into a prefabricated mold consisting of an outer tube and the bars attached to it at the ends, which form the structure of the waveguide. The method allows the creation of waveguides of only limited length and relatively simple geometry. On the other hand, the method can have potentially high repeatability and accuracy of manufactured waveguides depending on the quality of the mold. The method is very suitable for creating waveguides from biodegradable and biocompatible materials. Thus, the authors [37] presented a similar cheap, simple, and versatile technology for the fabrication of biocompatible and biodegradable agarose-based structured optical fiber. The fiber is obtained by pouring food agar into a mold with stacked rods, forming a solid core surrounded by air holes (500 μm diameter), where the refractive index and fiber geometry can be changed by choosing the composition of the agarose

29

solution and mold design, respectively. These waveguides are suitable for in vivo imaging, light delivery, sensing, sensing.

3D printing

In recent years, additive technologies have become widespread in the field of microstructural waveguide fabrication. Currently, there are several different types of 3D printers, each with its own unique capabilities and limitations. Each of the technologies has its own disadvantages and advantages, which determine the technically possible limits of the finite dimensions of the waveguides and the choice of material.

The most common types include the following:

- Fused Deposition Modeling (FDM) - FDM printers use thermoplastic filament that is melted and extruded layer by layer to create a 3D object. This is the most common and most affordable type of 3D printer.

- Stereolithography (SLA) - SLA printers use a laser to cure liquid resin into a solid form layer by layer. These printers can produce high-resolution, highly detailed parts, but they can be more expensive and difficult to use than FDM printers.

- Digital Light Processing (DLP) - DLP printers use a projector to layer-cure liquid resin into a solid form. These printers are similar to SLA printers in resolution and detail, but they can be faster and more affordable.

- Selective Laser Sintering (SLS) - SLS printers use a laser to sinter (or fuse) powdered materials (such as nylon or metal) into a solid object. This technology produces highly detailed parts with excellent mechanical properties, but can be more expensive and difficult to use than other types of 3D printers.

3D printing is more commonly used to make macro-sized waveguide preforms for subsequent reattachment, which will be discussed in more detail below. However, the possibility of creating waveguides in one step using 3D printing also exists. In [38] the fabrication of an antiresonant hollow waveguide for the terahertz range using an affordable FDM 3D printer is shown. The waveguide shell consists of semi-elliptical tubes, which is difficult to reproduce with other waveguide fabrication methods. A waveguide of similar

30

structure was also fabricated using 3D printing from photosensitive resin by the authors [39].

Polymer waveguides of high precision, complex geometry and minimal dimensions can be fabricated by 3D two-photon lithography, as shown by Betroncini *et al.* [40]. In two-photon lithography, a focused laser beam induces highly localized polymerization of the photopolymer. The writing laser is a near-infrared femtosecond fiber laser with a pulse duration of ~100 fs, a wavelength of 780 nm, and a repetition rate of 80 MHz. The system uses galvanometer mirrors to control the beam. 3D printing was performed layer by layer. With a layer thickness of 0.2 µm, a scanning speed of 10 mm/s, and a laser power of 13.5 mW, the total fabrication time for the entire structure printed on a 210 µm fiber was about 25 minutes. This is followed by removal of excess polymer and complete polymerization in the developer machine. To demonstrate the capabilities of this technology, the authors repeated the designs of various waveguide designs described in the literature, and also made a three-section polarizing beam splitter directly on the end of a commercially available waveguide.

The main disadvantage associated with the use of 3D printing methods to manufacture waveguides in one step is the roughness of the longitudinal surfaces of the manufactured waveguides due to the layer-by-layer technology, which leads to increased losses in light propagation. Also, the maximum possible length of the waveguide (several tens of centimeters) and the speed of fabrication are significantly limited.

Preform-less extrusion

In direct extrusion, the material is melted and then extruded directly into the desired shape through a die. This simplifies the production process and reduces the number of steps. However, it should be noted that direct extrusion can also have some disadvantages in terms of controlling the homogeneity of the material and ensuring dimensional consistency. In general, the choice between using or not using a preform in the extrusion process will depend on the specific requirements of the application and the desired properties of the final optical waveguide.

Extrusion dies are typically made of stainless steel on CNC machines. In Ebendorff-Heidepriem *et al.*[41] shows the ability to fabricate complex geometry 3D printed dies in Cr-Co-Mo and titanium capable of withstanding the high temperature (560-600 °C) and high force (20 kN) that occur during lead-silicate glass extrusion. Since 3D printing dies have a rough surface, it is necessary to polish the inner surface at the die outlet to ensure the quality of the produced fiber.

Cordeiro *et al.* [42] demonstrate the feasibility of using a commercial, low-cost desktop extruder to produce optical fibers with complex microstructures directly from thermoplastic polymer pellets, Zeonex and ABS. The process does not require the use of a tower to draw the optical fiber and saves time, energy, and space. Various fiber geometries (hexagonal lattice solid core, suspended core, and hollow core) have been successfully fabricated. To demonstrate the feasibility of easy fabrication of doped MOF using this method, rhodamine B-doped ABS fiber was extruded. Among the undoubted advantages of the described method is the potentially infinite length of the fabricated waveguide. The method is also versatile, as it makes it easy to produce waveguides of different geometries by changing the nozzle. Although the method described has been tested on polymeric materials, the authors believe that in the future it will also be possible to use it to manufacture waveguides from glass-like materials. A similar technology was described by Talataisong *et al.* [43]. The authors paid attention to the disadvantages of the process: improperly selected temperature and extrusion speed lead to the formation of air bubbles in the thickness of the waveguide material, which deform the structure; the instability of polymer flow leads to roughness of the waveguide surface.

Two-step methods for manufacturing hollow microstructure waveguides

These methods of fabrication of microstructured waveguides consist of two steps: fabrication of the waveguide preform of the required geometry in the macro size from the selected material and re-pulling in the similarity of the preform to the required dimensions. Drawing in similarity is mathematically described as follows:

$$D_0^2 V_n = d_x^2 V_B,$$ (2.1)

where D_0 is the initial size of the preform (diameter, diagonal length of a hexagonal package or its size along double apothem); V_n is the speed of delivery into the furnace; V_B is the speed of drawing; and d_x is the resulting size of the element [44].

It is worth noting that several deformations of holes in the waveguide structure can occur during the re-tensioning process: destruction of holes, expansion of holes (relative to the outer diameter of the fiber), enlargement of holes (relative to their original size) and changes in hole shape, such hole deformations can lead to significant changes in optical properties of the fiber, such as operating wavelength, confining loss, guiding properties, etc. [45]. Denisov *et al.* [46] demonstrated the importance of maintaining stable temperature to obtain long microstructures with unchanged parameters, additional adjustments for the geometric structure transformation should be considered when drawing light guides with large hole diameters. The authors have shown methods of fabrication of long (more than 1200 m) waveguides with both stable and varying along the length parameters.

Depending on the method of preform manufacture, several basic two-step methods of waveguide fabrication can be distinguished: stack-and-draw, molding/casting and draw, drilling and draw, 3D-printing and draw, extrusion and draw.

Stack-and-draw

The Stack and Draw method is one of the most common methods of creating microstructured waveguides. It involves stacking tubes and rods made of glass or polymer of the same or different sizes in a package of the required geometry, and then pulling the structure to create a preform on a macro scale. If necessary, alternate drawing of several elements of the structure of intermediate sizes from capillaries of large diameter, then from the received elements the whole structure is formed. Capillaries and rods are stacked manually or with a computer-controlled stacking device, if the design allows it, which ensures precise alignment of the tubes and the distance between them. After stacking, this package is pulled into a macro-size preform using a heat source, such as an oven, to soften

the material and create tension. A schematic representation of the drawing process is shown in Figure 2-6. As the material is drawn, the tubes fuse together to form a strong structure with air holes. The resulting preform is then re-pulled in a similar fashion to the waveguides of the desired size. This intermediate re-drawing is an important step because it avoids a drastic change in scale from the capillary package to the final waveguide [47].

This technology allows the creation of unique structures both in terms of the geometrical arrangement of the elements and in terms of the dimensional series. The advantage of the stacking method is also that it can be used for any material, regardless of the melting temperature. Prefabricated capillaries and prefabricated rods with minimum tolerances are also now available and can be used to assemble the preform, making the process easier and increasing the accuracy of the fabricated waveguides.

This technology allows the creation of unique structures both in terms of the geometrical arrangement of the elements and in terms of the dimensional series. The advantage of the stacking method is also that it can be used for any material, regardless of the melting temperature. Prefabricated capillaries and prefabricated rods with minimum tolerances are also now available and can be used to assemble the preform, making the process easier and increasing the accuracy of the fabricated waveguides.

However, the stack-and-draw method has some drawbacks. One of the biggest challenges is ensuring the uniformity and repeatability of the stacking process, which is difficult to achieve with manual stacking. Another problem is to ensure homogeneity of initial capillaries and rods, which always have some variation in size, which further leads to disturbance of the waveguide structure in the drawing process [22]. Air holes can become severely deformed due to unbalanced pressure during extraction. Therefore, drawing conditions such as drawing temperature, drawing speed, and tension must be optimized and carefully controlled to achieve the desired microstructure [46,48].

Jasion *et al.* [49] developed a model that recreates the drawing process of waveguides. The model predicts the parameters and geometry of the waveguide during the drawing process, and selects optimal internal capillary tube sizes and gaps between them, which can

significantly improve fiber fabrication performance, especially in research environments where different structures are often drawn and drawing parameters are often unknown.

Despite these challenges, the stack and draw method remains a popular method for creating microstructure waveguides because of its versatility and scalability. With further improvements in materials and fabrication techniques, it is likely that this method will remain a key tool for creating microstructured hollow-core waveguides in the future.

Despite these challenges, the stack and draw method remains a popular method for creating microstructure waveguides because of its versatility and scalability. With further improvements in materials and fabrication techniques, it is likely that this method will remain a key tool for creating microstructured waveguides in the future.
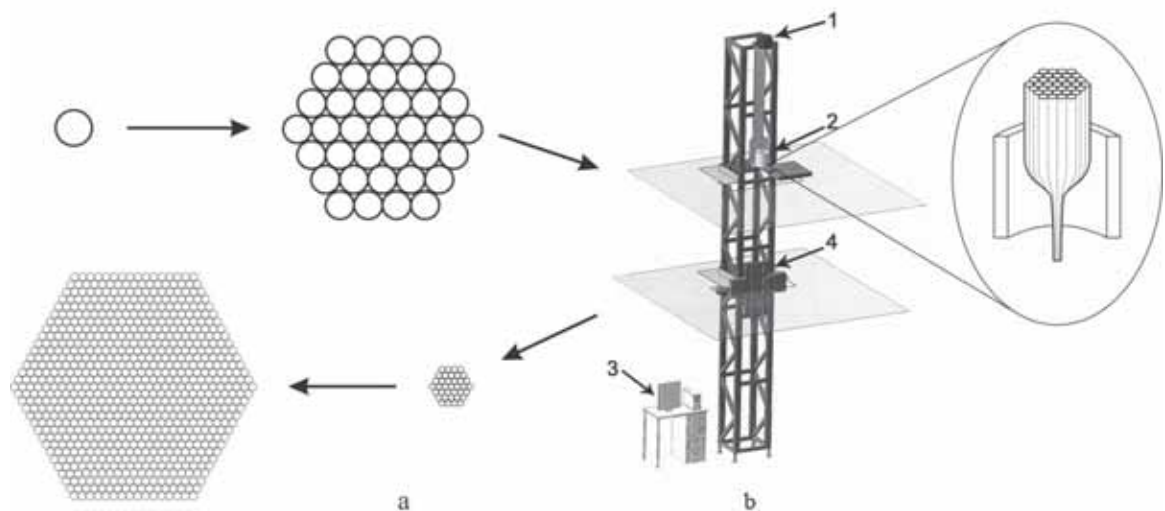
Figure 2-6. Schematic representation of the MOW manufacturing process (a) and MOW drafting unit (b): (1) billet feeding mechanism into the furnace; (2) furnace; (3) computer control; (4) drafting chain mechanism. Adapted from [31].

Extrusion and draw

Earlier in the one-step waveguide fabrication methods, the method of waveguide fabrication by direct extrusion was described. This method is essentially the same. By direct extrusion through a die, a preform of the desired geometry is produced. The preform is then stretched in a similar fashion to the desired dimensions. This method is mainly used

35

when working with soft glass and bypasses some of the disadvantages of the stack and draw method. The work Gattass *et al.* [50], which demonstrates chalcogenide glass anti-resonant waveguides fabricated through this technique. Extrusion was performed using a specially designed vertical glass extruder with a stainless-steel plunger and sleeve. The preforms produced by this method proved to be highly symmetrical with well-defined characteristics. The authors also showed the ability to control the final geometry of the waveguide by changing the internal pressure in the preform during the drawing process.

3D-printing and draw

Earlier in the one-step waveguide fabrication methods, the method of making a waveguide by 3D printing was described. This method is essentially the same. Using 3-D printing, a preform of the required geometry is made. The preform is then pulled in similarity to the required dimensions. A detailed review by Chu *et al.* [51]. Luo *et al.* [52], on the topic of using 3D printing technology to fabricate microstructure waveguide preforms from various types of plastics and glass. In general, the authors write about the prospects of these technologies, as they allow the creation of waveguides with such geometry, which cannot be repeated by the stack and draw method. On the other hand, the most common and cheap 3D printing technique FDL does not provide sufficient accuracy required in the production of waveguides, and methods based on light curing, although they provide the necessary printing quality and resolution, are much more expensive.

Separately, it should be noted that the production of silica preforms using additive technologies is currently possible in two ways. The first method consists of combining silica and organic substances to produce a resin, which is then used to create preforms by light curing methods. This production method has a very high resolution, but an additional purification process is required due to the presence of organics. The second method is the direct sintering or melting of silica powder using a laser. Currently, waveguides manufactured by these methods have a significant level of loss due to the presence of micro-bubbles, micro-cracks caused by uneven voltage distribution during unwinding,

sintering or cooling, streaks between layers during printing, unremoved organic substances and purity of raw materials.

Molding and draw

This method is based on casting a waveguide preform using a mold/mold with the desired cross-sectional profile of the waveguide, made in macro scale. The mold is filled with the selected material (glass, plastic, etc.) and then allowed to harden and solidify. At the same time, it is necessary to control the uniformity of filling of the mold for the absence of air pockets, bubbles and other defects. The preform is then removed from the mold, polished and trimmed to the desired length. The preform is then stretched to the desired dimensions using a stretching mechanism. The specifics of the process may vary depending on the material, the design of the waveguide and the molding or casting equipment used.

Yamamoto *et al.* [53] showed a low-loss waveguide fabrication process based on the slurry casting method. High-purity SiO2 powder, which is produced by thermal oxidation of silicon chloride, is used as a starting material. The required amount of SiO2 powder, organic binder, dispersing agent and distilled water are mixed by ball milling. The resulting suspension is poured into a metal mold. A stainless steel wire with the desired outside diameter is placed in that mold to create air holes in the preform. After the organic binder hardens, the wires are removed and the preform is released from the mold. The resulting preform is dried thoroughly to prevent cracking. The dried preform is then calcined to remove organic chemicals by oxidation at high temperature. The calcined preform goes through a cleaning step to remove metallic impurities and OH, and then is sintered at 1400°C. The sintered preform has the desired microstructure.

Wu *et al.* [54] demonstrated the fabrication of a chalcogenide glass preform by casting. The mold was made of silica capillaries strung on hexagonal silica guides, with the desired hole distribution. After casting and annealing, the silica tube and capillaries that are inside the MOF preform are removed using a diamond tool and soaking in 40% concentrated hydrofluoric acid.

Drill and draw

Making optical waveguides by drilling involves using a laser or mechanical drill to create channels in the glass or plastic rod. The size and spacing of these holes are carefully controlled to ensure efficient light transmission through the waveguide. Once the drilling process is complete, the proforma can be further processed to improve its performance, such as polishing. This technique is quite versatile and allows the creation of complex geometries. However, the drilling process does present some challenges. For example, it can be difficult to maintain the accuracy of drilled holes over a large area, and it can be difficult to maintain consistent hole diameters and depths. In addition, debris can build up during the process that can damage the waveguide or interfere with the light passing through it. To overcome these difficulties, careful control of the drilling process and postprocessing steps is necessary.

Wu *et al.* [54] showed the fabrication of preforms for chalcogenide glass microstructure waveguide by drilling is shown. The equipment consists of two main parts: a drill bit for drilling and an accurate x-y platform for controlling the position of the air holes. After drilling, the inside surface of the air holes is polished. After drilling is complete, the preform must be annealed again at a temperature slightly below the glass transition temperature for 5 h and then cooled slowly to room temperature. The authors have shown that the method based on mechanical drilling allows to obtain different structures of waveguides, from simple to the most complex, and the method can increase the transmission of the obtained waveguides in comparison with stack and drowe, as there are no inhomogeneities in the places of contact of capillaries.

2.1.3. HC-MOW wall modification

Before discussing fiber modification, some main knowledge from theory of chemical bonding is provided. There are three main classes of chemical bonds: electrostatic bonds, covalent bonds, and metallic bonds [55,56]. There are several types of electrostatic bonds, including ionic bonds, hydrogen bonds, dipole-dipole interactions, and Van der Waals

forces. These bonds differ in their binding energy and the nature of their interaction. Ionic bonds are the strongest type of electrostatic bond and form when one or more electrons are completely transferred from one atom to another. This results in one positively charged ion and one negatively charged ion, which attract each other due to their opposite charges. Ionic bonds have very high binding energies and are very strong. Hydrogen bonds are a type of attractive force formed between a hydrogen atom covalently bonded to an electronegative atom (such as nitrogen or oxygen) and another electronegative atom. Hydrogen bonds are weaker than ionic bonds and have lower binding energies but are still strong enough to play important roles in biological systems. Dipole-dipole interactions occur when two polar molecules interact with each other through their partial charges. This force is weaker than both ionic and hydrogen bonds and has intermediate binding energies. Van der Waals forces are the weakest type of electrostatic bond and result from fluctuations in the electron density of molecules. These forces can be attractive or repulsive and their strength is highly dependent on the distance between the interacting atoms or molecules. Overall, the strength of chemical bonds varies widely depending on the specific type of bond involved. Covalent and ionic bonds are the strongest with high binding energies, while hydrogen and dipole-dipole bonds are intermediate, and van der Waals interactions are the weakest with lower binding energies. This detailed description of the types of chemical bonds is provided to demonstrate that the types of chemical bonds are retained in the fiber and that all types of interactions can also be preserved.

The modification of the walls of MOFs can be categorized into two types: modification of the inner capillaries and modification of the outer surface [57–61]. These types of modifications are typically achieved through the same methods. However, the interaction of functional groups occurs either with the guided light or with the evanescent field respectively. Modification is done by attachment of small molecules, or polymers, or nanoparticles to the hollow core fiber wall.

One of the main purposes is attachment of antibodies or reactive molecules to the glass surface. Since the majority of them do not typically adhere directly to the glass, it is

essential to build a structure on which the molecules can be bound using chemical or physical functionalization [62,63], that will be described below.

One of the most popular chemical methods is grafting, that means using oxide surfaces for linking functional molecules [64–66], polymers [67], or metals [68]. There are various attachment chemistries available for grafting: phosphonates, carboxylates, catechols, alkenes, alkynes, and amines. The most stable modification of silica surface by these groups can be obtained by silanization procedure, providing covalent bonding [69,70]. Here, hydrolysis of silane generates silanols that covalently attach to hydroxyl groups on the surface [71]. This allows the use of diverse functional groups for further attachment of sensing molecules or surface passivation. The silane layer density significantly depends on the surface density of hydroxyl groups on the fiber's surface, that may be improved by plasma or acid treatment for hydroxyl activation [72]. After that, silanes can be deposited from liquid or gas phase. In case of silane colution, dipping the freshly activated glass fiber into liquid leads to complete silane coating in minutes to hours [60,73,74]. To sum up, the wide range of organic molecules required for fiber functionalization cannot be strongly adsorbed onto the fiber surface, hence a preliminary modification is needed, such as silanization.

Another chemical method for surface modification is based on electrostatic interaction, typically using charged polymers like polyelectrolytes (PE). One polyelectrolyte or a stack of oppositely charged PE may be used. The latter approach is called the Layer-by-Layer (LbL) assembly method, and it is one of the popular methods for hollow fibers modification. LbL was originally developed for the preparation of nanoscale films [75] and then was adapted to modify MOF [14,57,76–78]. Depositing layers of charged polymers like polyelectrolytes (PE) from a solution which follows a layer-by-layer process [10,14,57,79] make a good sorption of polymers on the surface. The first PE layer is deposited with a charge that opposes the intrinsic surface charge of the substrate, then the surface is rinsed, and a subsequent PE layer with the opposite charge is deposited. The process can be repeated several times to stack layers on any substrate, resulting in an increased PE functional group density on the sensor surface. Alternatively, a volume-doped

polymer layer can be deposited which can both create a safeguard coating and functionalize the fiber to the target species. Therefore, LbL functionalization may be provided for a number of purposes.

Physical functionalization is a term used to describe attaching sensor molecules to the surface through forces other than chemical bonds. From the other side, as physical methods are less reliant on the surface molecules, be employed on a broad range of substrates, including metals, polymers, carbon nanotubes, and glass [80–82].

The deposition of nanoparticles opens up wide possibilities for using fibers as high-precision sensors. It can be provided by various chemical methods [83–86] . Nanoparticles absorbed to the surface may either form self-assembling NP monolayers [87,88] or provide chaotic distribution. NP deposition as a step-by-step process, as an additional linking layer between the fiber wall and nanoparticles is needed. If all bonds present in the resulting multilayer are chemical ones, the structure is strong enough and can be broken ultimately by another chemical reaction. For instance, the linking layer may be silanes, such as (3-mercaptopropyl)trimethoxysilane (MPTMS), that ensures uniform distribution of gold or silver nanoparticles [89]. Another type of the linking layer is polyelectrolytes: their charged surface can attach nanoparticles due to electrostatic forces. Nanoparticles can be embedded in a polymer coating adsorbed on the wall and deposited using the LbL method, as was demonstrated for gold [90] and magnetite [77]. In addition to the described methods of NP deposition, the interaction between the wall and nanoparticles can be further enhanced by annealing [19], as the elevated temperature provides mutual diffusion.

Development of layer deposition protocol plays a crucial role in modification outcome. Therefore, the main typical protocol features are reviewed below. In most studies [57–61,76–78,83,91–98], the modification of MOFs involves depositing one or more layers of various materials onto their surface. This process usually consists of the following steps, with some possible variations: Firstly, the non-modified empty waveguide is thoroughly cleaned to eliminate any potential contaminants both inside and outside. This cleaning procedure may involve a combination of techniques such as plasma treatment, washing the waveguide interior and/or exterior with DI water or different solutions, and high-

temperature heating for a certain duration followed by gradual cooling. As a result, the pretreatment removes any impurities from the fiber surface, breaks existing bonds with organic molecules and/or inorganic materials, and coats the surface with hydroxy groups, which makes further modification easier. Secondly, the MOF surface is activated using a specific substance to facilitate adhesion of the material to be deposited. This is an optional intermediate step that may be employed when a more complex chemical modification is required. The final step is the deposition of the functional layer.

In practice, the second and third steps are executed using one of several methods. For instance, when modifying the inner wall of the waveguide, the material solution can be delivered inside using capillary forces [78], which is the simplest experimental option but has the limitation of limited liquid elevation inside the capillary. Alternatively, the whole waveguide can be dipped into different solutions [78], thereby modifying not only the interior but also the outer walls of the MOF. A more complicated approach involves delivering the liquid inside the capillary using a syringe [57,58], which enables filling even relatively long waveguides but lacks precise control over the rate of solution supply into the MOF, potentially affecting the uniformity of the applied layer. Using different types of pumps [14,92,99] for solution pumping through the waveguide allows for the control of the flow rate and adjustment to the required values. To ensure the uniform application of material to the surface, it is recommended to create a sealed, hermetic connection between the waveguide and the tubes used for solution supply, to prevent air bubbles from entering the MOF.

Thus, wall modification of microstructured optical fibers is provided in most cases with chemical methods, refers to the process of altering the optical fiber's internal or external surface through chemical reactions. This is done to integrate additional functionalities into the fiber or enhance its existing properties for various sensing applications. The modification process can involve coating the surface with a functional layer or creating an entirely new structure on it through various chemical techniques like LbL deposition, atomic layer deposition, silanization and others. The chemical wall modification of microstructured optical fibers can provide advanced sensing capabilities

42

such as enhancing the sensitivity, selectivity, and dynamic range of the fiber, making it potential for various tunable applications in the fields of chemical sensing, biosensing, environmental monitoring, and biomedical applications.

2.1.4. HC-MOW applications for sensing

Unique design features of microstructured optical fibers, namely the presence of a hollow core and waveguide envelope channels, lead to specific guiding regimes. This phenomenon possesses great potential for using in sensing systems. The guiding exists when the refractive index of the core is low compared to the effective refractive index of the shell. In a hollow-core microstructured waveguide, the light tightly confines in a low RI core because of the photonic bandgap formed by cladding or on the anti-resonant reflectance, as was discussed in the section 2 [100].

One limitation in terms of the principle of light propagation is the need to contrast the refractive index of the substance filling the core and shell channels of the waveguide with the substance from which the waveguide is made. Since the refractive index of gaseous substances is close to 1, the development of sensors for gaseous substances seems to be a particularly promising task. On the other hand, microstructured waveguides made, for example, from glasses with a high refractive index can be successfully used to create sensors for liquid media.

Microstructured waveguides offer highly efficient interaction between light and analytes in longitudinal dimensions. The use of hollow core waveguides provides to trap the minimum sample volume at very low concentration into a long optical path with tight optical confinement has been shown to enhance the analyte-light interaction by orders of magnitude, resulting in improved sensitivity and selectivity of biochemical sensors [101]. The transmission wavelength band of the waveguides can be tuned to the required wavelength range by changing the dimensions of the internal microstructure. For example, HC-MOF can be manufactured from fused silica, which exhibits minimal fluorescence even at deep-UV wavelengths, and with structure dimensions such as to allow high UV transmission [102].

The waveguides provide the interaction between the light and with the fluid/gas or the substances carried in the fluid/gas (including chemical macromolecules and biomolecules) to generate a specific light signal response. Then efficient and rapid measurement of biochemical quantities can be achieved due to combined with various sensing mechanisms such as molecular absorption, fluorescence detection, refractive index, Raman scattering [103,104], etc.

Sensors based on HC-MOF offer superior performance and practicality making them an ideal choice for a wide range of sensing applications. They allow for enhanced long path analyte-light interaction, are portable, immune to electromagnetic interference, easy to use, and are relatively inexpensive to produce on a large scale. Furthermore, MOF-based sensors have additional advantages such as ultra-low sample and reagent consumption, making them more effective [100,101,103–105]. In addition to biochemical sensing, hollow core microstructured optical waveguides can be widely employed in the sensing of various physical parameters such as temperature, strain, curvature, displacement, liquid level, and mechanical force, fully exploiting the intrinsic advantages.

Refractive index and layer deposition sensing

Liquid sensing, based on the detection of changes in the refractive index (RI) of the measured medium, is one of the most important applications of HC-MOW. This makes it promising for environmental monitoring, food and beverage quality control, and biomedical diagnosis in a label-free and real-time manner. In contrast to conventional waveguides with a solid core, HC-MOW offer a completely hollow core that, when a sample is pumped into it, can enhance the interaction with the guided light in the core region. This enables greater sensitivity and control over the sensing, and potential to avoid cross-sensitivity to other factors by isolating samples from the external environment.

Wang *et al.* [106] proposed a fiber optic refractive index sensor based on the ARROW (anti-resonant reflecting optical waveguide) and mode interference, which offers both high sensitivity and large dynamic range for detecting refractive index changes in chemical and biological applications. The use of hollow-core fiber provides a natural microfluidic

channel for the liquid sample, simplifying the complexity of RI measurement. The ARROW mechanism allows for strong interaction between the guided light and the liquid sample in the microfluidic channel, while the mode interference generates evanescent fields that modulate the resonance wavelength of the fiber. The proposed sensor overcomes the tradeoff between sensitivity and dynamic range by utilizing different refractive index sensitivities of ARROW and mode interference. The experimental results demonstrate a high refractive index sensitivity of 19014.4 nm/RIU for mode interference and a large dynamic range from 0.04 RIU for ARROW. This paper provides a promising solution to the challenge of achieving both high sensitivity and large dynamic range in fiber optic RI sensors.

Chen *et al.* [107] presented a highly sensitive waveguide sensor based on a liquid infiltrated modal interferometer in a hollow-core waveguide is presented. The sensor is specifically designed for refractive index and temperature sensing applications. It is constructed by splicing a section of hollow-core waveguide filled with high refractive index liquids between single mode waveguides, which results in changes in the transmission properties of the hollow-core waveguide. The infiltration of liquids also introduces modal interference, which allows for highly accurate sensing of temperature and refractive index changes. The sensor exhibits high sensitivity to temperature change, with a maximum sensitivity of -1.4 nm/°C observed in the temperature range from 22°C to 36°C. Additionally, the sensor shows a spectral shift towards longer wavelengths as the ambient liquid refractive index increases, with a highest sensitivity of 884 nm/RIU achieved around an RI value of 1.448. This liquid infiltrated hollow-core waveguide interferometer is a simple and cost-effective method for highly accurate temperature and refractive index sensing.

Zhao *et al.* [108] proposed a novel liquid sensing method using a cascade of traditional single-mode fiber (SMF) - hollow-core fiber (HCF) - photonic crystal fiber (PCF) - SMF structure, which simultaneously forms a reflected Fabry–Perot interferometer and a transmitted Mach–Zander interferometer. The HCF is filled with ethanol, which exhibits sensitivity to temperature changes. By monitoring the reflected and transmitted spectra,

simultaneous measurement of temperature and refractive index (RI) changes can be achieved. A significant advantage of this method is that the two spectra do not interfere with each other, simplifying the demodulation process and avoiding the need for complex fast Fourier transform and matrix computation. The proposed method shows high sensitivities for both temperature and RI, with values of up to 0.454 nm/°C and 178.7 nm/RIU, respectively.

Liu *et al.* [109] introduced an ultracompact and highly sensitive liquid refractive index sensor employing cascaded Fabry-Perot (FP) cavities with an in-fiber mirror inscribed in single-mode fiber (SMF) using femtosecond laser technology. To allow the liquid to enter or leave the hollow-core cavity, two micro-holes are drilled on the side wall of the HCF by femtosecond laser micromachining. The design of the device provides an enhanced and precisely controllable amplification factor for the Vernier effect, which yields an ultra-high refractive index sensitivity of -73417.9 nm/RIU. This sensitivity is approximately 73 times greater than that of the fiber FPI sensors without using the Vernier effect. The device is simple to fabricate and features good repeatability.

Zheng *et al.* [110] proposed a new high-linearity liquid sensing method using an analyte-filled defect hollow core Bragg fiber (DHCBF). This method employs a resonant wavelength induced by transverse coupling between core and defect modes to detect changes in refractive index (RI) of the liquid analyte. The researchers were able to improve the linearity of the sensor significantly by optimizing the structural parameters of the defect layer, thus enlarging the dynamic measurement range. By using an analyte-filled DHCBF with a low RI-contrast cladding, they demonstrated a high-linearity RI sensor with a sensitivity of 2062 nm/RIU and an adjusted R-Square value of 0.99967 in the measurement range of 1.324 to 1.432. This new sensor achieved higher sensitivity and a larger dynamic range compared to those based on standard hollow-core fibers.

Recently, Alam *et al.* [111] presented a highly sensitive biosensor based on HC-MOF for detecting low-index liquid analytes, with a focus on detecting plasma concentration in blood samples. The authors demonstrate how variations in plasma concentration in blood can change the transmission spectra of HC-MOFs due to the photonic bandgap mechanism.

They use a finite element approach to explore the biosensor's performance, and it is shown that the biosensor is an effective way to detect changes in blood plasma. The authors investigate various HC-MOF structures with varying numbers of cladding rings and a hollow core filled with a liquid sample to detect various concentrations of blood plasma. They measure changes in the bandgaps and transmission spectra of the proposed HC-MOFs to study the biosensor's performance over a wide variety of analyte refractive indexes. The article reports that an ultra-sensitive HC-MOF biosensor for detecting blood plasma has been developed, and it has an average spectral and amplitude sensitivity of 8928.57 nm/RIU and 1.21 dB/RIU, respectively.

Gao *al.* [112] proposed and experimentally demonstrate an optofluidic anti-resonant reflecting guidance using hollow-core photonic crystal fibers (HC-PCFs) for the precise measurement of liquid refractive index (RI). By fabricating micro-channels with femtosecond laser micromachining, a Fabry-Perot resonator is formed between the hollow hole and cladding, which changes its resonant condition with the RI change of the liquid sample. This change can be detected through the wavelength shift at the dip wavelength in the transmission spectrum, allowing for a sensitivity of up to 1328 nm/RIU in the RI range of 1.345 to 1.363.

Finally, Ermatov et al. [14] introduces the concept of in-fiber multispectral optical sensing (IMOS) as a highly efficient and cost-effective method for real-time detection of liquid biological samples. IMOS is based on antiresonant HC-MOW to detect spectral shifts in the transmission spectrum caused by the presence of a bioanalyte, as demonstrated in Figure 2-7. By coating the capillaries of HC-MOW with polymer nanofilms and this providing additional spectral shifts, IMOS can measure the refractive index at up to 42 wavelengths, with a sensitivity of up to ~3000 nmRIU^{-1} and a figure of merit (FOM) reaching 99 RIU^{-1} in the visible and near-infra-red spectral domains. IMOS offers a unique advantage over other optical biosensors, providing simultaneous measurement of a bioanalyte's RI over a wide spectral domain in real-time. The practical performance of IMOS has been demonstrated by measuring the concentration and RI dispersion of bovine serum albumin (BSA). The accuracy of BSA concentration measurement achieved by

IMOS matches that of standard tests on albumin. The production of functionalized HC-MOWs is simple and cost-effective.
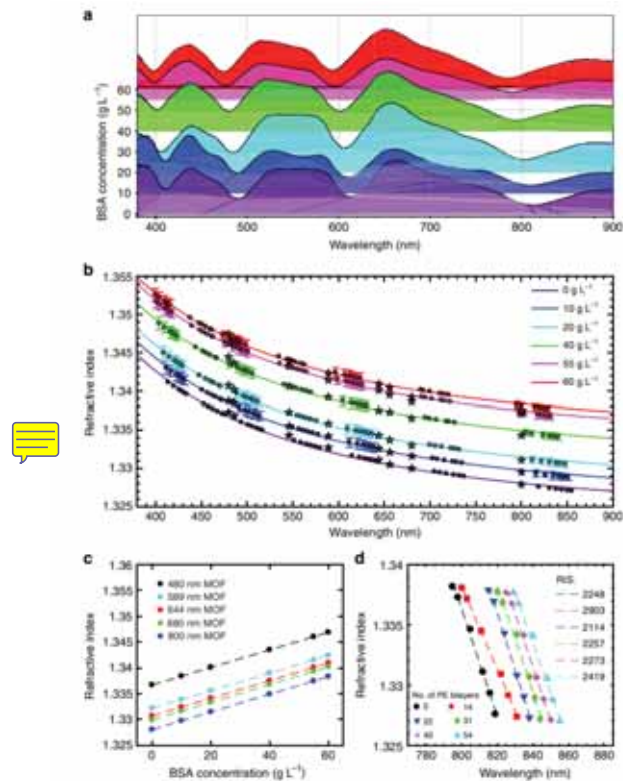
Figure 2-7. Performance of IMOS for BSA dissolved in deionized water in static mode. a) Transmission spectrum evolution with increasing BSA concentration for the non-modified HC-MOW. b) Optical dispersion of BSA in a water buffer with different concentrations. Coloured points: extracted from the shifts in the minima and the peak centroids of the fiber transmission spectra; solid line: their Sellmeier fits. The stars mark RIs measured by the Abbe refractometer, provided for comparison. c) Calibration relating the concentration of BSA and RIs of the BSA-water solution at different wavelengths. The RIs of BSA are extracted from the Sellmeier fits of the experimental points (see Table 1S). d) The positions of the longest-wavelength minima as functions of RI extracted from (a) and (b). The error bars are smaller than the data points. Reproduced from Ermatov et al. [14].

Raman and SERS sensing

Raman sensing

Raman spectroscopy is a powerful technique used to analyze the vibrational properties of molecules. Additionally, Raman spectra is unique for every substance (so it is often referred as "fingerprint"), that enables possibility to qualify and quantify substances [113,114], making Raman spectroscopy a great tool for biomedical application [115]. In conventional Raman spectroscopy, a sample is irradiated with a laser, and the scattered light spectum is analyzed to determine the vibrational frequencies of the sample's molecules. However, Raman signal intensity is often weak (as around 1 of 10^7 photons scatters inelastically), making it difficult to detect low concentrations [116].

One of the ways to slightly improve Raman intensity is fiber-enhanced Raman spectroscopy (FERS): HC-MOF can enhance the intensity of Raman scattering signal observed by confining the laser light and the gas or liquid sample in a small volume, increasing the interaction length between them and guiding the scattered light directly to the detector [17,117]. The reviews of Markin *et al.* [118] and Ding *et al.* [17] comprehensively describe the use of microstructured optical fibers in Raman spectroscopy and demonstrate applicability of both PBG and antiresonant fibers for that. Furthermore, plasmonic nanostructures may be added to HC-MOF to provide surface enhanced Raman scattering (SERS) to improve Raman intensity even more. The variety of approaches to

Raman scattering in a hollow-core fiber is presented in Figure 2-8.
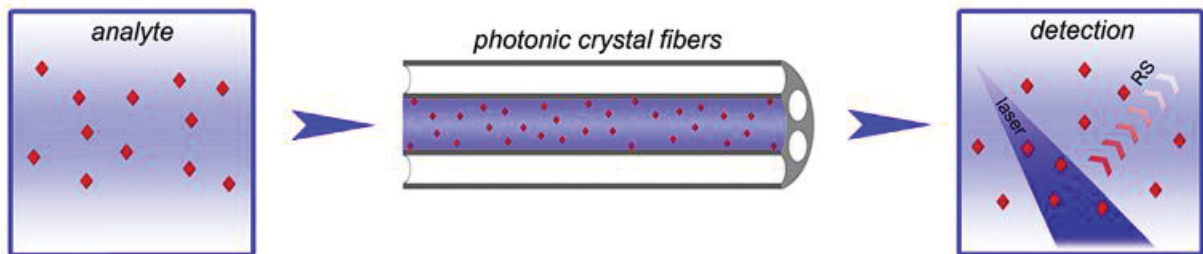
Figure 2-8. Raman and surface-enhanced Raman spectroscopy (SERS) with HC-MOW: (a) Raman scattering; (b) label-free SERS; (c) label-based SERS. Reproduced with adjustments from Markin et al.[18].

A bare HC-MOF enhances observed Raman signal intensity for 1-2 orders of magnitude compared to liquid in a form of a drop on a plain surface or filling a cuvette [25,119–121], thus providing improved detection sensitivity. Khetani *et al.* [121] explored Raman signal amplitude dependence on fiber length, and for a backscattering Raman signal collection configuration, PBG fiber and heparin-serum analyte got a maximum enhancement of 90 times at 8 cm fiber length. However, these values may be affected by analyte (light absorption, viscosity, surface tension) and fiber (loss) properties. Liquid analytes that were probed for Raman scattering in HC-MOF include e.g. heparin in serum [121], glucose [120], antibiotic moxifloxacin [119].

The simplest way to perform Raman sensing of liquid with HC-MOF is to fill both core and cladding holes by the analyte. However, a PBG fiber has a disadvantage connected with a narrow band gap in cladding modes and hence propagating core modes. To expand a spectral range for Raman sensing, the cladding holes of the HC-MOF may be sealed, so the liquid fills ultimately the hollow core [119,122]. This type of fiber is referred as liquid-core PCF.

Along with liquid substances, HC-MOF is applicable for Raman analysis of gases composition for medical, environmental, industrial, purposes [11,117]. So, the analysis of human breath can disclose health issues such as malabsorption syndrome [123] and detect natural isotopes [124].

SERS sensing

However, as Raman scattering possesses low signal intensity [116], the bulk fiber enhancement may not be sufficient to detect low concentration. Besides, multi-component systems (solution, gas) complicate the analysis of results. These difficulties can be overcome by the effect of plasmon resonance on metal (typically gold or silver) nanostructures, that dramatically enhance Raman signal from molecules in their vicinity by amplifying both incident and inelastically scattered light. Such amplification technique is referred as SERS (Surface Enhanced Raman Scattering) and may result to $10^6 - 10^{11}$ enhancement factor [125]. As demonstrated in Figure 2-8b, plasmonic nanostructures for SERS in HC-MOF may be implemented either by in a form of solution of nanoparticles (colloids) mixed with an analyte [20,122,126–133]. Technologies for wall modification of HC-MOF are discussed in Section 3.2.1. Plasmonic nanoparticles may be label-free and

mixed with the analyte in a non-specific way [20,122,126,128,130–134] or provide targeted binding to particular molecules and contain Raman reporters as labels [135,136].

To gain greater enhancement for SERS in HC-MOF, authors implement a number of improvements, such as: in the case of colloidal suspensions of plasmonic nanoparticles, the use of anisotropic nanoparticles (nanorods, nanostars, nanotriangles, etc.) allows higher enhancement compared to spherical nanoparticles [137,138]; tuning the laser excitation wavelength close to the absorption peak of the colloid to excite surface plasmons more actively [129]; tuning the laser excitation wavelength in the electronic absorption band of the analyte to obtain resonance Raman scattering to achieve several more orders of signal enhancement [126].

Furthermore, an indirect SERS reporting, or label-based SERS, is demonstrated in Figure 2-8c and may be implemented to overcome a problem of a weak Raman scattering of the analyte or when providing molecule detection in a complex sample such as blood. Indirect SERS reporting assumes colloidal SERS nanoparticles with Raman reporter molecules on their surfaces, possessing a relatively strong Raman signal [118,139]. Simultaneously, these SERS nanoparticles are functionalized with targeting ligands to molecules of interest. Such complex structures are called SERS nanotags. If the molecules of interest are previously absorbed on the HC-MOF inner wall, then the SERS nanotags will be captured via targeting ligands and provide signal from Raman reporters meaning that the molecules of interest are detected. Dinish et al. firstly demonstrated SERS detection of one cancer protein (EGFR) from a cell lysate [135] and then expanded the approach to multiple detection of three biomarkers using SERS nanotags with different targeting ligands and proteins [136].

2.2. Biomarkers used for medical diagnostics. Extracellular vesicles

2.2.1. Biomarkers for medical diagnostics

The accurate detection and diagnosis of cancer in the very early stages of its progression is highly important to increase the probability of achieving a successful treatment. Recently, liquid biopsy has emerged as a minimally invasive approach that can

52

potentially be used in medicine for early diagnosis and monitoring of patient's health. This approach is based on the reliable detection of tumor markers circulating in biological fluids using various techniques. Recently, identification and quantification of circulating tumor cells (CTC), circulating tumor DNA (ctDNA), and extracellular vesicles (their subtype called exosomes) have attracted particular attention for early cancer detection. Their size and time of appearance are compared in Figure 2-9.
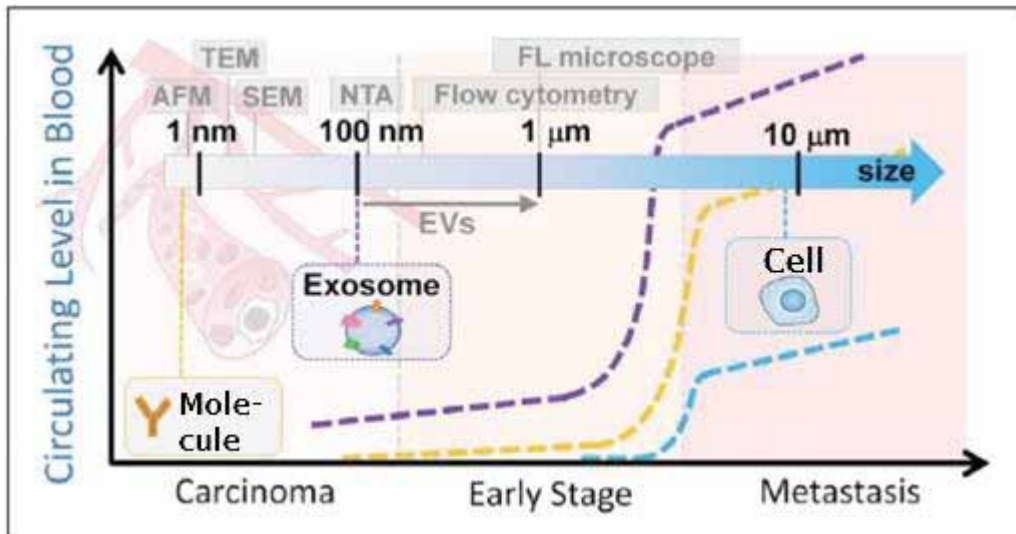
Figure 2-9. Markers for diagnostics. Adapted from He et al.[7]

CTC is one of FDA-approved liquid biopsy methods with relatively high specificity that allows performing in vitro examination by cell culturing as well as phenotypic and genotypic analysis. On the other hand, CTC's complex heterogeneity, low abundance (1–10 cells/10 mL of peripheral blood of cancer patients [7]), and difficulty to develop an enrichment technology in order to achieve a high limit of detection (LOD) present a challenge for CTC to be a single, universal, and reliable approach for cancer diagnostics in its early stages. Quantification and analysis of ctDNA present in cancer patient's blood is another Food and Drug Administration (FDA)-approved liquid biopsy method that can become a supplement to conventional biopsies due to its high sensitivity and easy access to genomic information of the patient. Access to such information allows the selection of the most appropriate treatment and to monitor its effectiveness in real-time. In addition, it

was shown that ctDNA levels often correlate with tumor burden [140]. However, ctDNA has a short half-life in blood (~2 h) [141] and can interfere with cell-free DNA (cfDNA) that is not related to the tumor [142]. Similar to CTC, current FDA-approved ctDNA assays have low LOD at ~25 copies/mL [143] making its detection and ability to obtain a detailed molecular profile a difficult task. Although detection of CTC and ctDNA can become highly effective approaches for cancer diagnosis, the mentioned challenges impact the feasibility of their implementation for diagnosis especially at the initial stage of cancer. In this respect, analysis of extracellular vesicles (EV) circulating in the patient's body may be an innovative and promising method for the diagnosis of cancer and solving the most important problems of sensitivity, specificity, and reliability of currently available diagnostic methods.

2.2.2. Extracellular vesicles for diagnostics

Extracellular vesicles are nano- and microsized objects with a lipid bilayer produced by biological cells. Due to their biogenesis, EV may be divided to three subtypes, as demonstrated in Figure 2-10: microvesicles (ectosomes), that are produced by direct outward budding of the cell membrane; exosomes, that are produced by firstly inward budding of the cell surface region, then they are processed inside the cell and finally released outside; and finally apoptotic bodies that are the result of cell fragmentation after death [5].
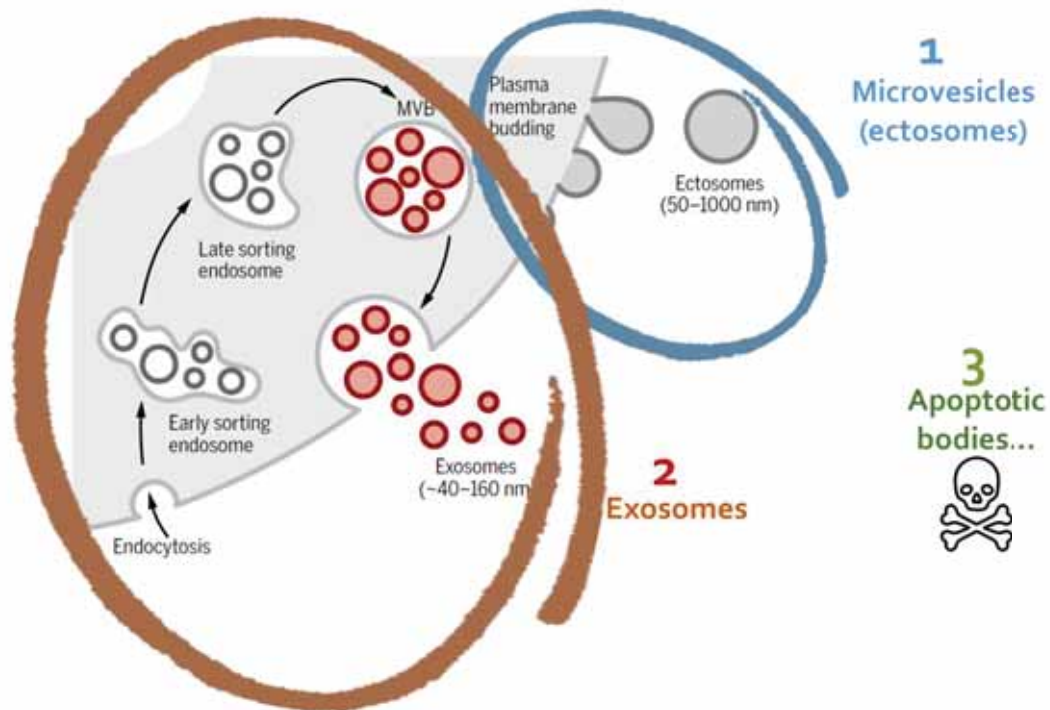
Figure 2-10. Types of extracellular vesicles. Adapted from Kalluri et al.[5]

Due to a multistage process of formation inside the cell, represented in Figure 2-11, exosomes are the EV that are most enriched with cellular footprint, such as a variety of proteins and nucleis acids and thus the most informative about the parental cells and hence represent the most interest for diagnostics. However, isolation of only exosomal fraction from overall EV solution is intricate due to ectosomes with intersecting size distribution. Therefore, sometimes an overall fraction of EV with size 40-160 (200) nm is referred as exosomes, although this is not technically right and should be referred as extracellular nanovesicles (ENV) [144].
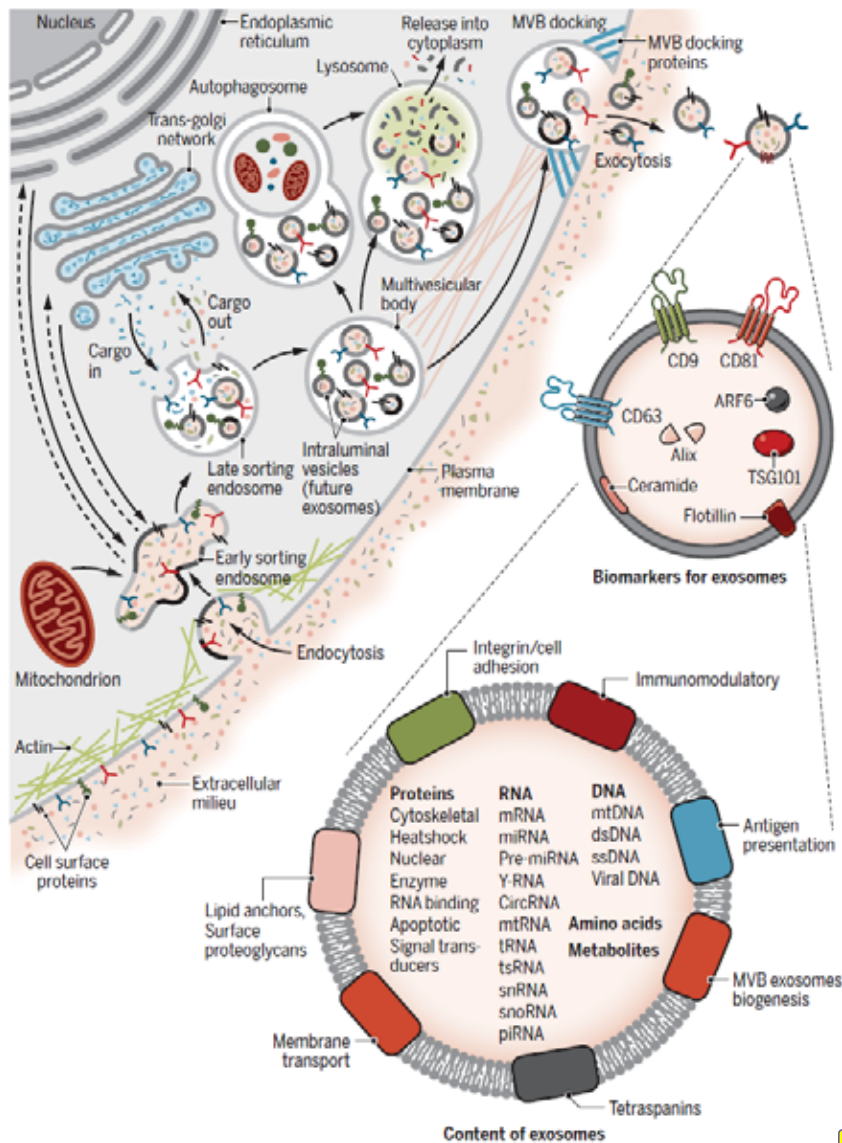
Figure 2-11. Exosome biogenesis. Reproduced from Kalluri et al.[5]

Extracellular nanovesicles (ENVs) are minor components of plasma. Their quantitative and qualitative patterns are still poorly understood, but the emerging biological significance of ENVs is attracting growing scientific interest. It is now assumed that the population of circulating vesicles mediates the interaction of anatomically distant cells [145], and this population is extremely heterogeneous [146]. As evaluated by the original technology of cryo-electron microscopy of vesicles labeled with gold particles, plasma contains membrane formations of various morphologies, including spherical vesicles with

56

a diameter of 30–1000 nm, tubular vesicles with a length of 1–5 µm, and membrane fragments up to 6–8 µm, with the former accounting for >95%, the latter accounting for <5%, and the third accounting for <0.5% of the entire population [147]. Moreover, 1 µL of plasma includes approximately 5 x 10^5 spherical vesicles and 2 x 10^3 tubular vesicles [147]. Other studies have presented quite different results of plasma ENV quantitation. For example, the concentration of plasma nanovesicles measured by nanoparticle tracking analysis (NTA) varied from 10^{11} to 10^{12} particles per mL [148]. Nanoflow cytometry (nFCM) allowed the detection of 10^7 to 10^{13} exosome-like vesicles per 1 mL of plasma, depending on the method applied for isolation [149]. When ENVs were isolated by the standard ultracentrifugation procedure, the concentration of plasma ENVs differed by 2–3 orders of magnitude [148,149]. Such obvious discrepancies in the quantification of plasma ENVs may reflect the imperfection of both the isolation methods and the calculation technologies. The isolation of nanovesicles from plasma is indeed a nontrivial task that has led to the development of many methods [150,151]. The current approaches can be generally divided into two main groups: methods based on specific physical properties of ENVs and methods based on the chemical characteristics of the vesicular membrane. The first group of methods includes ultracentrifugation as a "gold standard" [152], with various modifications (speed, time, gradient density medium) and ultrafiltration. More advanced approaches are based on microfluidic effects and nanoparticle flow fractionation phenomena [153]. The second group of methods is based on more or less specific binding of the components of the vesicular membrane with various ligands, including protamines , aptamers [154], antibodies [155], etc. This interaction leads either to the "fixation" of vesicles to a solid matrix or to the formation of multi-vesicular complexes, which are easily precipitated by low-speed centrifugation. The first group of methods makes it possible to obtain fairly pure ENV preparations from plasma, but these methods are relatively laborious and associated with losses of vesicles during the isolation process. The methods of the second group have one common drawback—there is no known vesicular marker that would be presented exclusively on ENVs and on all ENVs. Therefore, ENVs isolated by any of the affinity methods represent a certain fraction.

To date, numerous methods have been developed to isolate, detect, and characterize exosome-like vesicles. The most common protocol that is considered to be a gold standard for isolation of exosomes is differential centrifugation, which includes three main steps: low speed centrifugation during a short time period; high speed centrifugation with extended time period to remove cell debris and microvesicles; and ultra-high speed centrifugation, or ultracentrifugation (UC), at forces of 100,000 g or greater to precipitate exosomes[156]. An additional centrifugation step, using sucrose or iodixanol to form a density gradient, can be coupled with differential centrifugation to further purify the sample from contaminants [157]. Size-exclusion chromatography [158], immuno-affinity capture [159], filtration [160,161], polymer-based precipitation [162], field-flow fractionation [163], and different combinations of these methods [160,164] have been introduced in recent years to reduce the cost and time needed for exosome isolation and achieve high yield and purity of exosome samples. Microfluidic technology is yet another new and effective technique for the non-invasive separation of exosome-like vesicles preserving the structure and composition of intact exosomes [165,166] with the ability to process and characterize exosomes by using immunolabeled entities simultaneously [167–169]. At present, the enzyme-linked immunosorbent assay (ELISA) is the gold standard for exosome quantification using their membrane proteins, such as CD63, CD9, and CD81 [167–169]. Although ELISA provides rapid analysis of exosomal membrane proteins with relatively low cost, it is difficult to capture all subpopulations of exosomes containing the protein of interest and perform fast analysis of multiple samples.

To enhance efficiency in the quantification and multiplex detection of exosomes, optical methods have been developed. While nanoparticle tracking analysis (NTA) [170,171], dynamic light scattering (DLS) [172], and flow cytometry (FC) [173] can be used to obtain the size distributions and concentrations of exosomes in the fluid samples, fluorescence microscopy is used for in vitro imaging and tracking of exosomes labeled by specific fluorophores [174,175]. Surface plasmon resonance (SPR) provides quantitative information about exosomes attached to the surface of the SPR sensor with an exosome specific antibody [176].

2.3. Summary

On the one hand, among the variety of biological markers present in liquid biopsy, recently discovered nanosized extracellular vesicles (EV) released by cells hold great interest for early diagnostics.

On the other hand, HC-MOW can be used as a sensor for liquids. The thickness of the first inner wall thickness determines the type of light propagation in HC-MOW. If the thickness is less than 150 nm, the mechanism is photonic bandgap (PBG) guiding; otherwise, with thicker wall thickness, the mechanism is inhibited coupling (IC) guiding. Other names for IC are broadband, or anti-resonant fibers (ARF). This type of waveguide is the most promising for sensing applications because multimodal sensing can be organized based on a combination of several techniques: a multi-wavelength refractive index sensor, a sensor with layer deposition control, a fiber-enhanced Raman scattering sensor, a SERS sensor. Combining several sensing modalities could allow for multifaceted characterization of complex fluids. The examples of such fluids are synthesized macromolecule structures, complexes, and extracellular vesicles. The latter leads to a perspectivity of using HC-MOW in the diagnosis of liquid biopsies.

The aim of this study is to narrow the gap between HC-MOW and EV by developing multifaceted liquid sensing approaches. This will be accomplished by first testing a model dye in HC-MOW, followed by macromolecular nano- and microsized structures, and ultimately EV.

Chapter 3. Research Methodology

3.1. Sample Synthesis and Characterization

3.1.1. Chemical reagents used

Bovine serum albumin (BSA), N−vinyl−2−pyrrolidone (NVP), acrylic acid (AA), 2,2′−azobis (2−methyl propionitrile) (AIBN), 1−octadecanethiol (ODT) are all purchased from Sigma−Aldrich (Germany). 1,4−dioxane is purchased from Chimmed (Russia).

The copolymer of poly (N−vinylpyrrolidone−*co*−acrylic acid), labeled as P(VP−AA) throughout the manuscript, is synthesized similarly to Estifeeva et al.[177]. Briefly, NVP and AA are dissolved in 1,4−dioxane with desired amounts, AIBN and ODT are added to the mixture, followed by sealing the vial and keeping it for 3 h at 70 °C. After the synthesis, a copolymer is purified by dialysis with the membrane cut−off 0.5 kDa and freeze−dried. The same set of methods is used to assess the properties of the resulting amphiphilic copolymer as in[177–179]. The P(VP−AA) copolymer used in the manuscript shows a molecular weight of 18 kDa with 9.7 mol %. of AA units randomly distributed in the chain structure.

Polyethyleneimine (PEi, MW 750,000), chloroauric acid (HAuCl4, 1% aqueous solution), and trisodium citrate (Na3C6H5O7, 1% aqueous solution) were purchased from Sigma Aldrich. For PEi dilution and sample wash, deionized water (18 MΩ*cm, Millipore) was used. For HC-MOW pump coating, a peristaltic pump (Shenchen) and a flexible silicone tube with an inner diameter of 1mm were used.

3.1.2. Gold nanoparticles synthesis and characterization

AuNP seeds, which are an aqueous solution of AuNPs with tetrakis-(hydroxymethyl)-phosphonium chloride (THPC) as simultaneously a reducing agent and stabilizing ligand, were synthesized as described previously [180], with gold concentration 1 mg/mL. Three months passed between the seed preparation and their utilization in the current experiment, therefore their size increased due to Ostwald ripening. Larger AuNPs stabilized by citrate in an aqueous solution were synthesized by a modified Turkevich method [181], with gold concentration 0.2 mg/mL. Both types of AuNPs were imaged by transmission electron microscopy (TEM) and their size distribution was estimated using dynamic light scattering

(DLS), as demonstrated in Figure 1. TEM images were taken on a Zeiss M912 Omega transmission electron microscope (Carl Zeiss Microscopy GmbH, Oberkochen, Germany) at an operating voltage of 300 kV. DLS analysis was provided on Zetasizer Nano ZS (Malvern Panalytical), with 3 measurements for each sample.

3.1.3. Nanoscale visualization using SEM

SEM observations were carried out without a metal coating using JEOL JSM-7200F FE-SEM. The hollow-core microstructured waveguides (HC-MOWs) were analyzed at 30 keV accelerating voltage using SE-detector. For the observation of the SERS-active substrates on glass slides, a beam deceleration function and charge-free scanning mode was used. To reduce the charging phenomenon the beam was decelerated in the vicinity of the specimen to 1.5 keV (gentle-beam mode). To use the low acceleration voltage the sample was biased to 2.0 kV. SEM images were taken by using an upper detector (UED) with the backscattered electron mode.

3.1.4. UV-mediated gold reduction

As a UV light source, Camelion LH26-FS 26W light bulb was used, with an emission spectrum centered at 365 nm. Samples were placed approximately 3 cm under the vertically mounted bulb, so that power density on the sample measured at 365 nm was 4.3 mW/cm^2.

3.2. Measurement Setups

3.2.1. HC-MOW transmission spectroscopy

To verify the adsorption of functional materials onto waveguide capillaries, the optical transmission of functionalized waveguides was measured, since the formation of nanocoating leads to the growth in the effective thickness of capillary walls and shifts in the waveguide transmission windows towards longer wavelengths [14].

The optical setup used in our experiments was described by Ermatov et al. [14]. The output light of a broadband halogen lamp (Thorlabs SLS201L, 360–2600 nm) was initially collimated (Thorlabs F220SMA-532) and then focused by a 10× objective (Olympus) to the HC-MOW input. The other 10× objective (Olympus) was used to collect the transmitted light, which was further guided to a compact CCD spectrometer (Thorlabs CCS100) operating in the extended wavelength region (200–1000 nm). All of the transmission spectra were initially normalized to the spectrum of the lamp and then to its maximum value [14]. Positions of minima were calculated using a centroid function.

3.2.2. Confocal Raman microscopy

For all samples, Raman measurements were provided on Raman spectrometer LabRAM HR Evolution (HORIBA France SAS, France), with a diffraction grating 600 lines/mm, objective Olympus MPlan 10x, 633 nm laser at 12 mW power. The detector used is a nitrogen-cooled Symphony OE.

A backscattering signal was used while focusing on the center of the waveguide end face, with an optical axis parallel to waveguide.

All spectra were corrected for baseline using built-in Labspec 6 software. For mean +- standard deviation representation, 5 measurements of the same sample were averaged

Chapter 4. HC-MOW application for Raman spectroscopy of liquid samples

In this chapter, application of HC-MOW to Raman spectroscopy is described. For that, the analytes in the form of aquaeous solutions of two molecules were taken: a relatively small organic molecule R6G (479 Da[182]) and a much larger biological molecule BSA(66.5 kDa[183]).

This chapter is a combination of the material published by the author in two research articles:

a) In part with R6G, [25] **A.A. Merdalimova**, P.G. Rudakovskaya, T.I. Ermatov, A.S. Smirnov, S.S. Kosolobov, J.S.Skibina, P.A. Demina, B.N. Khlebtsov, A.M. Yashchenok, D.A. Gorin, SERS Platform Based on Hollow-Core Microstructured Optical Waveguide: Technology of UV-Mediated Gold Nanoparticle Growth. Biosensors, 2022,

12, 19. https://doi.org/10.3390/bios12010019 (IF=5.519, Q1). All Raman measurements and data curation was provided by the thesis author.

b) A part with BSA, [26] **A. Merdalimova**, V. Vorobev, R. Barmin, A.Aleksandrov, D. Terentyeva, T. Estifeeva, S. German, V. Chernyshev, O. Maslov, Y. Skibina, P.Rudakovskaya, D. Gorin, Two-in-One Sensor of Refractive Index and Raman Scattering using Hollow−Core Microstructured Optical Fibers for Colloid Characterization. Colloids Surfaces B, 2023 (under revision, submission number COLSUB-D-23-02310). Raman measurement supervision and all data curation were provided by the thesis author, supported with measurements implemented by Artem Aleksandrov.

The experimental setup for Raman measurements in HC-MOW is demonstrated in Figure 4-1 [27]. The HC−MOW is fixed vertically by a waveguide clip. The waveguide bottom end is dipped in the liquid that fills the cavities inside via capillary forces. The objective of Raman spectrometer is focused to the center of the liquid in the top waveguide end. Raman signal is collected in a backscattering mode.
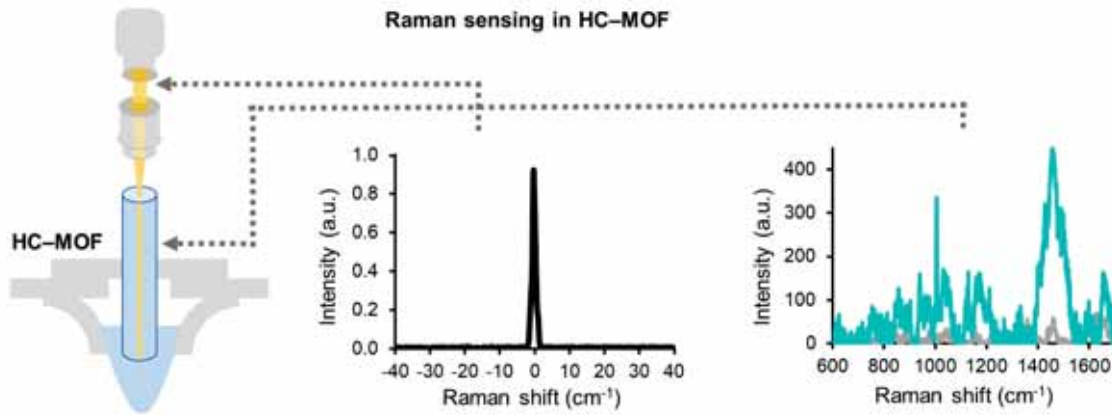
Figure 4-1. A setup for Raman scattering measurement in a HC−MOW. One end of HC−MOW is dipped in the analyte, so the liquid fills the whole waveguide, and the objective of the Raman spectrometer is focused to the liquid surface on another waveguide end. The signal is collected in a backscattering mode, so the initial, narrow−band laser irradiation (depicted on the left plot) and Raman scattered signal (depicted on the right plot).

4.1. Rhodamine 6G aqueous solution

Firstly, Raman spectra of R6G on a drop on a planar substrate and in the HC-MOW[25] were compared. The spectra are demonstrated on Figure 4-2. One may conclude that using HC-MOW is beneficial for Raman intensity: R6G with concentration 0.2 mM is distinguishable in HC-MOW, meanwhile, it wasn't on planar slides; if to calculate "waveguide analytical Raman enhancement factor", taking into account signal amplitudes and concentrations, 50x enhancement was obtained. This may be explained by a larger effective volume of analyte undergoing Raman scattering due to waveguiding properties of HC-MOW. Meanwhile, the large height of liquid analyte in HC-MOW is provided by a sample volume of around 1.1 µL in the hollow core with 2.5 cm length.
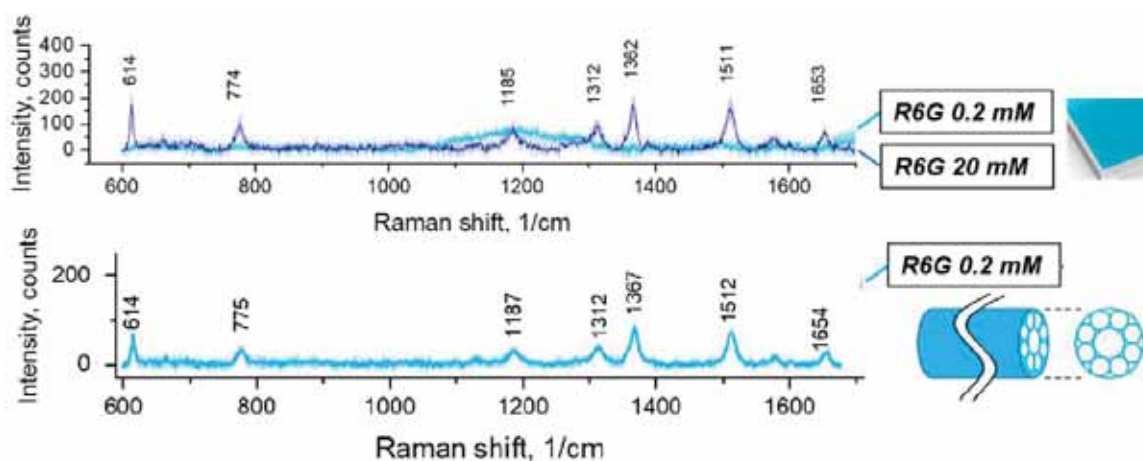
Figure 4-2. Raman spectrum of Rhodamine 6G (R6G) on a drop a planar substrate and in the HC-MOW.

4.2. BSA aqueous solution

Next, one of the simplest and popular model biological analytes, BSA, is taken as an analyte. Compared to R6G, it possesses much greater molecular weight, and at concentrations applicable for optical sensing and close to physiological values (dozens of mg/mL) BSA is more dense and possesses greater refractive index, viscosity and is prone to drying on air, obtaining a crust on the surface.

Figure 4-3a demonstrates Raman spectra of BSA measured in the HC−MOW presented in Figure 4-1. Raman spectra BSA peak assignments for BSA are presented in Table 4-1. In selecting the peak that is best for simple univariate tracing, without additional peak shape fitting, the preferred one should possess a relatively high amplitude to avoid errors from noise. Additionally, a narrow shape is preferred to prevent amplitude distortion during software-based background correction and no spectral overlap. Based on these criteria, for BSA the peak at 1004 cm^{-1} was chosen, corresponding to phenylalanine ring breathing mode[184,185]. The dependence of the peak intensity on the BSA concentration and its linear approximation is demonstrated in Figure 4-3Figure 4-3b; similar measurements in a bulk solution and a drop on a planar substrate are demonstrated in Figure 4-3c,d.

65

It is worth noting that for the last two dependencies no signal increase was detectable with concentration increase until concentration 20 mg/mL is reached. ANOVA and further post-hoc testing (Tukey's HSD) showed that the null hypothesis could not be rejected when comparing the 5, 10, and 20 mg/mL concentrations, so the first two concentrations were not included in the linear fit. The obtained sensitivities for measurement in a tube and on a wafer are 4.53 mL/mg and 2.81 mL/mg, respectively, demonstrating a higher sensitivity of Raman measurement in HC-MOW. Therefore, for these linear fittings only 20 mg/mL and higher concentrations are used.

As a result, for all three line fittings, $p-value$ is less than 0.001, R^2 is 0.950 for HC-MOW and bulk solution, and R^2 is 0.757 for the drop. Thus, the Raman peak intensity linearly depends on concentration, analogously to RI dependence on concentration. As for the sensitivity, that is the line slope in the present plots, it is 6.44, 4,53 and 2.81 for the measurements in HC-MOW, bulk medium and in a drop, respectively. Thus, the sensitivity in a HC-MOW is 1.4x greater than in a bulk solution and 2.3x greater than in the drop.
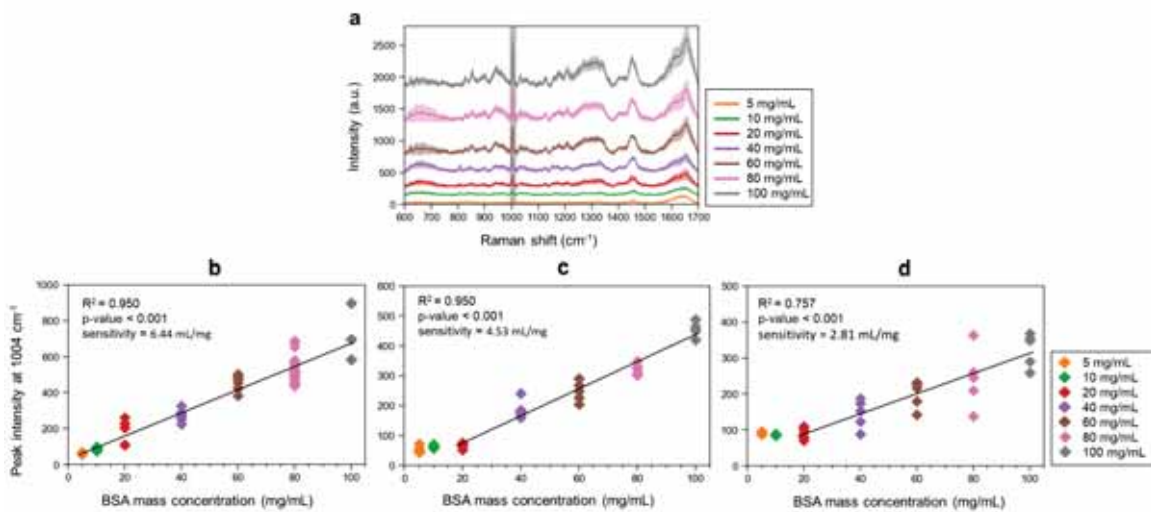
Figure 4-3. BSA monocomponent solution Raman spectroscopy measurements: (a) in HC-MOW, (b) in a bulk solution, (c) in a drop on a planar substrate. Reproduced with adjustments from [26]

Table 4-1. Raman peaks assignment for BSA monocomponent solution

Raman shift (cm^{-1})	Corresponding assignment	Reference
622	Phenylalanine phenyl ring breathing, Tyrosine C−S stretch	[184], [185], [186]
644	Tyrosine C−S stretch	[185,186]
830	Tyrosine, out−of−plane C−H bond motion	[184,186]
851	Tyrosine, in−plane ring breathing mode, Proline, C−C ring stretch	[184,186]
880	Tryptophan aromatic residue	[187]
942	C−C−N symmetric deformation, alpha−helical skeletal	[185,186]
1004	Phenylalanine, C−C aromatic ring stretch	[185,186]
1030	Phenylalanine, CH_2−CH_3 bending, C−C vibration	[187]
1130	C−N stretch	[185,186], [188]
1210	Phenylalanine, Tyrosine: side chain (C_β−C_γ) stretch coupled with the in−phase motion of ($C_{\delta1}$−$C_{\varepsilon1}$) stretch and ($C_{\delta2}$−$C_{\varepsilon2}$) stretch	[185,186]
1240−1350	Amide III, peptide chain secondary structure, coupled C–N stretch and N–H bending vibrations of the peptide group	[184], [187]
1450	CH_2/CH_3 deformation	[185,186]
1656	Amide I, stretch vibration of C=O	[185,186]

4.3. Summary

Raman spectra of liquid analytes possess greater intensity ~~of Raman peaks~~ when measured in a HC-MOW rather than in a drop. This is in agreement with the previously published works [16,189,190]. However, it is worth noting that different analytes provide different fiber enhancement. So, in the present experiment R6G demonstrated up to 50x

fiber enhancement, meanwhile BSA was capable of just 2.3x enhancement. That may be explained by a number of factors, such as: BSA dried crust formation on the surface due to long measurement; increased BSA refractive index (will be discussed further in the present work) compared to R6G, that leads to less ratio between core and cladding, hence decreased reflection and finally decreased waveguiding efficiency.

However, the established values of fiber enhancement are promising and therefore the research is continued on sensing in HC-MOW, using Raman spectroscopy and combining it with other methods, as will be elaborated in further chapters.

Chapter 5. SERS substrates based on HC-MOW

The present chapter aims at developing a novel approach for the easy preparation of SERS substrate inside HC-MOW. The results were published in [25] **A.A. Merdalimova**, P.G. Rudakovskaya, T.I. Ermatov, A.S. Smirnov, S.S. Kosolobov, J.S.Skibina, P.A. Demina, B.N. Khlebtsov, A.M. Yashchenok, D.A. Gorin, SERS Platform Based on Hollow-Core Microstructured Optical Waveguide: Technology of UV-Mediated Gold Nanoparticle Growth. Biosensors, 2022, 12, 19. https://doi.org/10.3390/bios12010019 (IF=5.519, Q1). All surface modification, SERS measurements and data curation was provided by the thesis author.

Firstly, a concept of the present SERS substrate fabrication on glass slides was proved. The planar SERS substrates were fabricated by the author using a two-step UV-mediated chloroauric acid reduction on gold seeds and compared their SERS enhancement with the substrates made by one-step absorption of larger AuNPs. This comparison demonstrated the efficiency of the developed 2-step method. Then the technology was transferred to HC-MOWs. A method for SERS substrate deposition process control in HC-MOW was introduced, based on the change in its transmission spectra.

5.1. SERS substrates on planar slides

5.1.1. Surface modification by plasmonic nanoparticles

Firstly, SERS active substrates on planar objective slides were fabricated. For that, two types of AuNPs were compared: small AuNPs (gold seeds) stabilized with THPC [180] and larger AuNPs stabilized with citrate, synthesized by a modified Turkevich method [181]. TEM and DLS characterization of these two types of AuNPs are provided in Figure 1. According to DLS (Figure 5-1), gold seeds have a mean diameter and standard deviation of 8.0 nm and 1.4 nm, respectively; AuNPs stabilized with citrate have a mean diameter and standard deviation of 33 nm and 11 nm, respectively. However, according to DLS, AuNPs stabilized with citrate have a fraction with a size of around 1 nm. TEM image (Figure 1b) also contains a few objects much smaller in size than the main fraction. The main hypothesis is that they are citrate gold seeds.
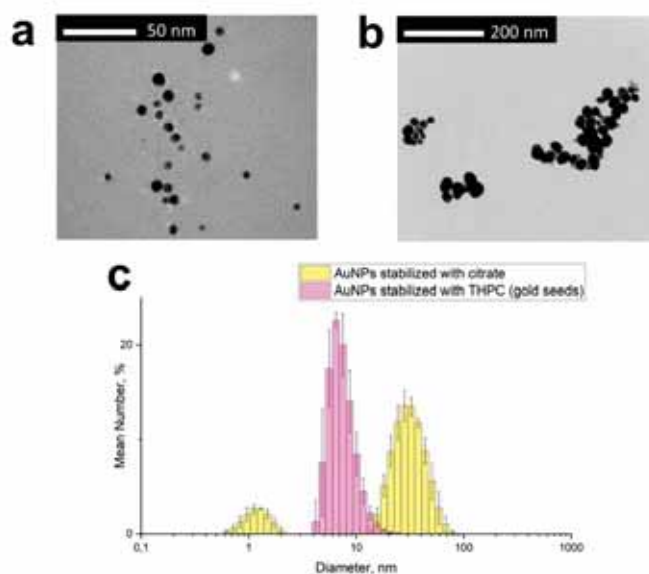
Figure 5-1. Characterization of AuNPs: (a) transmission electron microscopy (TEM) image of THPC gold seeds; (b) TEM image of AuNPs stabilized by citrate (yellow color); (c) size distribution histogram of gold seeds stabilized by THPC and AuNPs stabilized with citrate (pink color), revealed by dynamic light scattering (DLS). Reproduced from [25]

69

To compare Raman and SERS signal, three types of samples were fabricated, as illustrated in Figure 5-2: bare glass slide (sample Slide-Bare); glass slide functionalized with PEi and citrate-stabilized AuNPs (sample Slide-AuNP); glass slide functionalized with PEi and UV-mediated chloroauric acid reduction on gold seeds (sample Slide-Au-UV). Initially, objective glass slides were taken and etched with plasma to clean the surface and to get hydroxyl groups on the glass surface. Then slides were covered with PEi to obtain a positive surface charge which is necessary for further efficient electrostatic absorption. Then two types of negatively charged AuNPs (stabilized with citrate and with THPC) were adsorbed on slides by incubation and thus samples Slide-AuNP and Slide-Au-Seeds were obtained, respectively. The last step was Slide-Au-Seeds improvement to Slide-Au-UV by UV-mediated reduction of HAuCl4 in citrate presence.
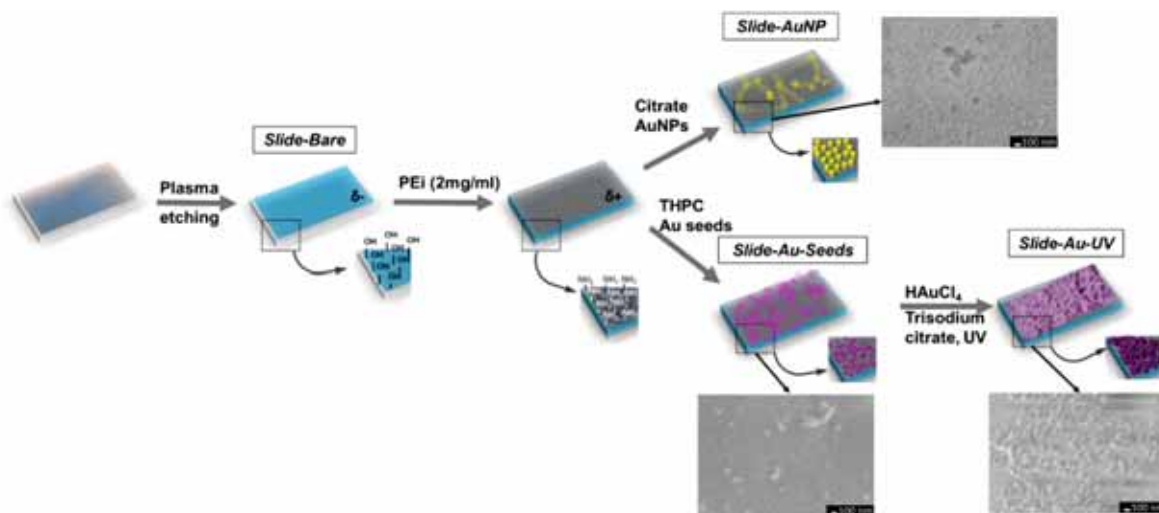
Figure 5-2. The fabrication process of SERS-active substrates on glass slides with scanning electron microscopy (SEM) images incorporated. The scale bar is 100 nm. Reproduced from [1]

As it can be noticed from SEM images incorporated into Figure 2, the sample Slide-Au-Seeds is covered with small AuNPs and in some places with their aggregates. The sample Slide-AuNP is covered with larger AuNPs more intensively, although gold mass concentration here is of the same order as in Slide-Au-Seeds, and taking into account particle sizes, concentration by particle number is even less than for the sample Slide-Au-

Seeds. After UV-mediated gold reduction, the obtained sample Slide-Au-UV has a significant increase in the size of gold nanostructures on its surface compared to the previous state on the sample Slide-Au-Seeds.

5.1.2. SERS measurements

To prove Raman signal enhancement, R6G as a model Raman reporter was used [191–193]: 2 µL of 0.2 mM R6G aqueous solution was placed dropwise on the prepared substrates. The comparison was provided with R6G spectra measured in Chapter 4.1.

For a simple substrate comparison, an analytical enhancement factor (EF) was calculated as follows[194]:

$$EF = \frac{\frac{I_{SERS}}{c_{SERS}}}{\frac{I_R}{c_R}},$$ (5-1)

where c_R, c_{SERS} are R6G concentrations during Raman (at a bare substrate) and SERS measurements, and I_R, I_{SERS} are their intensities, respectively, pairwise for each Raman peak considered.

For a general EF estimation for the substrates, Raman modes at 1362 and 1509 cm^{-1} were used, as they correspond to benzene ring stretching and are the most prominent ones. The sample Slide-Au-Seeds didn't demonstrate any signal from 0.2 mM R6G. The sample Slide-AuNP formed by 33 nm citrate-stabilized AuNPs demonstrated EF around $0.8*10^3$, meanwhile, the sample Slide-Au-UV, using UV-mediated chloroauric acid reduction, demonstrated EF $1.3*10^4$.

Therefore, UV-mediated chloroauric acid reduction on gold seeds demonstrated its potential in improving SERS signal, and this approach was adopted in HC-MOW, due to the ability of HC-MOW to integrate signal across the entire length with low-volume sensing and to mitigate a problem of sample volume change during measurements [15,195,196].
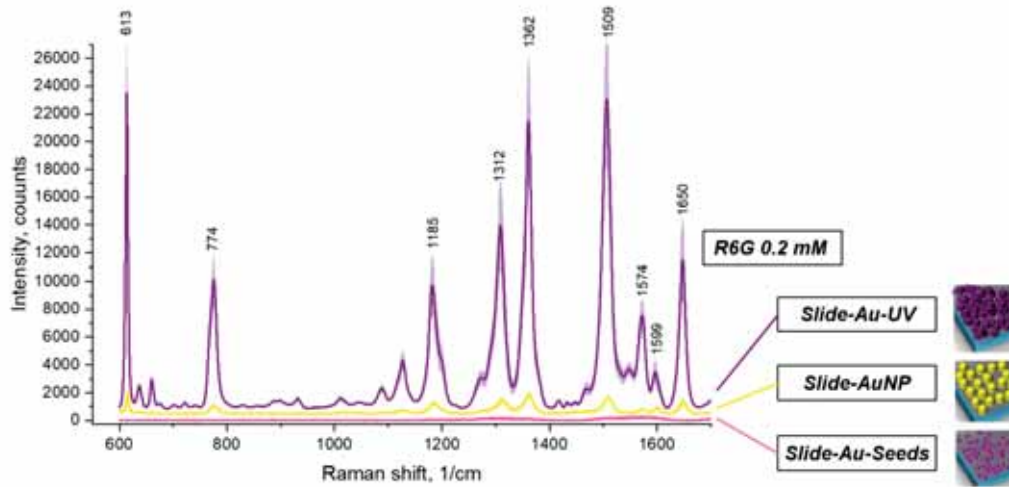
Figure 5-3. SERS of 0.2 mM Rhodamine 6G on planar plasmonic substrates. Reproduced from [1]

5.2. SERS in HC-MOW

5.2.1. Fabrication and layer deposition control

Sample fabrication is illustrated in Figure 5-4. Similar to the technology used for slides, firstly HC-MOWs were treated with plasma to clean and to get hydroxyl groups on waveguide walls. Then HC-MOWs were functionalized with PEi using a peristaltic pump to obtain a positive surface charge which is necessary for further efficient electrostatic absorption. Then, using the same peristaltic pump, AuNP seeds stabilized with THPC were electrostatically adsorbed, thus the sample MOW-Au-Seeds was obtained. The last step was MOW-Au-Seeds improvement to MOW-Au-UV by UV-mediated reduction of HAuCl4 in citrate presence.

SEM images of the waveguide tip on different steps of the functionalization are incorporated into Figure 5-4.

72
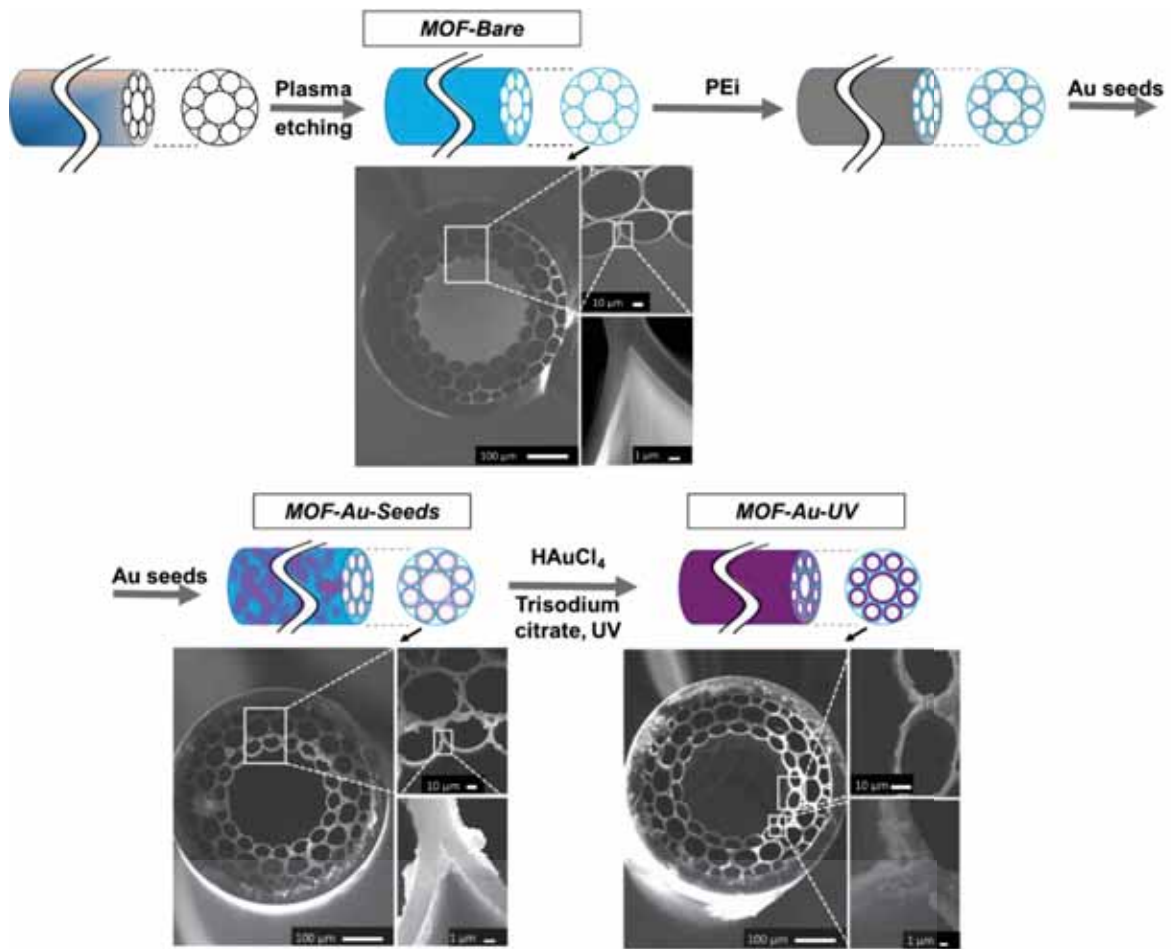
Figure 5-4. The fabrication process of SERS-active HC-MOWs with SEM images incorporated. Reproduced from [1]

While developing a novel technology for HC-MOW-coating, it is needed to evaluate performance. Layer deposition control using SEM images has several disadvantages. One image provides information about just one cross-section at the moment, on the examined waveguide tip. As it was demonstrated, the SEM imaging of the tip is not representative and waveguides need to be broken up for coating control. Besides that, SEM equipment is expensive, its usage is laborious and requires special skills, and is ~~usually~~ not routinely available. Furthermore, since most of the commercial waveguides are made of silica and

its counterparts, an extra deposition of conductive metals required for the proper imaging decreases the contrast between waveguide walls and functional coating and does not allow resolving nanometer-thin films [197]. An optical setup for transmission spectra measurement of HC-MOWs [14] solves this problem: spectral data provide integral information about HC-MOW geometry. Moreover, this optical setup is quite compact, is quickly mounted from common optical components, and is simple in use. The mechanism of light guidance in the employed HC-MOWs can be described by the model of Fabry–Perot resonances and antiresonances in the wall of the central capillary [13,198].

Figure 5-5a demonstrates transmission spectra for a single HC-MOW at all stages of the surface functionalization. For quantitative analysis, positions of minima min1...min4 were chosen, as earlier and later spectral components have lower signal-to-noise ratios, which may affect the accuracy of minima position determination. In Figure 5-5b, calculations of shifts in positions of transmission minima are presented for all stages of layer deposition cumulatively. It is worth noting that these shifts depend on additional optical path lengths experienced by a divergent beam inside the HC-MOW, and the optical path length depends both on refractive index and layer thickness. However, with wavelength increasing, the distance between minima becomes greater in a single spectrum, and the same optical path lengths lead to greater shifts in transmission spectra. This phenomenon compensates (and even overcompensates) the fact that the refractive index of gold in the visible range is mainly decreasing with increasing wavelength [199].
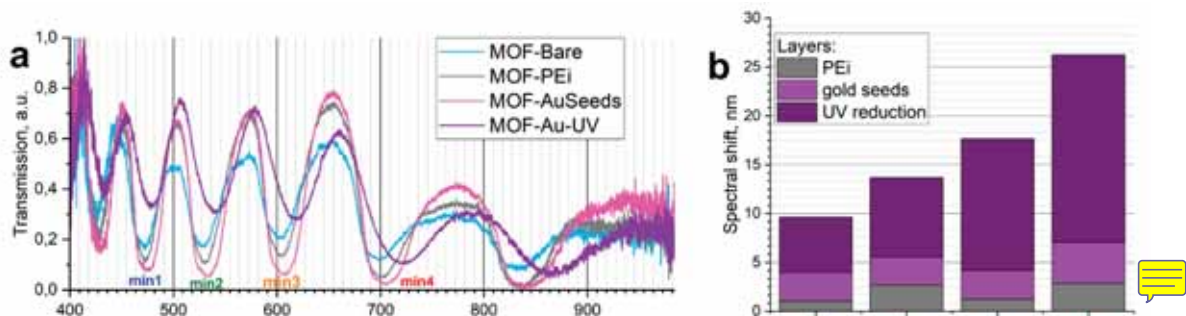
Figure 5-5. Shifts in transmission spectra induced by coatings: (a) transmission spectra of a single HC-MOW at all stages of layer deposition, with positions of minima selected for analysis labeled as min1...min4 ; (b) shifts in transmission spectra induced to 1 waveguide cumulatively by PEi, gold seeds, and UV-mediated chloroauric acid reduction.

5.2.2. SERS measurements

Functionalized HC-MOW demonstrates SERS enhancement with an analytical EF around 10x. The analytical EF for the present SERS substrate in HC-MOW is around 10x, which is lower than for the SERS substrate with the same fabrication technology but on planar slides. The main hypothesis is that although the SERS substrate area reached by laser irradiation in HC-MOW is greater than a planar substrate, the efficiency of scattering signal collection by an objective is lower in this case. Nanostructured gold coating on inner waveguide walls does not only enhance Raman scattering signal but scatters incident radiation in multiple directions at the same moment. Therefore, compared to the planar substrate irradiation, a smaller part of the generated signal (only backscattered to objective aperture) is collected by the Raman spectrometer. This problem may be solved by installing a mirror on the waveguide tip opposite to the illumination and signal collection side. Furthermore, as could be noticed in Figure 5-6, initially HC-MOWs were chosen so that laser wavelength of 633 nm is around the maximum of the waveguide transmission. But after UV-mediated gold reduction, the HC-MOW transmission spectrum shifted in such a way that 633 nm is around the minimum of the waveguide transmission, which is not an optimal choice and further studies are needed on HC-MOWs that possess maximum transmission on 633 nm after SERS substrate formation. Also, further improvement of the developed technology of gold deposition to HC-MOW may be provided. In particular, the developed UV-mediated gold reduction in HC-MOW could be combined with further annealing[200].
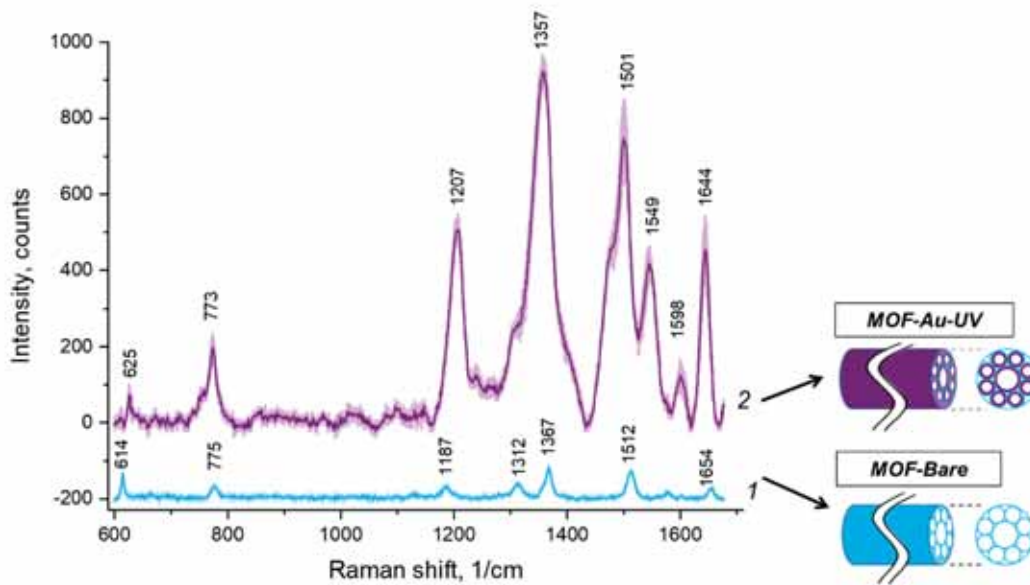
Figure 5-6. Raman and SERS of R6G in HC-MOW: 1 – bare HC-MOW; 2 – HC-MOW with UV-mediated chloroauric acid reduction on gold seeds. Reproduced from [1]

5.3. Summary

A technology of a multistep SERS substrate fabrication in HC-MOF using UV-mediated gold nanoparticle growth and layer deposition control was estimated. Due to HC-MOW features of light transmission, efficiency of substrate grow on the inner walls may be monitored.

Functionalized HC-MOW demonstrates SERS enhancement with an analytical EF around 10x. The analytical EF for the present SERS substrate in HC-MOW is around 10x, which is lower than for the SERS substrate with the same fabrication technology but on planar slides. The main hypothesis that although the SERS substrate area reached by laser irradiation in HC-MOW is greater than planar substrate, the efficiency of scattering signal collection by an objective is lower in this case. Nanostructured gold coating on inner waveguide walls does not only enhance Raman scattering signal but scatters incident radiation in multiple directions at the same moment. Therefore, compared to the planar substrate irradiation, a smaller part of the generated signal (only backscattered to objective

76

aperture) is collected by the Raman spectrometer. This problem may be solved by installing a mirror on the waveguide tip opposite to the illumination and signal collection side.

Furthermore, as could be noticed in Figure 6-9, initially HC-MOWs were chosen so that laser wavelength of 633 nm is around the maximum of the waveguide transmission. But after UV-mediated gold reduction, the HC-MOW transmission spectrum shifted in such a way that 633 nm is around the minimum of the waveguide transmission, which is not an optimal choice and further studies are needed on HC-MOWs that possess maximum transmission on 633 nm after SERS substrate formation. Also, further improvement of the developed technology of gold deposition to HC-MOW may be provided. In particular, the developed UV-mediated gold reduction in HC-MOW could be combined with further annealing[200].

However, it is worth noting that the UV gold reduction possesses stable adhesion on glass slides, meanwhile in HC-MOW the adhesion stability is poor. Therefore, further investigations should be made to gain a stable SERS substrate grow in HC-MOW.

Chapter 6. Two-in-one refractive index and Raman scattering sensing of colloids in HC-MOW

In this chapter, the methods of multispectral refractive index and Raman scattering sensing in HC-MOW are joined, and used for more complicated structures. The results were presented in the paper [26] A. Merdalimova, V. Vorobev, R. Barmin, A.Aleksandrov, D. Terentyeva, T. Estifeeva, S. German, V. Chernyshev, O. Maslov, Y. Skibina, P.Rudakovskaya, D. Gorin, Two-in-One Sensor of Refractive Index and Raman Scattering using Hollow−Core Microstructured Optical Fibers for Colloid Characterization. Colloids Surfaces B, 2023 (under revision, submission number COLSUB-D-23-02310). Raman and RI measurements and data curation were provided by the thesis author, with analytes synthesized by the team of T.Estifeeva, D.Terentyeva, O.Maslov headed by P.Rudakovskaya; the scripts for RI calculation were developed by the thesis author and V.Vorobyev.

6.1. Methodology of two-in-one measurement in HC-MOW

RI sensing is based on the HC−MOW ability to transform a broadband light spectrum to a quasi−periodic pattern. The setup for multispectral RI sensing is schematically presented in Figure 6-1a. The HC−MOW is fixed horizontally by two liquid cells, providing along with a waveguide a hermetic channel for liquid analyte flow introduced by a peristaltic pump. Furthermore, an optical setup includes a lamp as a broadband light source, whose irradiation is focused to the first HC−MOW tip. The liquid cells have transparent borosilicate glass windows to allow light passing. In HC−MOW, different modes propagate with different efficiency, therefore the light spectrum after passing the HC−MOW differs from initial one and gains a sinusoid−like shape. The positions of transmission minima are related to resonant positions in a waveguide, at which modes leak effectively. To perceive and analyze the spectrum, the light coming out from the second waveguide tip after interacting with the liquid analyte is collected by two objectives and sent to the spectrometer input.
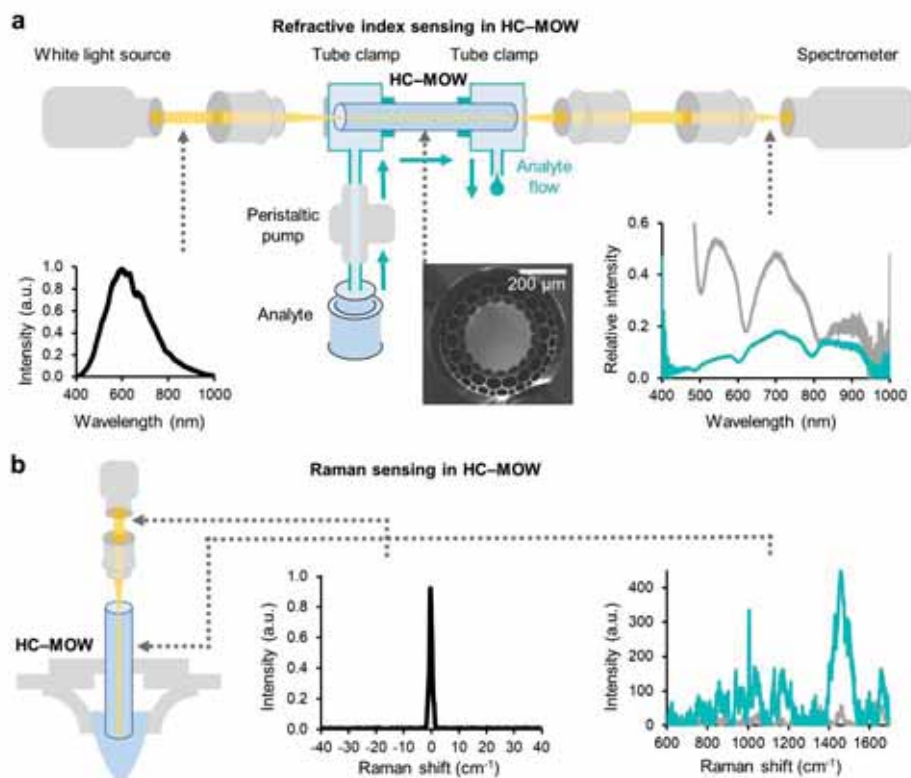
*Figure 6-1. Scheme of the HC−MOW setup for two−in−one refractive index and Raman scattering measurements of analytes. (**a**) A setup for transmission measurement and RI sensing in a HC−MOW (adapted with additions from Ermatov et al.[14]). The left incorporated graph corresponds to light source spectrum, the right graph corresponds to light spectrum after the HC−MOW (grey line for aqueous solution and cyan line for BSA@P(VP−AA) [3:1] complex). The scanning electron microscopy image of the HC−MOW cross−section is adapted from our previous work.[25] (**b**) A setup for Raman scattering measurement in a HC−MOW. Initial narrow−band laser irradiation is depicted on the left plot, and Raman scattered signal is depicted on the right plot, grey line for aqueous solution and cyan line for BSA@P(VP−AA) [3:1] complex. Reproduced from [26]*

The left inset graph in Figure 6-1a depicts the input spectrum of lamp, while the right inset graph shows output transmission spectra after HC−MOW for water (gray line) and

BSA@P(VP−AA) complexes with the protein and copolymer ratio of 3:1 and the total mass concentration of 50 mg/mL (cyan line), highlighting periodical transmission pattern of the HC−MOW for both substances but possessing different positions of transmission minima and different intensity patterns for these two substances. HC−MOW structure is reflected on the incorporated scanning electron microscopy image adapted from our work with a similar HC−MOW.[25]

The structures used for the study have a diameter of 240 μm of the central capillary and a thickness of the first wall of 1.8 − 2 μm. The main part of the light is ~ 87 % guided inside the central capillary and approximately ~13 % in the first layer of adjacent capillaries. Therefore, it is possible to describe the mechanism of light propagation on the basis of the Fabry−Perot resonances model[13,198], and the transmission spectrum of such structures has minima with wavelengths described:

$$\lambda_{jmin} = \frac{2d}{j}\sqrt{n_2^2 - n_1^2}, \quad (6\text{-}1)$$

where j is an integer describing the capillary mode order (j = 1, 2, 3, …), n_1 indicates RI of an analyte filling the capillaries, n_2 is the RI of the waveguide material, and d describes its capillaries wall thickness. The positions of the minima are estimated using a centroid function.

Thus, the RI of the solution inside the HC−MOW can be determined from the position of the minimum in the transmission spectrum of the filled waveguide, the thickness of the glass, its RI, and the capillary mode order.

Firstly, the glass thickness is determined from the transmission spectrum of an air−filled HC−MOW. Local minima and their positions are located on the spectra, after which, using the least squares method, the thickness of the waveguide walls can be determined. The RI of glass at different wavelengths, *i.e.,* dispersion curve for waveguide glass was obtained from Noskov *et al.*[198]. Furthermore, based on the measured HC−MOW transmission spectra filled with different solutions, the positions of the local

minimum can be found, and from the ratio of their wavelengths, the capillary modes order (*i.e.*, j) is obtained for each of the tracked minima. Thus, this procedure provided us with the entire set of required data within the model for determination of the RI of the solution filling the HC−MOW. For calculations, the RI of glass was interpolated to values determined by the positions of the minimum.

To evaluate RI sensing performance, RI sensitivity (RIS) is estimated, which is the ratio of the change in sensor output (in our case, the shift of the resonant wavelength) to the variation in RI of the analyte. Equation (6-2) evaluates RIS value as an analytical dependence of the wavelength derivative on the refractive index of analyte:

$$RIS = \frac{\partial \lambda_{jmin}}{\partial n_1} = \frac{\partial \left(\frac{2d}{j} \sqrt{n_2^2 - n_1^2} \right)}{\partial n_1} = -\frac{2 n_1 d}{j \sqrt{n_2^2 - n_1^2}} \quad (6\text{-}2)$$

For each initial minimum position, it is possible to obtain RI of the material inside HC−MOW that will correspond to the shift in the location of the minimum:

$$n_1(\lambda_0, \delta\lambda) = n_1(\lambda_0) + \frac{\partial n_1}{\partial \lambda} \delta\lambda \quad (6\text{-}3)$$

This approach allows to calculate the RI of the material inside the waveguide knowing the experimental shift in the spectrum, or, on the other hand, to calculate what spectral shift should be expected in experimental measurements with a material of known refractive index. From this point of view, the lower limit of detection is determined by the experimental measurement error, which should be less than the expected spectral shift.

The experimental measurements conducted in determining the wavelength of the minimum reveal an approximate error of 2 nm or less. According to Equation (6-3), this error translates to the minimum deviation of the RI value that can be detected using this method being approximately 0.001.

Figure 6-2 illustrates RIS evaluations for a set of capillary mode orders $j = 5, 4, 3$, that correspond to wavelength minima positions further referred as *min 1, min 2, min 3*. In the

RI range described in the manuscript, our RIS value turns to be around 2000 nm / RIU, that is consistent with optical RI 2D sensors described in the literature[201,202]. Higher values, such as tens of hundreds of nm/RIU, are reported for waveguide SPR sensors, interferometer sensors and others setups[201], however, they are more expensive and involve additional complicated fabrication steps compared to our design. Meanwhile, the presented sensor on HC−MOW is simply designed and inexpensive, yet the precision of concentration measurement on it (as will be demonstrated in the further text) is less than ± 5 mg/mL, which is appropriate for certain non−demanding applications where the possibility of in−flow measurement is in the first place.
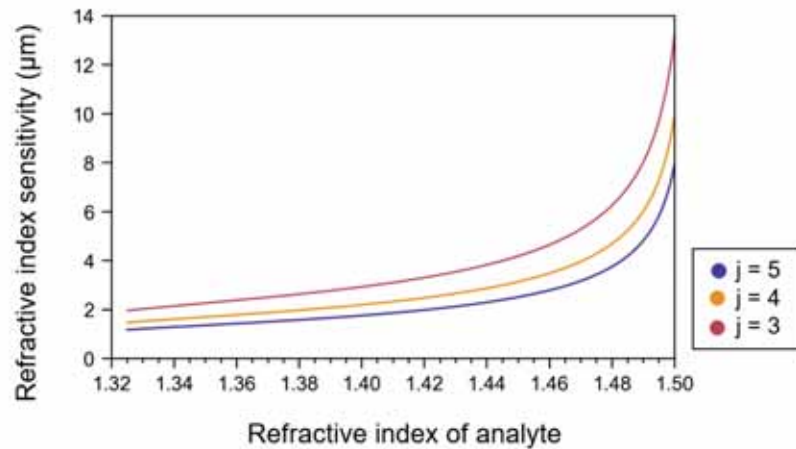
Figure 6-2. Refractive index sensitivity: analytical dependence of the wavelength derivative on the refractive index of analyte for a set of capillary mode orders j. Reproduced from [26].

The setup designed for Raman scattering is presented in Figure 6-1b. The HC−MOW is fixed vertically by a waveguide clip. The waveguide bottom end is dipped in the liquid that fills the cavities inside via capillary forces. The objective of Raman spectrometer is focused to the center of the liquid in the top waveguide end. Raman signal is collected in a backscattering mode.

6.2. BSA and P(VP-AA) bulk solutions

To assess the two−in−one RI and Raman sensing capabilities of the HC−MOW setup, BSA and P(VP−AA) monocomponent solutions are measured with a set of varied concentrations. Corresponding RI and Raman scattering measurements of BSA aqueous solution are demonstrated in Figure 6-3.

Figure 6-3a shows transmission spectra of BSA monocomponent solutions measured in the HC−MOW setup presented in Figure 6-1a. To calculate RI values, firstly a transmission spectrum of an empty HC−MOW is used to estimate the particular wall thickness d for an individual waveguide, according to the Equation (6-1). The obtained thickness values are 1.8 − 2 µm, which is consistent with the estimation from scanning electron microscopy images. Furthermore, with the calculated precise value of the wall thickness, the same Equation (6-1) is used for RI estimation of liquid solutions introduced into the waveguide based on the transmission spectra. For that, the wavelength positions corresponding to transmission minima are determined and named *min 1, min 2, min 3*, corresponding to wavelength ranges around 500, 600, 800 nm, which in their turn refer to capillary mode orders 5, 4, 3, respectively. Thus, RI values for these wavelengths are calculated according to Equation (6-1) and presented in Figure 6-3b. As the wavelength increases from *min* 1 to *min* 3, the RI values decrease, which is consistent with a typical dielectric dispersion curve in the visible optical region.[203,204] For each minimum, RI dependence on concentration is approximated with a linear regression. For all three minima, R^2 values are 0.999 and *p−values* are less than 0.05 (with the highest value of 0.003), so the RI dependence on concentration is linear and statistically significant for all three regions. Therefore, the present method is applicable for indirect BSA concentration measurement.
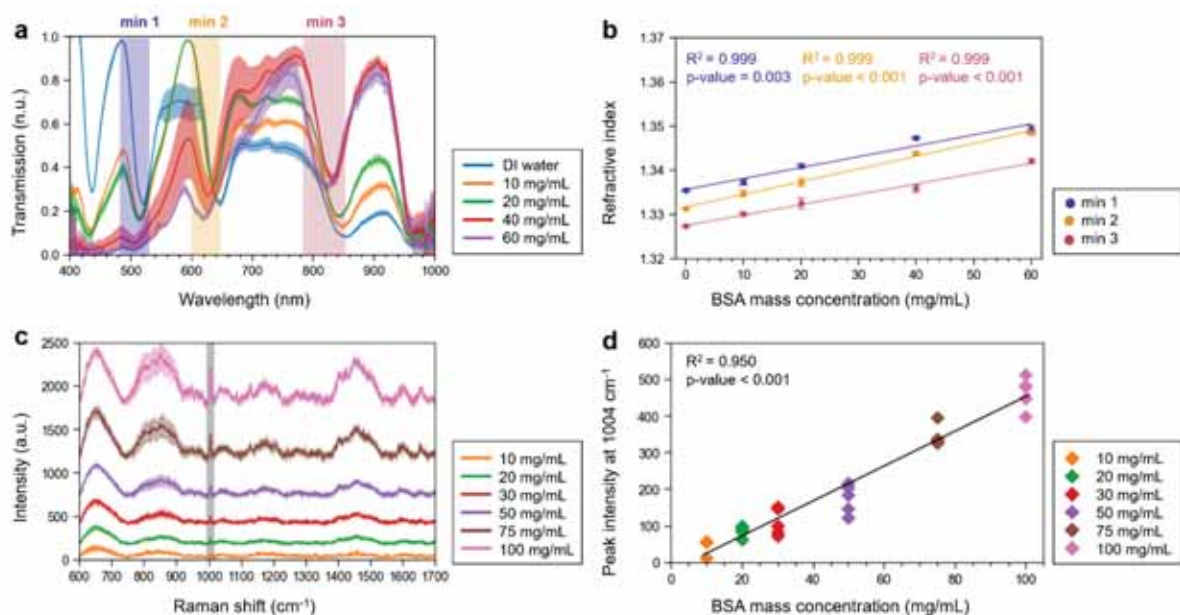
Figure 6-3. BSA monocomponent solution RI and Raman spectroscopy measurements. (a)
Transmission spectra of HC−MOW with BSA aqueous solutions with concentrations of 10, 20,
40, and 60 mg/mL compared to DI water demonstrate 3 spectral regions (min 1, min 2, min 3)
*with anti−resonant minima positions, that can be used to extract RI values. (**b**) Linear*
dependence of the corresponding RI values of BSA aqueous solutions extracted from the 3
*anti−resonant minima positions on the BSA mass concentration. (**c**) Raman spectra of*
HC−MOW with BSA aqueous solutions with concentrations of 10, 20, 30, 50, 75 and 100
mg/mL provide a set of characteristic Raman peaks. Raman peaks assignment for BSA
*monocomponent solution is presented in Table S1. (**d**) Linear dependence of the corresponding*
Raman peak intensities at 1004 cm^{-1} Raman shift of BSA aqueous solutions. Reproduced from
[26]

As was mentioned earlier in this chapter, the minimum deviation of refractive index
that can be detected is 0.001 RIU. According to the built linear regressions, the line slopes
are 2.47×10^{-4} RIU × mL/mg, 2.88×10^{-4} RIU × mL/mg, and 2.35×10^{-4} RIU × mL/mg

for *min 1*, *min 2*, *min 3*, respectively, that corresponds to maximum 4.25 mg/mL deviation of concentration of BSA.

Figure 6-3c demonstrates Raman spectra of BSA monocomponent solutions measured in the HC−MOW setup design presented in Figure 6-1b. Raman spectra BSA peak assignments for BSA are presented in Table 4-1. Choosing the peak that is the most convenient for simple univariate tracing (without additional peak shape fitting), the one preferred possessing relatively high amplitude to avoid high error due to noise, narrow shape to avoid amplitude distortion during software−based background correction, and absence of spectral overlap. Based on these criteria, for BSA the peak at 1004 cm^{-1} is chosen, corresponding to phenylalanine ring breathing mode.[184,185] The dependence of the peak intensity on the BSA concentration and its linear approximation is demonstrated in Figure 6-3d. For the line fitting, R^2 is 0.950 and $p-value$ is less than 0.001, so the Raman peak intensity linearly depends on concentration, analogously to RI dependence on concentration. The slope of the fitted line corresponds to a sensitivity of 6.44 mL/mg for BSA in HC-MOW.

Similarly to BSA, RI and Raman spectroscopy measurements for P(VP−AA) are provided in Figure 6-4. Figure 6-4a shows transmission spectra of P(VP−AA) monocomponent solutions measured in the HC−MOW setup presented in Figure 6-1a. For RI extraction, wavelength positions corresponding to transmission minima are determined and named *min 1*, *min 2, min 3*, corresponding to wavelength ranges around 500, 600, 800 nm and capillary mode orders 5, 4, 3, respectively. RI for these wavelengths are calculated according to Equation (6-1) and presented in Figure 6-4b. For each minimum, RI dependence on concentration is approximated with a linear regression. For all three minima, R^2 values are 0.999 and $p-values$ are less than 0.001, so the RI dependence on concentration is linear and statistically significant for all three regions. Therefore, the present method is applicable for indirect P(VP−AA) concentration measurement.

According to the built linear regressions, the line slopes are 2.21 × 10^{-4} RIU × mL/mg, 2.08 × 10^{-4} RIU × mL/mg, and 2.25 × 10^{-4} RIU × mL/mg for *min 1*, *min 2*, *min 3*,

respectively (all sensitivity estimations are summarized in Table S3), that corresponds to maximum 4.8 mg/mL deviation of concentration of P(VP−AA). Thereby, both BSA and P(VP−AA) demonstrated linear dependence of the measured refractive index on concentration, with deviation below 5 mg/mL.

Figure 6-4c demonstrates Raman spectra of P(VP−AA) monocomponent solutions measured in the HC−MOW presented in Figure 6-1b. A full table of peak assignments for P(VP−AA) is provided in Table S2. Looking for the most prominent peaks, for P(VP−AA) the ones at 938 cm^{-1} are chosen.
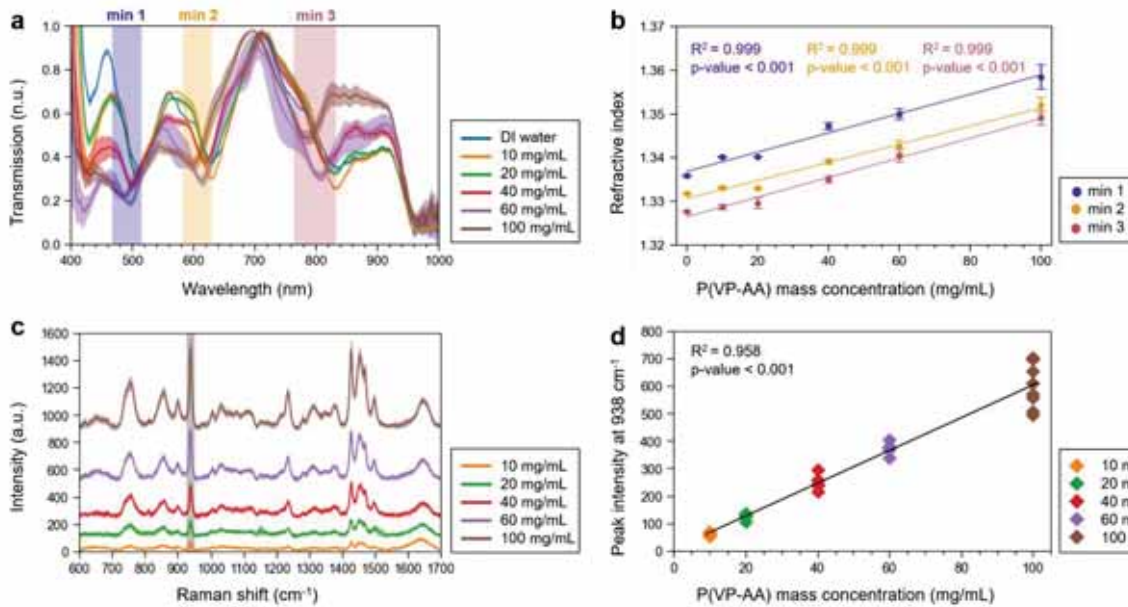
*Figure 6-4. P(VP−AA) monocomponent solution RI and Raman spectroscopy measurements. (**a**) Transmission spectra of HC−MOW with P(VP−AA) aqueous solutions with concentrations of 10, 20, 40, 60 and 100 mg/mL compared to DI water demonstrate 3 spectral regions with anti-resonant minima positions (min 1, min 2, min 3), that can be used to extract RI values. (**b**) Linear dependence of the corresponding RI values of P(VP−AA) aqueous solutions extracted from the 3 anti-resonant minima positions on the P(VP−AA) mass concentration. (**c**) Raman spectra of HC−MOW with P(VP−AA) aqueous solutions with concentrations of 10, 20, 40, 60 and 100 mg/mL provide a set of characteristic Raman peak Raman peaks assignment for P(VP−AA) monocomponent solution is presented in Table S2. (**d**) Linear dependence of the corresponding Raman peak intensities at 938 cm^{-1} Raman shift of P(VP−AA) aqueous solutions on the P(VP−AA) mass concentration. Linear dependences at the peak intensities of 1234 cm^{-1} and 1428 cm^{-1} are presented in Figure S3. Reproduced from [2]*

(C−C ring breathing mode and C−C stretch), 1234 cm^{-1} (corresponds to C−C stretch, C−H bending in acrylic acid unit) and 1428 cm^{-1} (corresponds to pyrrolidone ring (CH$_2$ scissor)).[205–208] The dependence of the peak intensity at 938 cm^{-1} on the P(VP−AA) concentration and its linear approximation is demonstrated in Figure 6-4d. For the line fitting, R^2 is 0.958 and $p-value$ is less than 0.001, so the Raman peak intensity linearly depends on concentration, similarly to RI dependence on concentration and to dependencies obtained for BSA.

Therefore, the next step of the research is two−in−one characterization of multicomponent colloid systems of BSA and P(VP−AA), highlighting the ability to extract RI values in a set of spectral regions and observe characteristic Raman peaks of each compound. RI values and considered Raman peaks have linear dependence on component concentration. Next, the capabilities of two−in−one characterization for resulting BSA@P(VP−AA) nano−sized complexes and corresponding micron−sized MB are evaluated.

6.3. BSA@P(VP-AA) structures

6.3.1. Characterization

The synthesis route of BSA@P(VP−AA) complexes and MB is presented in Figure 6-5a and similar to our previous report[177]. Briefly, initial compounds are dissolved in aqueous solution with desired protein: copolymer ratios of 3:1, 5:1, and 10:1 and at the total mass concentration of 50 mg/mL to produce complexes (BSA@P(VP−AA) [3:1], BSA@P(VP−AA) [5:1], and BSA@P(VP−AA) [10:1], respectively). Next, each complex solution with protein: copolymer mass ratios of 3:1, 5:1, and 10:1, that equals to molar ratios 1:1.5, 1:1, 2.3^1 is sonicated to produce MB (labeled as [3:1] MB, [5:1] MB, and [10:1] MB, respectively). Figure 6-5b highlights that the surface tension values of BSA@P(VP−AA) [3:1] aqueous solution are lower than BSA aqueous solution at the same total mass concentration, that promotes stable MB synthesis[209]. The mass concentration of 50 mg/mL is the most preferred one for stable BSA or HAS based MB synthesis[210].
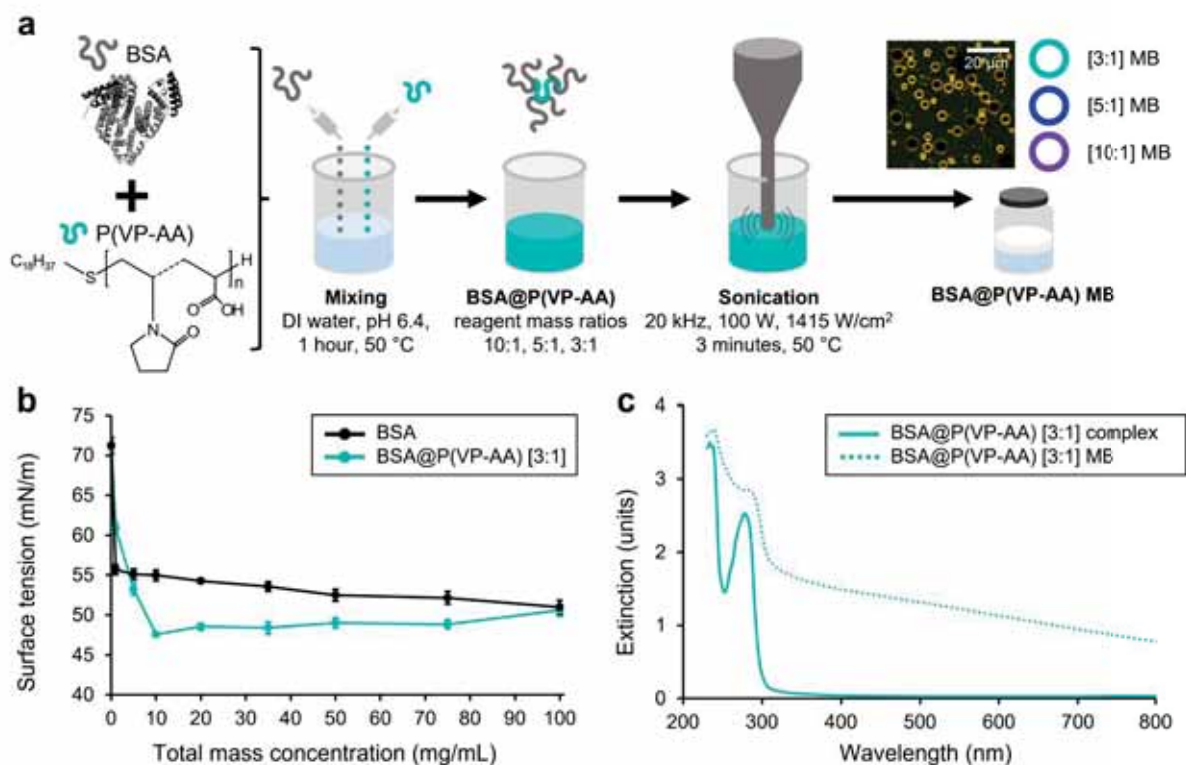
Figure 6-5. Synthesis and characterization of BSA@P(VP−AA) complexes and microbubbles. (a) Intact compounds (BSA and P(VP−AA)) are mixed initially with the protein: copolymer mass ratios of 3:1, 5:1, and 10:1, mixed at 50 °C for an hour to produce BSA@P(VP−AA) complexes with corresponding ratios. After that, aqueous solutions of complexes are sonicated to produce BSA@P(VP−AA) MB. Inlet confocal microscopy image of [3:1] MB is adapted from Estifeeva et al.[60] (b) Surface tension of BSA@P(VP−AA) [3:1] complexes compared to monocomponent BSA solution measured as a function of the total mass concentration of components in the aqueous solution. Values for [5:1] and [10:1] complexes are presented in Figure S3. (c) Extinction spectra of BSA@P(VP−AA) complexes and corresponding MB synthesized at the protein: copolymer ratio of 3:1. Reproduced from [2]

Therefore, all complexes and MB used in the present work are produced at the total mass concentration of 50 mg/mL as the optimal concentration for MB synthesis.

After the synthesis, [3:1] MB demonstrated a higher mean diameter of 4.7 μm, compared to moderate values of 3.2 μm for [5:1] MB and 3.0 μm for [10:1] MB. The MB concentration is ranging from $(2.0 \pm 0.5) \times 10^8$ MB/mL for [3:1] MB to $(1.0 \pm 0.4) \times 10^{10}$

MB/mL for [10:1] MB. Observed trends are consistent with the previous report of our group[177].

6.3.2. Two-in-one sensing

Figure 6-5c demonstrates the extinction spectra of BSA@P(VP−AA) [3:1] complex and corresponding [3:1] MB produced with the total mass concentration of 50 mg/mL and highlights the absence of absorbance for the complex in the visible wavelength range. In contrast, a significant light scattering is observed for air−filled MB in the same spectral range, that can be analyzed by the Lorenz−Mie theory[211]. However, both spectra demonstrate that the BSA characteristic peak at 280 nm, confirming the presence of BSA in both systems[212,213]. Similar observations can be found for all produced complexes and MB with protein: copolymer ratios of [3:1], [5:1] and [10:1] at sets of different total mass concentrations, as presented in Figure 6-6.

Raman spectra of the obtained BSA@P(VP−AA) complexes and corresponding MB are presented in Figure 6-7. In Figure 6-7a, high concentrations are evaluated: 91 mg/mL for P(VP−AA) monocomponent solution, 250 mg/mL for BSA monocomponent solution, and 273 mg/mL: 91 mg/mL for BSA@P(VP−AA) [3:1] complex, respectively. Therefore, clear Raman peak designation is observed, and Raman fingerprint of BSA@P(VP−AA) in a 3:1 complex represents peaks from both BSA and P(VP−AA). In Figure 6-7b, all BSA@P(VP−AA) complexes and MB have total mass concentration of 50 mg/mL, leading to lower Raman signal intensities compared to Figure 6-7a, and reduced signal−to−noise ratios. Furthermore, in all BSA@P(VP−AA) complexes and MB with total mass concentration of 50 mg/mL, a bright peak of phenylalanine in BSA at 1004 cm^{-1} can be clearly found, meanwhile the mentioned P(VP−AA) peaks at 938, 1234, 1428 cm^{-1} possess reduced intensity. For peaks at 938 and 1428 cm^{-1}, related to pyrrolidone ring, this could be explained by steric complementarity and additional van der Waals bonds between P(VP−AA) and BSA[214]. It is worth noting that such P(VP−AA) peak intensity decrease
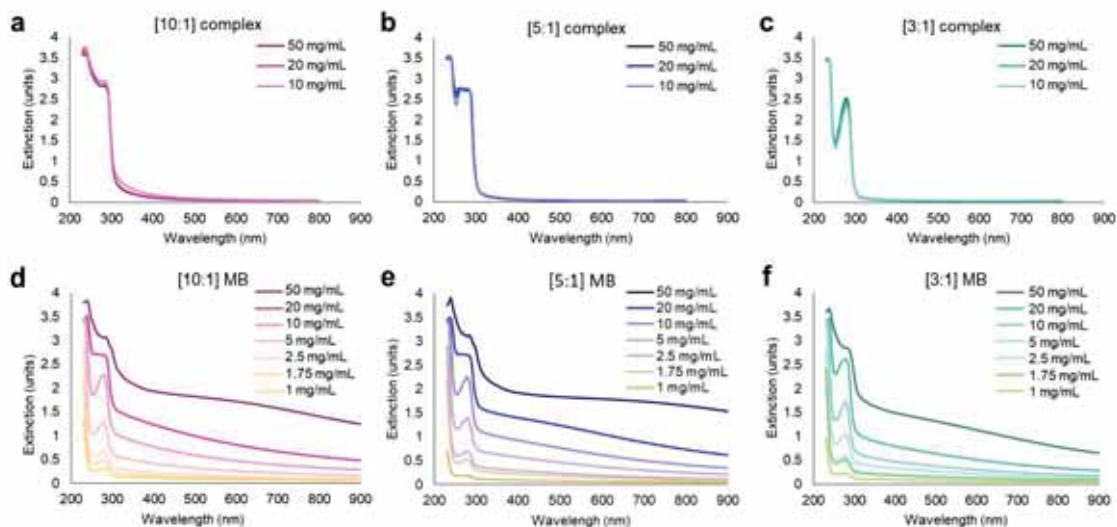
Figure 6-6. Extinction spectra for BSA@P(VP−AA) complexes and corresponding BSA@P(VP−AA) MB at sets of total mass concentrations. (a) BSA@P(VP−AA) [10:1] complex, (b) BSA@P(VP−AA) [5:1] complex, (c) BSA@P(VP−AA) [3:1] complex. All complex aqueous solutions are measured at a set of total component mass concentrations of 50, 20 and 10 mg/mL derived from the intact complex solution. (d) BSA@P(VP−AA) [10:1] MB, (e) BSA@P(VP−AA) [5:1] MB, (f) BSA@P(VP−AA) [3:1] MB. All complex aqueous solutions are measured at a set of total component mass concentrations of 50, 20, 10, 5, 2.5, 1.75 and 1 mg/mL from the intact MB solution. <mark>Reproduced from [26].</mark>

is observed mainly at low concentrations, that may indirectly indicate about less BSA and P(VP−AA) interaction at high concentrations. As for the Raman peak at 1234 cm^{-1} (related to C−H bending in acrylic acid unit), electrostatic interaction between BSA and P(VP−AA) takes place and hence influences the amplitude. Therefore, the preserved pattern of BSA and P(VP−AA) components in Raman sensing can assist in distinguishing between complex and monocomponent solutions, while the Raman fingerprint of the protein−copolymer complex can provide information on the nature and the intensity of interactions between BSA and P(VP−AA) that promote complex formation.
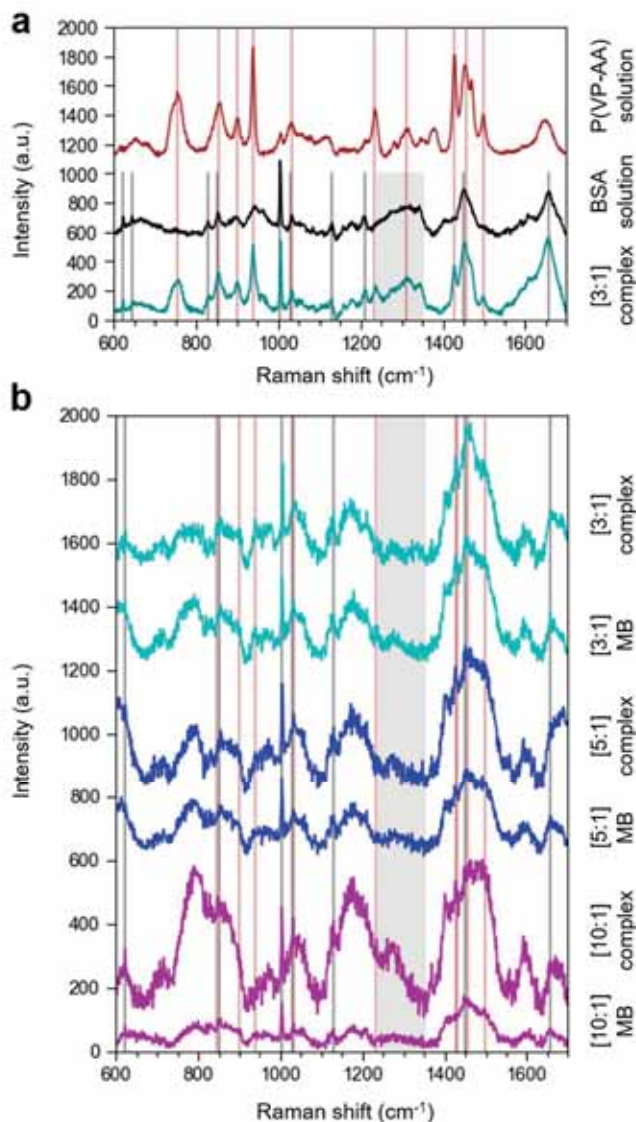
*Figure 6-7. Raman spectra of BSA@P(VP−AA) complexes and MB. (**a**) Measurements are made at high concentrations of PVP (91 mg/mL, brown line) and BSA (250 mg/mL, black line) monocomponent solutions, and BSA@P(VP−AA) [3:1] complex (with BSA and P(VP−AA) concentrations of 273 mg/mL and 91 mg/mL, respectively, represents the cyan line). (**b**) Measurements are made at the total mass concentration of 50 mg/mL for BSA@P(VP−AA) complexes and corresponding MB with the ratio of [3:1] (cyan lines), [5:1] (blue lines), and [10:1] (purple lines), respectively. Reproduced from [2]*

RI sensing of BSA@P(VP−AA) complexes and MB is demonstrated in Figure 6-8. As shown in Figure 6-8a, complexes synthesized with different protein: copolymer ratios

provide linear dependence of the RI on the total mass concentration (R^2 values greater than 0.977) and *p−values* lower than 0.01. Meanwhile, for MB in Figure 6-8b, only [3:1] MB can provide linear dependence of RI on the total mass concentrations, [5:1] MB can be measured at the total mass concentrations up to 10 mg/mL, while [10:1] MB are able for RI measurements only on concentrations as low as 1.75 mg/mL. For [3:1] MB, the total mass concentration of 50 mg/mL corresponds to the MB concentration of 2.0×10^8 MB/mL. For [5:1] MB, the total mass concentration of 10 mg/mL corresponds to the MB concentration of 4.0×10^8 MB/mL, while higher concentrations (up to 2.0×10^9 MB/mL as total mass concentration of 50 mg/mL) cannot be measured. Similar trend is well pronounced for [10:1] MB sample, where the total mass concentration of 50 mg/mL corresponds to $(1.0 \pm 0.4) \times 10^{10}$ MB/mL. With a components total mass concentration 2.5 mg/mL and higher (corresponds to 5.0×10^8 MB/mL), quasi−sinusoidal pattern with minima in transmission spectrum for [10:1] MB doesn't exist, as illustrated in Figure 6-9, that leads to impossibility to extract RI values according to Equation (6-1). Hence, [3:1] MB could be measured at total mass concentrations of 1.75 mg/mL (that corresponds to the MB concentration of 4.0×10^8 MB/mL) and lower, where the required periodical pattern is preserved. As RI determination requires extracting wavelength minima positions from a periodical transmission spectrum, the upper detection limit for MB samples is 4.0×10^8 MB/mL regardless of MB mean diameters. Therefore, while RI sensing of BSA@P(VP−AA) protein−copolymer complexes can be done with linear dependence of RI values on concentrations, RI sensing of corresponding BSA@P(VP−AA) MB is limited to the MB concentration of 4.0×10^8 MB/mL.
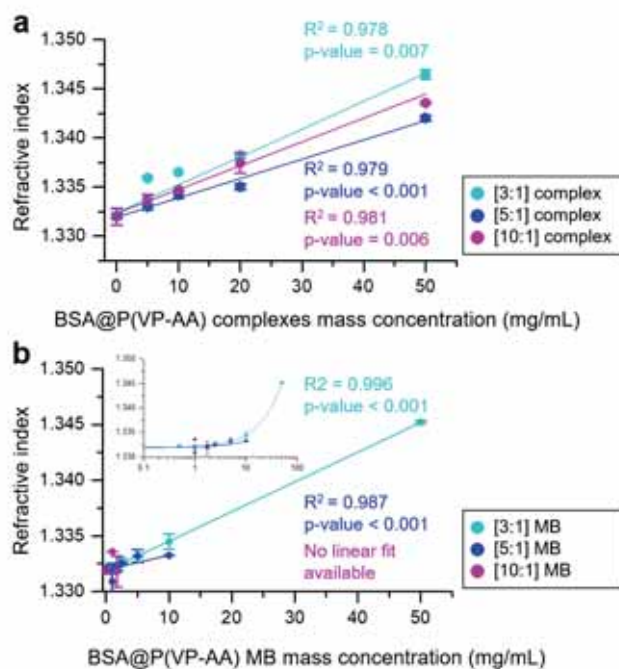
Figure 6-8. RI of BSA@P(VP−AA) complexes and corresponding MB. (a) complexes with the ratio of [3:1] (cyan lines), [5:1] (blue lines), and [10:1] (purple lines), respectively; (b) MB with the ratio of [3:1] (cyan lines), [5:1] (blue lines), and [10:1] (purple lines), respectively. The inset chart depicts the same plot in log scale to highlight values at low concentrations. <mark>*Reproduced from [26]*</mark>
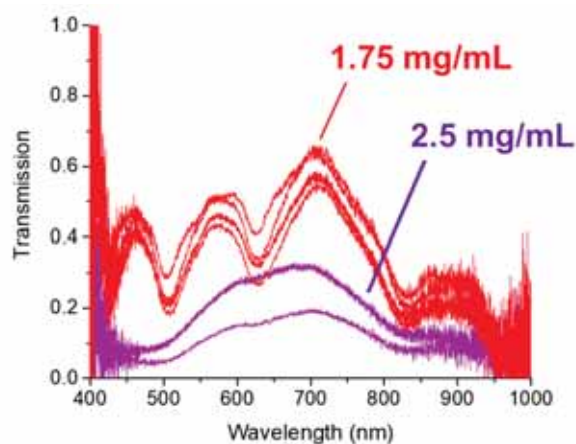
Figure 6-9. Transmission spectra of HC−MOW with BSA@P(VP−AA) [10:1] MB. Measurements are provided at the total mass concentration of 2.5 mg/mL (violet lines), and 1.75 mg/mL (red lines). <mark>Reproduced from [20]</mark>

6.4. Summary

A 2-in-1 measurement strategy was utilized to analyze a high molecular weight compound, specifically BSA protein. The study obtained data on the dependencies of Raman signal intensity and refractive index on concentration, revealing linear relationships between concentration and both parameters. The sensitivity of the method was up to $2.9 \cdot 10^8$ RIU·mL/mg for RI, while for Raman it was 6.4 mL/mg. Measurements were conducted in a range of 5 to 100 mg/mL, which includes the physiological values of albumin concentration in human plasma (35-50 mg/mL), making the method reliable for medical diagnostics.

The 2-in-1 measurement strategy was utilized to examine protein-copolymer nanosized conjugates at various concentrations and component ratios (1:1.5, 1:1, 2:1 protein:copolymer molar ratios). The effective RI and Raman scattering of the mixture at different component ratios were obtained.

For the first time, the ability to measure the transmission spectra of HC-MOW filled with aqueous microbubble (MB) solutions is demonstrated. The HC-MOW transmission spectra have a dependence on microbubble concentration, with a critical concentration of microbubbles at $4 \cdot 10^8$ MB/mL. Beyond this concentration, the periodicity of the HC-

MOW transmission spectrum deteriorates, which can be attributed to an augmented losses caused by light scattering on MB.

The obtained results demonstrated that HC-MOW is perspective for multifaceted 2-in-1 characterization of complex solutions.

Chapter 7. Perspectives of HC-MOW and Raman Spectroscopy Application for Isolation and Analysis of Extracellular vesicles

Next, the applicability of the present 2-in-1 sensor to extracellular vesicles (EV) was explored. But before proceeding to EV sensing, their isolation from cell culture medium or biological fluid is needed and therefore discussed. These results were published in:

a) [215] M.A. Slyusarenko, N.S. Nikiforova, E. I. Sidina, I.V. Nazarova, V.V. Egorov, Y.P. Garmay, A.A. Merdalimova, N.P. Yevlampieva, D.A. Gorin, A.V. Malek, Formation and evaluation of a two-phase polymer system in human plasma as a method for extracellular nanovesicle isolation. Polymers (Basel), 2021, 13(3):1–16. https://doi.org/10.3390/polym13030458 (IF=3.426, Q1)

Author's contribution: Raman spectroscopy, nanoparticle tracking analysis, writing a corresponding paragraph.

b) [216] V.Chernyshev, R.Chuprov-Netochin, E.Tsydenzhapova, E.Svirshchevskaya, R.Poltavtseva, A.Merdalimova, A.Yashchenok, A.Keshelava, K.Sorokin, V.Keshelava, G.Sukhikh, D.Gorin, S.Leonov, M.Skliar. Asymmetric depth-filtration: A versatile and scalable method forhigh-yield isolation of extracellular vesicles with low contamination. Journal of Extracellular Vesicles, 11, e12256. https://doi.org/10.1002/jev2.12256 (IF 17.3, Q1)

Author's contribution: Raman spectroscopy, writing a corresponding paragraph.

7.1. Isolation

7.1.1. Asymmetric Depth Filtration

A novel asymmetric depth filtration (DF) approach to isolate EV was developed by our lab research scientist V. Chernyshev and collaborators [216]. The present method

allows isolation from biological fluids that outperforms ultracentrifugation (that is a gold standatd for EV isolation) and size-exclusion chromatography in purity and yield of isolated EVs. By thesemetrics, a single-step DF matches or exceeds the performance of multistep protocols with dedicated purification procedures in the isolation of plasma EVs. The selective transit and capture of biological nanoparticles in asymmetric pores by size and elasticity, low surface binding to the filtration medium, and the ability to cleanse EVs held by the filter before their recovery with the reversed flow all contribute to the achieved purity and yield of preparations were demonstrated. Furthermore, the method's versatility by applying it to isolate EVs from different biofluids (plasma, urine, and cell culture growthmedium) was demonstrated. The DF workflow is simple, fast, and inexpensive. Only standard laboratory equipment is required for its implementation, making DF suitable for low-resource and point-of-use locations. The method may be used for EV isolation from small biological samples in diagnostic and treatment guidance applications. It can also be scaled up to harvest therapeutic EVs from large volumes of cell culture medium.

The asymmetric depth filtration features and protocol are demonstrated in Figure Figure 7-1 and elaborated in the paper[216]. Briefly, The developed method immobilizes EVs on the surface and within the depth of porous medium and then recovers them by reversing the carrier flow through the filter. In a single step, it isolates EVs from complex biological fluids, such as plasma, with high yield and purity. Characterization methods to prove the method performance are the following: nanoparticle tracking analysis to estimate EV concentration and size distribution; electronic microscopy to explore sizes and morphology; FACS (Fluorescence-activated Cell Sorting) to estimate expression of EV biomarkers (proteins); mass spectrometry and immunoblotting to compare concentration of EVs and lipid particles.
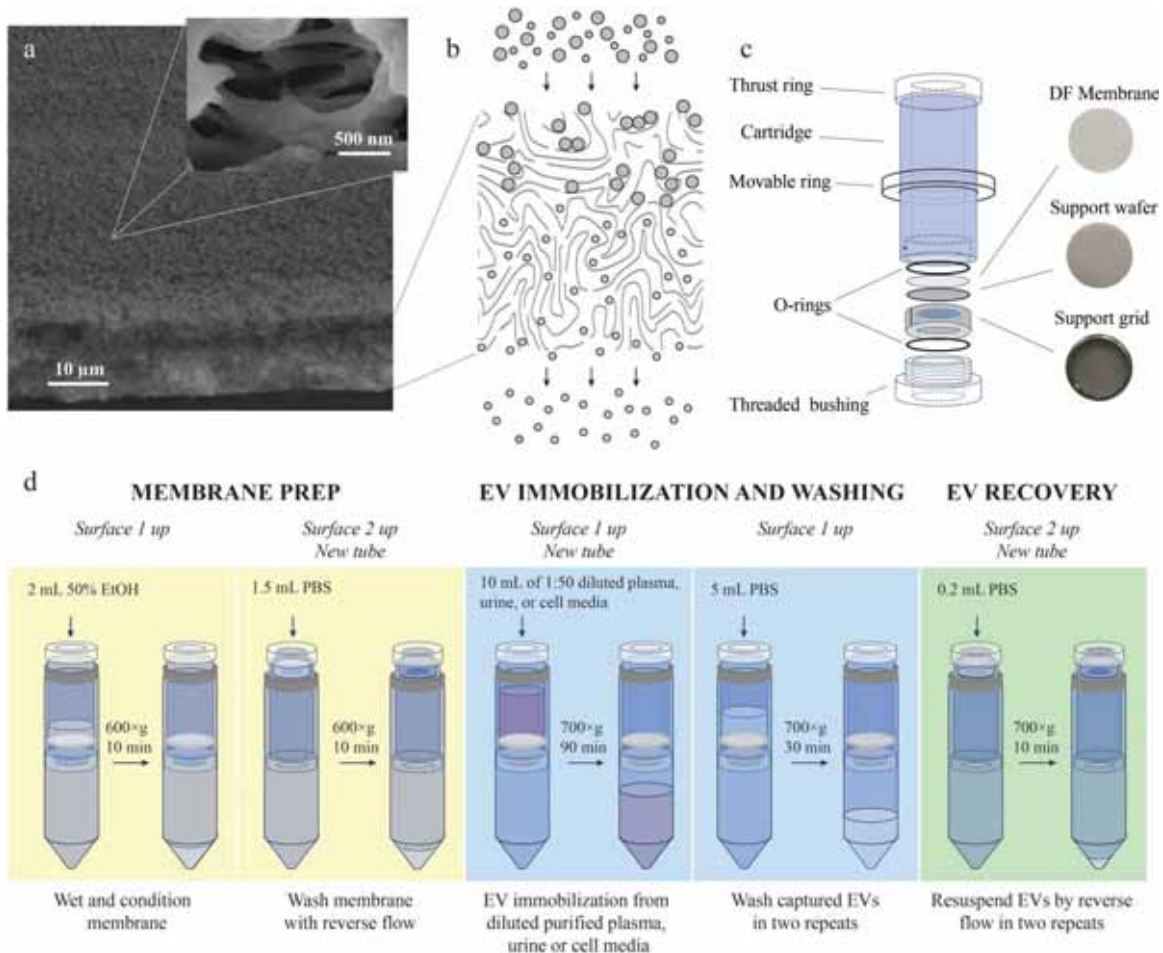
Figure 7-1. Depth-filtration medium, cartridge, and the protocol for DF isolation of EVs from blood plasma, urine, and cell culture media. (a) SEM image of the depth-filtration membrane showing its edge and the entrance surface (Surface 1). Higher magnification (inset) of inlet pores in Surface 1 shows apertures much larger than the size of EVs. As a result, the flow drags vesicles inside the pores until they become immobilized within the depth of the filter. (b) Illustration of the depth filtration process showing two populations of particles of different sizes. Larger particles are retained within the volume of the filtration medium, while smaller particles are eluted. (c) DF cartridge. Photographs of the membrane and its support (porous wafer and stainless-steel grid on which it rests) are shown on the right. (d) Summary of the depth-filtration workflow to isolate EVs from blood plasma, urine, and cell culture media. Reproduced from [216]

My part of work was to use in addition Raman spectroscopy to compare Raman spectra of proteins and EV. As EV in fact consist of lipids and proteins, their Raman spectra should be enriched compared to bulk protein.

The Raman analysis of plasma EVs was performed using a spectrometer (Horiba LabRam EvolutionHR,Horiba Ltd., Irvine, CA, USA) equipped with OlympusMPlan 50 × objective and 600 lines/mm grating. Raman scattering was excited by a 633-nm laser adjusted to 50% of its maximum power. A small drop (∼1 μl) of a plasma EV sample was pipetted on a fused quartz surface and dried at roomtemperature. The analyte concentration was increased by placing the second drop in the exact location and drying.
Three spectra were accumulated with a 50-s exposure and averaged. The Raman spectra of the clean area of quartz glass and the dried solution of human serum albumin (0.4 g/ml; Octapharma Pharmazeutika Produktionsgesellschaft m.b.H., Austria) were used as controls.

Raman spectrum of plasma EVs isolated by DF (Figure 7-2) agrees with previous reports [215,217] and contains the expected peaks identified in

Table 7-1. Specifically, the peak at 1004 cm–1 corresponds to aromatic ring stretching in Phenylalanine. The spectral region between 1200 and 1300 cm–1 corresponds to amide III bands, and the peak at 832 cm–1 is due to out-of-plane ring breathing in Tyrosine. The presence of cholesterol (peak near 704 cm–1) and lipids (peak at 1440 cm–1, corresponding to CH2 bending in lipids and cholesterol) reveals membrane constituents of EVs.
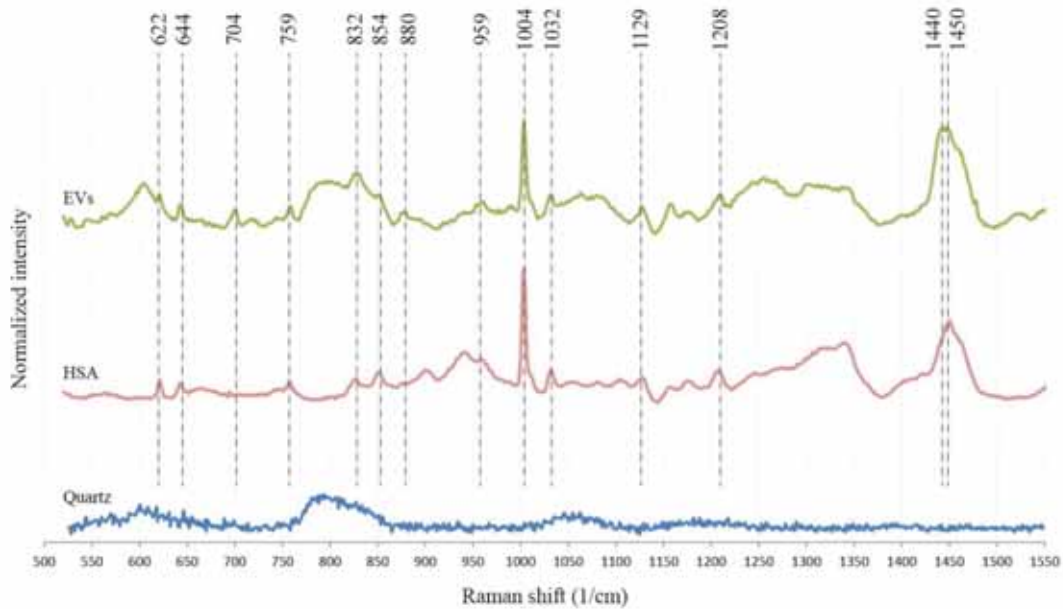
Figure 7-2. Raman spectrum of plasma EVs isolated by depth-filtration is compared with spectra of human serum albumin (HSA) and fused quartz substrate. Reproduced from [216]

Table 7-1. Raman peaks in EV spectra

Raman shift, cm^{-1}	Assumed assignment	Reference
622	Phenylalanine (phenyl ring breathing)	[184]
644	Tyrosine (C–C twisting)	[218]
704	Cholesterol and cholesterol esters	[219,220]
759	Tryptophan	[221]
832	Tyrosine (out of plane ring breathing)	[218,221]
854	Tyrosine (ring breathing mode); proline (C-C ring stretch)	[221]
880	Tryptophan; in-plane rocking (CH$_2$), e.g., protein	[218,222]
959	Cholesterol	[218,221]
1004	Phenylalanine, C-C aromatic ring stretching	[184,219]
1032	CH$_2$CH$_3$ bending (e.g., phospholipid); C-C vibration (e.g., polysaccharide)	[222]
1129	Lipids and proteins	[219]
1208	Phenylalanine, tryptophan (C-C$_6$H$_5$ stretching)	[221], [223]
1200-1300	Amide III in proteins	[219]
1440-1450	Lipids CH$_2$ deformation at 1437; lipids and proteins CH$_2$/CH$_3$ deformation at 1443; protein CH$_2$ bending mode at 1446	[218], [221], [222]

7.1.2. Two-phase polymer system

The optimized method of a two-phase polymer system in human plasma (PTPS) for EV isolation was developed by our colleagues in N.N. Petrov National Medical Research Center of Oncology and Oncosystem Ltd[215]. The aim of the study was to explore the

polyethylene glycol–dextran two-phase polymer system formed in human plasma to isolate the exosome-enriched fraction of plasma extracellular nanovesicles. The main steps of the isolation protocol are demonstrated in **Figure 7-3**.

Systematic analysis was performed to determine the optimal combination of the polymer mixture parameters (molecular mass and concentration) that resulted in phase separation. The separated phases were analyzed by nanoparticle tracking analysis and Raman spectroscopy, that were my part of work. Furthermore, the isolated vesicles were characterized by atomic force microscopy and dot blotting. In conclusion, the protein and microRNA contents of the isolated EV were assayed by flow cytometry and by reverse transcription followed by quantitative polymerase chain reaction (RT-qPCR), respectively. The presented results revealed the applicability of a new method for plasma ENV isolation and further analysis with a diagnostic purpose.
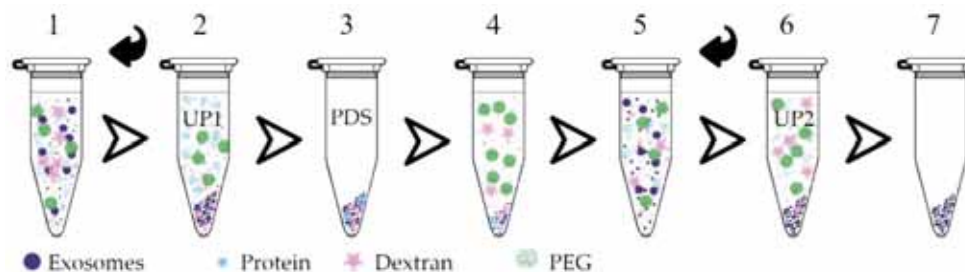
Figure 7-3. Steps of the PTPS-based extracellular nanovesicles isolation protocol. (1) A mixture of plasma and polymers (dextran/polyethylene glycol); (2) two phases formed after mixing and centrifugation; (3) the upper phase "UP1", containing PEG and proteins, is removed; (4) UP1 is replaced with a protein-depleting solution (PDS); (5) stirring; (6) the solution is again separated into two phases by centrifugation; (7) as a result, together with the formed upper phase "UP2", protein residues are removed, while the lower phase contains dextran and ENVs. Reproduced from Slyusarenko et al.[215]

Raman spectroscopy, that is my part, was applied to explore the chemical compositions of the phases by evaluation of their characteristic spectra. Figure 7-4 shows the Raman spectra of "pure" PTPS components: DEX, PEG, and UC-isolated ENVs dissolved in PBS and four phases of PTPS (UP1, LP1, UP2, and LP2). Characteristic peaks of "pure" PTPS components and their likely assignments reported previously are listed in
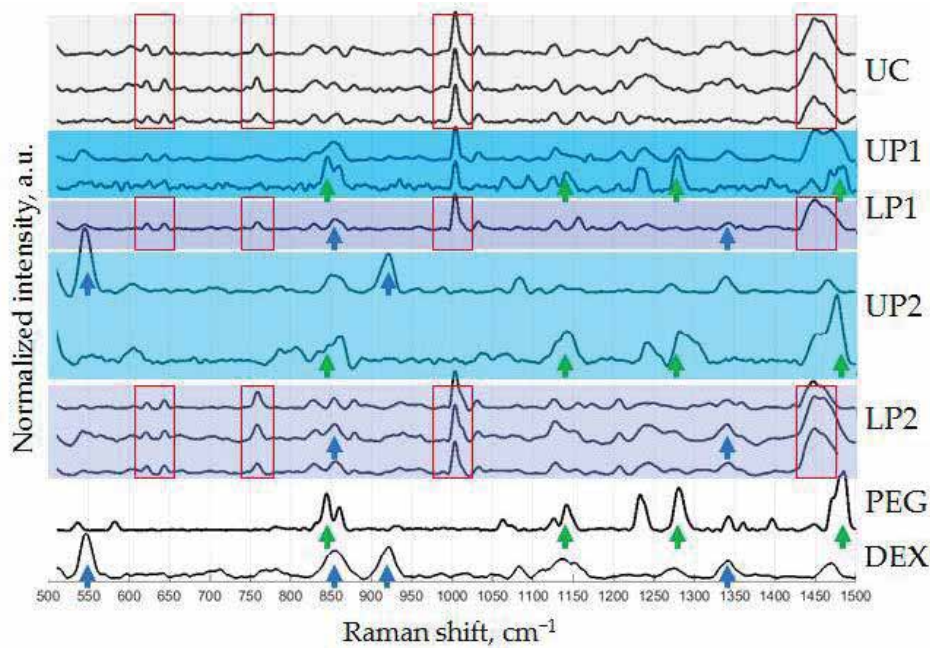
Figure 7-4. Raman spectra of PTPS phases and pure components. Measurements were repeated for samples that were supposed to be not homogeneous enough—these results are shown by multiple curves. Reproduced from [216]

For example, UC-EV-specific peak at 1004 cm^{-1} may reflect the presence of an essential -amino acid phenylalanine, however enrichment of this compound in plasma EV compared to total plasma was not detected. The composition of tested solution included various plasma components and was too complex for precise assigning. Without identifying specific peaks, it is important to note that several characteristic peaks can be observed in spectra of UC-ENV and they are repeated in spectra of lower phases after first (LP1) and second (LP2) separation (red frame). This observation can support the

phenomena of the concentration of the plasma vesicles into the dextran-formed lower phase of PTPS.

Raman spectra of pure DEX and PEG had also several characteristic peaks. As expected, the profiles of both the LP1 and LP2 phases had similarities to the DEX profile (marked by blue arrows), and these results were well reproducible. However, multiple analyses of the upper phases revealed different results, resembling either DEX or PEG profiles (marked by blue and green arrows). It became especially visible after the second phase separation. Two types of spectra, PEG-like with characteristic peaks shown by green arrows and DEX-like with characteristic peaks shown by blue arrows, were detected in UP2. To determine the nature of this observation, samples dried on the surface of quartz glass were visualized before Raman spectroscopy.

Table 7-2. Raman peaks in EV and polymers spectra

Sample	Raman shift, cm^{-1}	Likely assignment	Ref.
UC-ENV	622	Phenylalanine (phenyl ring breathing)	[184]
	644	Tyrosine (C–C twisting)	[218]
	758	Tryptophan	[218,221]
	1004	Phenylalanine (phenyl ring breathing)	[184]
	1208	Phenylalanine, tyrosine (C-C$_6$H$_5$ stretching)	
	1230, 1237-1241	Amide III bonds (rand coils and beta-sheet, respectively)	[223]
	1340	Tryptophan, lipids (CH$_2$ deformation)	[224–226]
	1360	Tryptophan (Fermi resonance doublet with 1340 cm^{-1})	[226]
	1449	Lipids and proteins (CH$_2$/CH$_3$ deformation)	[222,223,227]
PEG	844, 860	CH$_2$ rocking	[228,229]
	1141	CO stretch	
	1232	CH$_2$ twist	
	1281	CH$_2$ twist	
	1484	CH$_2$ bending	
Dextran	546	C3C4, C4C5 deformation	[230]
	855	C-1-H bending	[231]
	922	COH deformation	
	1342	CCH deformation, OCH deformation, CO vibration	

The dried UP2 phase revealed a bubble-like texture, as shown in Figure 7-5. Raman spectra taken inside of these "bubbles" showed a PEG-like profile, while spectra measured outside of "bubbles" were similar to DEX spectra. This result revealed the presence of both polymers in upper phases and their tendency to segregate within them. Incomplete

partitioning of the plasma two-phase polymer system during the applied procedure might influence the efficacy of plasma component separation.
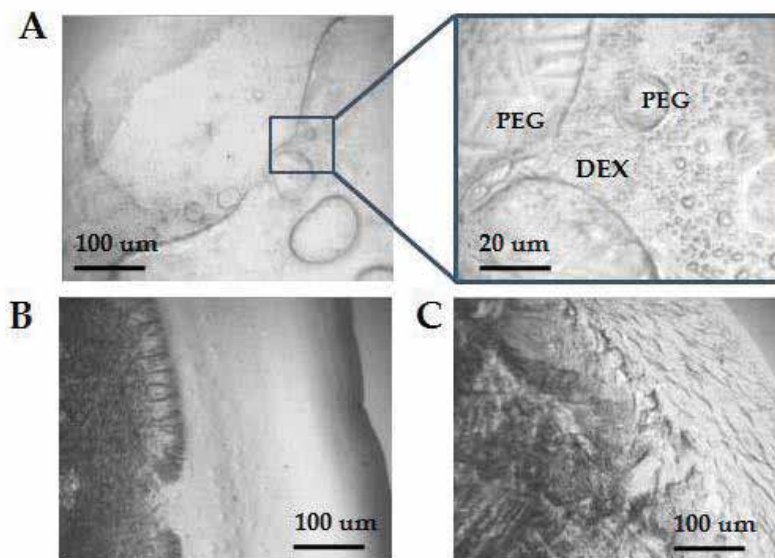
Figure 7-5. Area of dried drops of polymer mixtures and pure solutions visualized by light microscopy before Raman spectrometry. (A) Upper phase 2 UP2; (B) Dextran; (C) PEG.

Raman spectroscopy confirmed NTA results [215], namely the phenomena of phase separation in plasma solutions of PEG (20 kDa) 3.5% and DEX (450–650 kDa) 1.5%. Particles of exosomal size are concentrated in the lower phase, and their Raman spectra are similar to the spectra of UC-isolated plasma ENVs. Repeated phase separation did not considerably change the nanoparticle content (NTA) or chemical composition (RS) of the lower phase; however, it resulted in the appearance of nanoparticles of different sizes in the upper phase. It is interesting to note that the second round of phase separation resulted in an appearance of differently-sized particles in the upper phase (NTA, Figure 4B: UP2) and DEX-characteristic peaks 546 and 922 cm^{-1} (Figure 7-4: UP2) in its Raman spectra, and that both were not detected in UP1. However, the currently available data are not sufficient to explain this coincidence.

7.2. Two-in-one sensing of EV in HC-MOW

7.2.1. Characterization

The exosome-like fraction of EV was used, e.g. with size 50-200 nm, obtained from two cell lines: 22rv1 and skov3. To estimate their size distribution and concentration, nanoparticle tracking analysis (NTA) was used. The results are demonstrated in Figure 7-6: the median sizes are almost the same, but concentrations differ in one order: approximately 6×10^{11} 1/mL for 22rv1 and 6×10^{10} 1/mL for skov3, respectively.
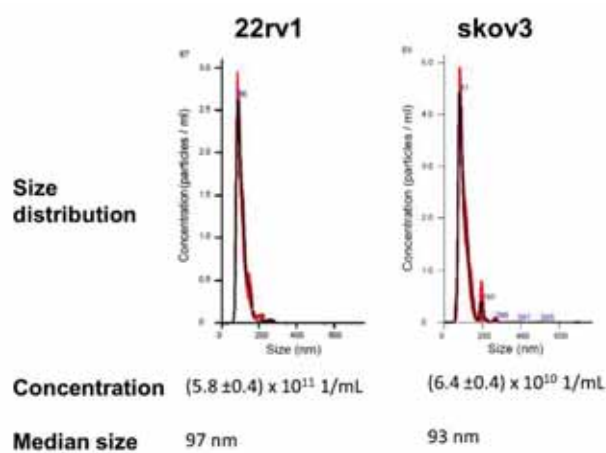
Figure 7-6. Characterization of extracellular vesicles (EV): size distribution and concentration.

7.2.2. Refractive index sensing

Similar to BSA, the transmission spectrum of exosomes 22rv1 and skov3 was measured in the waveguide. The results are shown in Figure **7-7**.
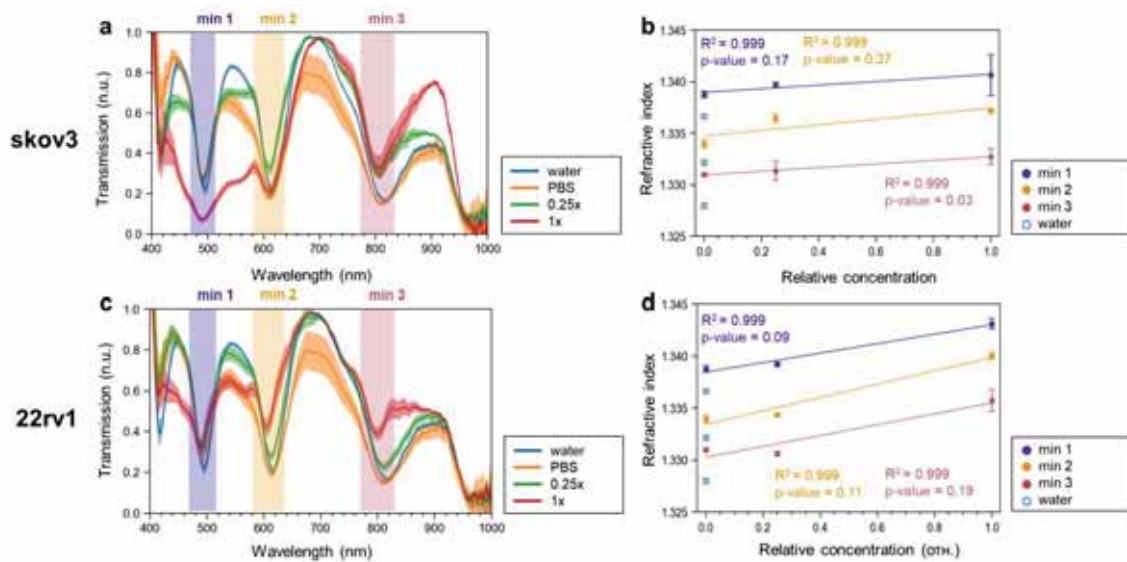
Figure 7-7. Measurement of the refractive index of EV in a waveguide. (a) Transmission spectra of skov3 vesicles; (b) Transmission spectrum versus relative concentration for skov3; (c) Transmission spectra of 22rv1 vesicles; (d) Transmission spectrum versus concentration for 22rv1. The concentrations used were: 0 = PBS; 0.25 = initial EV diluted by a factor of 4; 1 = initial EV concentration.

As the buffer for the exosomes is PBS and not water, the direct approximations were made through the points for PBS as the zero concentration of the exosomes. That is, in Figure 7-7b,d the points for water are not involved in the construction of the approximating straight line, and are shown only for comparison. On the plotted approximation lines it can be observed that R^2 is still close to unity, however the p-value in most cases does not pass the barrier of 0.05 (i.e. greater than it). However, instead of analysing three points (relative concentrations of 0, 0.25 and 1), only 2 points may be compared, PBS and exosomes at their original concentration, using the t-test and the mean and RMS values of the refractive index. The results are shown in Figure 7-8 - both exosomes used showed a statistically significant difference to PBS in their refractive index.
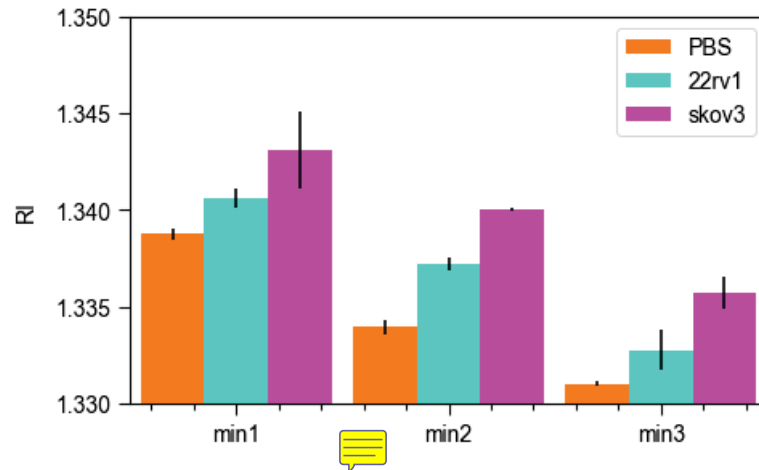
Figure 7-8. Comparison of the refractive index of EV and the control (PBS) for the initial EV concentrations.

7.2.3. Raman spectroscopy

Raman spectra of EV and controls, measured in HC-MOW, are demonstrated in Figure 7-9. Despite the long signal acquisition time (90 or 120 s), no significant EV spectra [216,219] (proteins and lipids, which are the main components of EV) were detected, and the observed Raman peaks belong to polypropylene [232], the material of the tube.
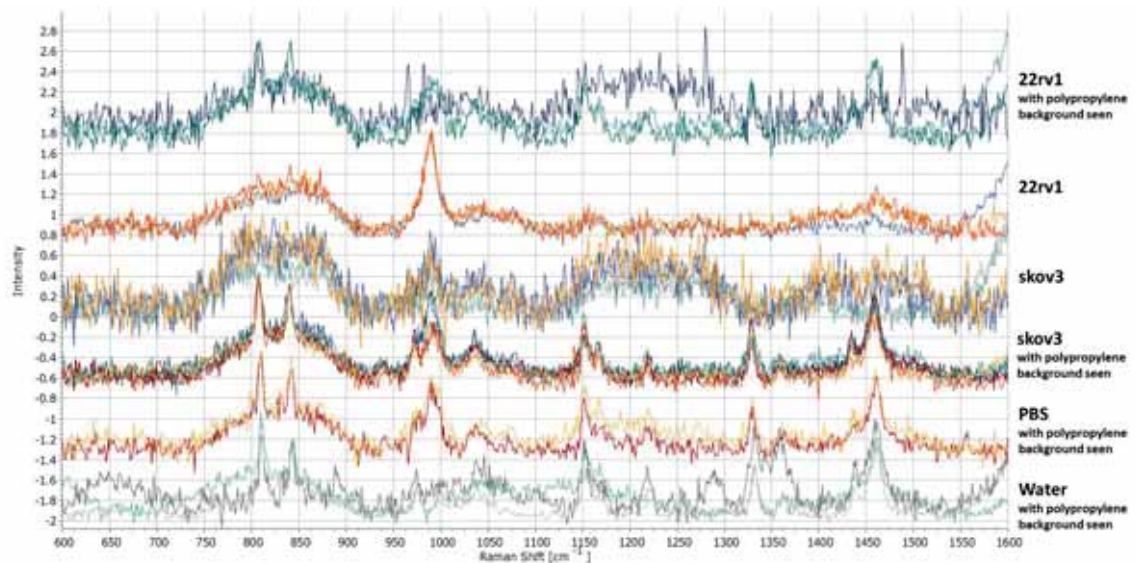
Figure 7-9. Raman spectra of EV and controls

7.3. Summary

It is shown that Raman spectroscopy can be used to demonstrate the process of phase separation of two high-molecular-weight components of the solution used for extracellular nanovesicle isolation. The LOD for the components of this solution, namely PEG and dextran, were estimated, that assisted to demonstrate the level of nanovesicle purification from them.

Raman spectroscopy of lipid and protein characteristic bands allowed to approve asymmetric depth filtration for extracellular vesicles isolation. Our findings are in good accordance with the Western blotting and mass spectrometric data.

At the concentrations of EV investigated, a statistically significant difference in refractive index from the control sample was detected. However, no characteristic Raman peaks were observed in the EV Raman scattering spectra, suggesting the need for higher concentrations or the use of Raman tags or plasmonic particles to enhance the Raman signal.

Thus, HC-MOW applicability for EV detection by refractive index was demonstrated, that makes HC-MOW perspective for medical diagnostics.

Chapter 8. Conclusion

The present work is aimed at developing sensors based on HC-MOW. Raman scattering, multi-wavelength refractive index (RI), and layer thickness are the physical properties that can be measured in HC-MOW and used for sensing.

It was shown that the use of a 2.5 cm long HC-MOW allows to increase the intensity of the observed Raman scattering in contrast to measuring a larger volume drop on a planar substrate. It was found that the enhancement factor for the low molecular weight compound (R6G was taken) is 50x, and for the high molecular weight compound (BSA) it is 2.3x. The difference in the enhancement factor between the high molecular weight and low

molecular weight compound is explained by the difference in the effective refractive index part.

A 2-in-1 measurement strategy was utilized to analyze a high molecular weight compound, specifically BSA protein. The study obtained data on the dependencies of Raman signal intensity and refractive index on concentration, revealing linear relationships between concentration and both parameters. The sensitivity of the method was up to $2.9 \cdot 10^8$ RIU·mL/mg for RI, while for Raman it was 6.4 mL/mg. Measurements were conducted in a range of 5 to 100 mg/mL, which includes the physiological values of albumin concentration in human plasma (35-50 mg/mL), making the method reliable for medical diagnostics.

The 2-in-1 measurement strategy was utilized to examine protein-copolymer nanosized conjugates at various concentrations and component ratios (1:1.5, 1:1, 2.3:1 protein:copolymer molar ratios). The effective RI and Raman scattering of the mixture at different component ratios were obtained.

For the first time, the ability to measure the transmission spectra of HC-MOW filled with aqueous microbubble (MB) solutions was demonstrated. The HC-MOW transmission spectra have a dependence on microbubble concentration, with a critical concentration of microbubbles at $4 \cdot 10^8$ MB/mL. Beyond this concentration, the periodicity of the HC-MOW transmission spectrum deteriorates, which can be attributed to an augmented losses caused by light scattering on MB.

It was shown that Raman spectroscopy can be used to demonstrate the process of phase separation of two high-molecular-weight components of the solution used for extracellular nanovesicle isolation. The LOD for the components of this solution, namely PEG and dextran, were estimated, that assisted to demonstrate the level of nanovesicle purification from them.

Raman spectroscopy of lipid and protein characteristic bands allowed to approve asymmetric depth filtration for extracellular vesicles isolation. Our findings are in good accordance with the Western blotting and mass spectrometric data.

111

The developed sensing methods show promise for real-time detection of small quantities of biological markers, making them valuable for rapid diagnostics.

Bibliography

1. Nazarenko, I. Extracellular Vesicles: Recent Developments in Technology and Perspectives for Cancer Liquid Biopsy. **2020**, doi:10.1007/978-3-030-26439-0_17.
2. Li, G.; Tang, W.; Yang, F. Cancer Liquid Biopsy Using Integrated Microfluidic Exosome Analysis Platforms. *Biotechnol. J.* **2020**, *1900225*, 1–10, doi:10.1002/biot.201900225.
3. Tenchov, R.; Sasso, J.M.; Wang, X.; Liaw, W.-S.; Chen, C.-A.; Zhou, Q.A. Exosomes─Nature's Lipid Nanoparticles, a Rising Star in Drug Delivery and Diagnostics. *ACS Nano* **2022**, *16*, 17802–17846, doi:10.1021/acsnano.2c08774.
4. Rondelli, V.; Helmy, S.; Passignani, G.; Parisse, P.; Di Silvestre, D. Integrated Strategies for a Holistic View of Extracellular Vesicles. *ACS Omega* **2022**, *7*, 19058–19069, doi:10.1021/acsomega.2c01003.
5. Kalluri, R.; LeBleu, V.S. The Biology, Function, and Biomedical Applications of Exosomes. *Science* **2020**, *367*, doi:10.1126/science.aau6977.
6. Tai, Y.L.; Chen, K.C.; Hsieh, J.T.; Shen, T.L. Exosomes in Cancer Development and Clinical Applications. *Cancer Sci.* **2018**, *109*, 2364–2374, doi:10.1111/cas.13697.
7. He, M.; Zeng, Y. Microfluidic Exosome Analysis toward Liquid Biopsy for Cancer. *J. Lab. Autom.* **2016**, *21*, 599–608, doi:10.1177/2211068216651035.
8. Lucchetti, D.; Fattorossi, A.; Sgambato, A. Extracellular Vesicles in Oncology: Progress and Pitfalls in the Methods of Isolation and Analysis. *Biotechnol. J.* **2018**, *14*, doi:10.1002/biot.201700716.
9. Rupert, D.L.M.; Claudio, V.; Lässer, C.; Bally, M. Methods for the Physical Characterization and Quantification of Extracellular Vesicles in Biological Samples. *Biochim. Biophys. Acta BBA - Gen. Subj.* **2017**, *1861*, 3164–3179, doi:10.1016/j.bbagen.2016.07.028.
10. Perevoschikov, S.; Kaydanov, N.; Ermatov, T.; Bibikova, O.; Usenov, I.; Sakharova, T.; Bocharnikov, A.; Skibina, J.; Artyushenko, V.; Gorin, D. Light Guidance up to 6.5 Mm in Borosilicate Soft Glass Hollow-Core Microstructured Optical Waveguides. *Opt. Express* **2020**, *28*, 27940, doi:10.1364/oe.399410.
11. Debord, B.; Amrani, F.; Vincetti, L.; Gérôme, F.; Benabid, F. Hollow-Core Fiber Technology: The Rising of "Gas Photonics." *Fibers* **2019**, *7*, doi:10.3390/FIB7020016.
12. Ding, W.; Wang, Y.Y.; Gao, S.F.; Wang, M.L.; Wang, P. Recent Progress in Low-Loss Hollow-Core Anti-Resonant Fibers and Their Applications. *IEEE J. Sel. Top. Quantum Electron.* **2020**, *26*, doi:10.1109/JSTQE.2019.2957445.
13. Zheltikov, A.M. Colors of Thin Films, Antiresonant Phenomena in Optical Systems, and the Limiting Loss of Modes in Hollow Optical Waveguides. *Uspekhi Fiz. Nauk* **2008**, *178*, 619–629, doi:10.3367/ufnr.0178.200806d.0619.

14. Ermatov, T.; Noskov, R.E.; Machnev, A.A.; Gnusov, I.; Atkin, V.; Lazareva, E.N.; German, S.V.; Kosolobov, S.S.; Zatsepin, T.S.; Sergeeva, O.V.; et al. Multispectral Sensing of Biological Liquids with Hollow-Core Microstructured Optical Fibres. *Light Sci. Appl.* **2020**, *9*, doi:10.1038/s41377-020-00410-8.

15. Bratashov, D.N.; Burmistrova, N.A.; Bondarenko, S.D.; Khlebtsov, B.N.; Atkin, V.S.; Shuvalov, A.A.; Zanishevskaya, A.A.; Skibina, Y.S.; Goryacheva, I.Y. Microstructured Waveguides with Polyelectrolyte-Stabilized Gold Nanostars for SERS Sensing of Dissolved Analytes. *Materials* **2018**, *11*, doi:10.3390/ma11050734.

16. Yan, D.; Popp, J.; Pletz, M.W.; Frosch, T. Highly Sensitive Broadband Raman Sensing of Antibiotics in Step-Index Hollow-Core Photonic Crystal Fibers. *ACS Photonics* **2017**, *4*, 138–145, doi:10.1021/acsphotonics.6b00688.

17. Ding, H.; Hu, D.J.J.; Yu, X.; Liu, X.; Zhu, Y.; Wang, G. Review on All-Fiber Online Raman Sensor with Hollow Core Microstructured Optical Fiber. *Photonics* **2022**, *9*, doi:10.3390/photonics9030134.

18. Markin, A.V.; Markina, N.E.; Goryacheva, I.Y. Raman Spectroscopy Based Analysis inside Photonic-Crystal Fibers. *TrAC - Trends Anal. Chem.* **2017**, *88*, 185–197, doi:10.1016/j.trac.2017.01.003.

19. Mu, Y.; Liu, M.; Li, J.; Zhang, X. Plasmonic Hollow Fibers with Distributed Inner-Wall Hotspots for Direct SERS Detection of Flowing Liquids. *Opt. Lett.* **2021**, *46*, 1369, doi:10.1364/ol.415733.

20. Khetani, A.; Momenpour, A.; Alarcon, E.I.; Anis, H. Hollow Core Photonic Crystal Fiber for Monitoring Leukemia Cells Using Surface Enhanced Raman Scattering (SERS). *Biomed. Opt. Express* **2015**, *6*, 4599, doi:10.1364/BOE.6.004599.

21. Ni, W.; Yang, C.; Luo, Y.; Xia, R.; Lu, P.; Hu, D.J.J.; Danto, S.; Shum, P.P.; Wei, L. Recent Advancement of Anti-Resonant Hollow-Core Fibers for Sensing Applications. *Photonics* **2021**, *8*, doi:10.3390/photonics8040128.

22. Bufetov, I.A.; Kosolapov, A.F.; Pryamikov, A.D.; Gladyshev, A.V.; Kolyadin, A.N.; Krylov, A.A.; Yatsenko, Y.P.; Biryukov, A.S. Hollow-Core Revolver Fibers (Properties, Design and Fabrication, Applications). *Photonics Russ.* **2019**, *13*, 426–443, doi:10.22184/FRos.2019.13.5.426.443.

23. Zanishevskaya, A.A.; Malinin, A.V.; Tuchin, V.V.; Skibina, Y.S.; Silokhin, I.Y. Photonic Crystal Waveguide Biosensor. *J. Innov. Opt. Health Sci.* **2013**, *6*, 1–6, doi:10.1142/S1793545813500089.

24. Liu, Z.; Zhang, W.; Zhang, X.; Wang, S.; Xia, Z.; Guo, X.; Zhao, Y.; Wang, P.; Wang, X.H. Microstructured Optical Fiber-Enhanced Light-Matter Interaction Enables Highly Sensitive Exosome-Based Liquid Biopsy of Breast Cancer. *Anal. Chem.* **2023**, *95*, 1095–1105, doi:10.1021/acs.analchem.2c03794.

25. Merdalimova, A.A.; Rudakovskaya, P.G.; Ermatov, T.I.; Smirnov, A.S.; Kosolobov, S.S.; Skibina, J.S.; Demina, P.A.; Khlebtsov, B.N.; Yashchenok, A.M.; Gorin, D.A. SERS Platform Based on Hollow-Core Microstructured Optical Fiber: Technology of UV-Mediated Gold Nanoparticle Growth. *Biosensors* **2022**, *12*, doi:10.3390/bios12010019.

26. Merdalimova, A.; Barmin, R.; Vorobev, V.; Terentyeva, D.; German, S.; Chernyshev, V.; Maslov, O.; Skibina, Y. Two − in − One Sensor of Refractive Index and Raman Scattering Using Hollow − Core Microstructured Optical Fibers for Colloid Characterization. 1–32.

27. Merdalimova, Anastasiia A. Vorobev, V.; Aleksandrov, A.; Barmin, R.; Terentyeva, D.; Estifeeva, T.M.; German, S.; Chernyshev, V.; Maslov, O.; Skibina, Y.S.; Rudakovskaya, P.; et al. Two-in-One Sensor of Refractive Index and Raman Scattering Using Hollow−Core Microstructured Optical Fibers for Colloid Characterization. *Adv. Opt. Mater.* **2023**, *submitted*.

28. Lægsgaard, J.; Bjarklev, A.; Monro, T. Microstructured Optical Fibers. *Handb. Optoelectron. Second Ed. Concepts Devices Tech.* **2017**, *1*, 711–740, doi:10.1201/9781315157009.

29. Debord, B.; Amrani, F.; Vincetti, L.; Gérôme, F.; Benabid, F. Hollow-Core Fiber Technology: The Rising of "Gas Photonics." *Fibers* **2019**, *7*, doi:10.3390/FIB7020016.

30. Skibina, J.S.; Iliew, R.; Bethge, J.; Bock, M.; Fischer, D.; Beloglasov, V.I.; Wedell, R.; Steinmeyer, G. A Chirped Photonic-Crystal Fibre. *Nat. Photonics* **2008**, *2*, 679–683, doi:10.1038/nphoton.2008.203.

31. Skibina, Y.S.; Tuchin, V.V.; Beloglazov, V.I.; Shteinmaeer, G.; Betge, I.L.; Wedell, R.; Langhoff, N. Photonic Crystal Fibres in Biomedical Investigations. *Quantum Electron.* **2011**, *41*, 284–301, doi:10.1070/qe2011v041n04abeh014536.

32. Russell, P.S.J. Photonic Crystal Fibers. *Science* **2003**, *299*, doi:10.1126/science.1079280.

33. Pryamikov, A.D.; Biriukov, A.S.; Kosolapov, A.F.; Plotnichenko, V.G.; Semjonov, S.L.; Dianov, E.M. Demonstration of a Waveguide Regime for a Silica Hollow - Core Microstructured Optical Fiber with a Negative Curvature of the Core Boundary in the Spectral Region > 35 Mm. *Opt. Express* **2011**, *19*, 1441, doi:10.1364/oe.19.001441.

34. Antonopoulos, G.; Benabid, F.; Birks, T.A.; Bird, D.M.; Knight, J.C.; St Russell, P.J.; Cregan, R.F.; Mangan, B.J.; Roberts, P.J.; Allan, D.C. Experimental Demonstration of the Frequency Shift of Bandgaps in Photonic Crystal Fibers Due to Refractive Index Scaling. *Opt. Express Vol 14 Issue 7 Pp 3000-3006* **2006**, *14*, 3000–3006, doi:10.1364/OE.14.003000.

35. Wang, Y.; Gao, R.; Xin, X. Hollow-Core Fiber Refractive Index Sensor with High Sensitivity and Large Dynamic Range Based on a Multiple Mode Transmission Mechanism. *Opt. Express* **2021**, *29*, 19703, doi:10.1364/oe.426705.

36. Merdalimova, A.; Vorobev, V.; Zanishevskaya, A.; Aleksandrov, A.; Rudakovskaya, P.; Skibina, Y.; Gorin, D. Hollow-Core Microstructured Optical Fibers and Their Applications for Biosensing. 1–48.

37. Fujiwara, E.; Cabral, T.D.; Sato, M.; Oku, H.; Cordeiro, C.M.B. Agarose-Based Structured Optical Fibre. *Sci. Rep.* **2020**, *10*, 1–8, doi:10.1038/s41598-020-64103-3.

38. van Putten, L.D.; Gorecki, J.; Numkam Fokoua, E.; Apostolopoulos, V.; Poletti, F. 3D-Printed Polymer Antiresonant Waveguides for Short-Reach Terahertz Applications. *Appl. Opt.* **2018**, *57*, 3953, doi:10.1364/ao.57.003953.

39. Yang, S.; Sheng, X.; Zhao, G.; Lou, S.; Guo, J. 3D Printed Effective Single-Mode Terahertz Antiresonant Hollow Core Fiber. *IEEE Access* **2021**, *9*, 29599–29608, doi:10.1109/ACCESS.2021.3059782.

40. Bertoncini, A.; Liberale, C. 3D Printed Waveguides Based on Photonic Crystal Fiber Designs for Complex Fiber-End Photonic Devices. *Optica* **2020**, *7*, 1487, doi:10.1364/OPTICA.397281.

41. Ebendorff-Heidepriem, H.; Schuppich, J.; Dowler, A.; Lima-Marques, L.; Monro, T.M. 3D-Printed Extrusion Dies: A Versatile Approach to Optical Material Processing. *Opt. Mater. Express* **2014**, *4*, 1494, doi:10.1364/OME.4.001494.

42. Cordeiro, C.M.B.; Ng, A.K.L.; Ebendorff-Heidepriem, H. Ultra-Simplified Single-Step Fabrication of Microstructured Optical Fiber. *Sci. Rep.* **2020**, *10*, 9678, doi:10.1038/s41598-020-66632-3.

43. Talataisong, W.; Ismaeel, R.; Sandoghchi, S.R.; Rutirawut, T.; Topley, G.; Beresna, M.; Brambilla, G. Novel Method for Manufacturing Optical Fiber: Extrusion and Drawing of Microstructured Polymer Optical Fibers from a 3D Printer. *Opt. Express* **2018**, *26*, 32007, doi:10.1364/oe.26.032007.

44. Skibina, Y.S.; Tuchin, V.V.; Beloglazov, V.I.; Shteinmaeer, G.; Betge, I.L.; Wedell, R.; Langhoff, N. Photonic Crystal Fibres in Biomedical Investigations. *Quantum Electron.* **2011**, *41*, 284–301, doi:10.1070/QE2011V041N04ABEH014536/XML.

45. Wu, S. *Ge 28 Sb 12 Se 60 Chalcogenide Glass Microstructured Optical Fiber: Fabrication and Application*; 2019;

46. Denisov, A.N.; Kosolapov, A.F.; Senatorov, A.K.; Pal'tsev, P.E.; Semjonov, S.L. Fabrication of Microstructured Optical Fibres by Drawing Preforms Sealed at Their Top End. *Quantum Electron.* **2016**, *46*, 1031–1039, doi:10.1070/QEL16212.

47. *Handbook of Optical Fibers*; Peng, G.-D., Ed.; Springer Singapore: Singapore, 2019; ISBN 978-981-10-7085-3.

48. Liu, Z.; Zhang, Z.F.; Tam, H.Y.; Tao, X. Multifunctional Smart Optical Fibers: Materials, Fabrication, and Sensing Applications. *Photonics* **2019**, *6*, doi:10.3390/photonics6020048.

49. Jasion, G.T.; Hayes, J.R.; Wheeler, N.V.; Chen, Y.; Bradley, T.D.; Richardson, D.J.; Poletti, F. Fabrication of Tubular Anti-Resonant Hollow Core Fibers: Modelling, Draw Dynamics and Process Optimization. *Opt. Express* **2019**, *27*, 20567, doi:10.1364/oe.27.020567.

50. Gattass, R.R.; Rhonehouse, D.; Gibson, D.; McClain, C.C.; Thapa, R.; Nguyen, V.Q.; Bayya, S.S.; Weiblen, R.J.; Menyuk, C.R.; Shaw, L.B.; et al. Infrared Glass-Based Negative-Curvature Anti-Resonant Fibers Fabricated through Extrusion. *Opt. Express* **2016**, *24*, 25697, doi:10.1364/oe.24.025697.

51. Chu, Y.; Dong, L.; Luo, Y.; Zhang, J.; Peng, G.-D. Additive Manufacturing of Optical Waveguides. In *Hybrid Planar - 3D Waveguiding Technologies*; D.

Fernandez, M., A. Ballesteros, J., Esteban, H., Belenguer, Á., Eds.; IntechOpen, 2023 ISBN 978-1-80356-149-3.

52. Luo, Y.; Canning, J.; Zhang, J.; Peng, G.D. Toward Optical Fibre Fabrication Using 3D Printing Technology. *Opt. Fiber Technol.* **2020**, *58*, doi:10.1016/j.yofte.2020.102299.

53. Yamamoto, J.; Yajima, T.; Kinoshita, Y.; Ishii, F.; Yoshida, M.; Hirooka, T.; Nakazawa, M. Fabrication of Multi Core Fiber by Using Slurry Casting Method. In Proceedings of the Optical Fiber Communication Conference; OSA: Los Angeles, California, 2017; p. Th1H.5.

54. Wu, Y.; Meneghetti, M.; Troles, J.; Adam, J.L. Chalcogenide Microstructured Optical Fibers for Mid-Infrared Supercontinuum Generation: Interest, Fabrication, and Applications. *Appl. Sci. Switz.* **2018**, *8*, doi:10.3390/app8091637.

55. Huheey, J.E.; Keiter, E.A.; Keiter, R.L. *Inorganic Chemistry: Principles of Structure and Reactivity*; 4th ed.; HarperCollins College Publishers: New York, NY, 1993; ISBN 978-0-06-042995-9.

56. Oxtoby, D.W.; Gillis, H.P.; Campion, A. *Principles of Modern Chemistry*; 7th ed.; Brooks/Cole Cengage Learning: Belmont, Calif, 2012; ISBN 978-0-8400-4931-5.

57. Ermatov, T.; Skibina, J.S.; Tuchin, V.V.; Gorin, D.A. Functionalized Microstructured Optical Fibers: Materials Methods Applications. *Materials* **2020**, *13*, doi:10.3390/ma13040921.

58. Li, J.; Ebendorff-Heidepriem, H.; Gibson, B.C.; Greentree, A.D.; Hutchinson, M.R.; Jia, P.; Kostecki, R.; Liu, G.; Orth, A.; Ploschner, M.; et al. Perspective: Biomedical Sensing and Imaging with Optical Fibers - Innovation through Convergence of Science Disciplines. *APL Photonics* **2018**, *3*, doi:10.1063/1.5040861.

59. Calcerrada, M.; García-Ruiz, C.; González-Herráez, M. Chemical and Biochemical Sensing Applications of Microstructured Optical Fiber-Based Systems. *Laser Photonics Rev.* **2015**, *9*, 604–627, doi:10.1002/lpor.201500045.

60. Schartner, E.P.; Tsiminis, G.; François, A.; Kostecki, R.; Warren-Smith, S.C.; Nguyen, L.V.; Heng, S.; Reynolds, T.; Klantsataya, E.; Rowland, K.J.; et al. Taming the Light in Microstructured Optical Fibers for Sensing. *Int. J. Appl. Glass Sci.* **2015**, *6*, 229–239, doi:10.1111/ijag.12128.

61. Ferreira, M.F.S.; Castro-Camus, E.; Ottaway, D.J.; López-Higuera, J.M.; Feng, X.; Jin, W.; Jeong, Y.; Picqué, N.; Tong, L.; Reinhard, B.M.; et al. Roadmap on Optical Sensors. *J. Opt. U. K.* **2017**, *19*, doi:10.1088/2040-8986/aa7419.

62. Candiani, A.; Cucinotta, A. Functionalized Microstructured Optical Fibers for Specific Nucleic Acid Detection. In *Optofluidics, Sensors and Actuators in Microstructured Optical Fibers*; Elsevier, 2015; pp. 229–246 ISBN 978-1-78242-329-4.

63. Caucheteur, C.; Guo, T.; Albert, J. Review of Plasmonic Fiber Optic Biochemical Sensors: Improving the Limit of Detection. *Anal. Bioanal. Chem.* **2015**, *407*, 3883–3897, doi:10.1007/s00216-014-8411-6.

64. Qin, M.; Hou, S.; Wang, L.; Feng, X.; Wang, R.; Yang, Y.; Wang, C.; Yu, L.; Shao, B.; Qiao, M. Two Methods for Glass Surface Modification and Their

Application in Protein Immobilization. *Colloids Surf. B Biointerfaces* **2007**, *60*, 243–249, doi:10.1016/j.colsurfb.2007.06.018.

65. Foo, H.T.C.; Ebendorff-Heidepriem, H.; Sumby, C.J.; Monro, T.M. Towards Microstructured Optical Fibre Sensors: Surface Analysis of Silanised Lead Silicate Glass. *J. Mater. Chem. C* **2013**, *1*, 6782, doi:10.1039/c3tc31414f.

66. Pujari, S.P.; Scheres, L.; Marcelis, A.T.M.; Zuilhof, H. Covalent Surface Modification of Oxide Surfaces. *Angew. Chem. Int. Ed.* **2014**, *53*, 6322–6356, doi:10.1002/anie.201306709.

67. Basabe-Desmonts, L.; Reinhoudt, D.N.; Crego-Calama, M. Design of Fluorescent Materials for Chemical Sensing. *Chem. Soc. Rev.* **2007**, *36*, 993, doi:10.1039/b609548h.

68. Müller, R.; Abke, J.; Schnell, E.; Macionczyk, F.; Gbureck, U.; Mehrl, R.; Ruszczak, Z.; Kujat, R.; Englert, C.; Nerlich, M.; et al. Surface Engineering of Stainless Steel Materials by Covalent Collagen Immobilization to Improve Implant Biocompatibility. *Biomaterials* **2005**, *26*, 6962–6972, doi:10.1016/j.biomaterials.2005.05.013.

69. Cordek, J.; Wang, X.; Tan, W. Direct Immobilization of Glutamate Dehydrogenase on Optical Fiber Probes for Ultrasensitive Glutamate Detection. *Anal. Chem.* **1999**, *71*, 1529–1533, doi:10.1021/ac980850l.

70. Tazawa, H.; Kanie, T.; Katayama, M. Fiber-Optic Coupler Based Refractive Index Sensor and Its Application to Biosensing. *Appl. Phys. Lett.* **2007**, *91*, 113901, doi:10.1063/1.2783278.

71. Howarter, J.A.; Youngblood, J.P. Optimization of Silica Silanization by 3-Aminopropyltriethoxysilane. *Langmuir* **2006**, *22*, 11142–11147, doi:10.1021/la061240g.

72. Fiorilli, S.; Rivolo, P.; Descrovi, E.; Ricciardi, C.; Pasquardini, L.; Lunelli, L.; Vanzetti, L.; Pederzolli, C.; Onida, B.; Garrone, E. Vapor-Phase Self-Assembled Monolayers of Aminosilane on Plasma-Activated Silicon Substrates. *J. Colloid Interface Sci.* **2008**, *321*, 235–241, doi:10.1016/j.jcis.2007.12.041.

73. Cras, J.J.; Rowe-Taitt, C.A.; Nivens, D.A.; Ligler, F.S. Comparison of Chemical Cleaning Methods of Glass in Preparation for Silanization. *Biosens. Bioelectron.* **1999**, *14*, 683–688, doi:10.1016/S0956-5663(99)00043-3.

74. Lowe, R.D.; Pellow, M.A.; Stack, T.D.P.; Chidsey, C.E.D. Deposition of Dense Siloxane Monolayers from Water and Trimethoxyorganosilane Vapor. *Langmuir* **2011**, *27*, 9928–9935, doi:10.1021/la201333y.

75. Decher, G.; Hong, J.D.; Schmitt, J. *Thin Solid Films, 210/21 I*; 1992; pp. 831–835;.

76. Ermatov, T.; Petrov, Y.V.; German, S.V.; Zanishevskaya, A.A.; Shuvalov, A.A.; Atkin, V.; Zakharevich, A.; Khlebtsov, B.N.; Skibina, J.S.; Ginzburg, P.; et al. Microstructured Optical Waveguide-Based Endoscopic Probe Coated with Silica Submicron Particles. *Materials* **2019**, *12*, doi:10.3390/ma12091424.

77. Noskov, R.E.; Zanishevskaya, A.A.; Shuvalov, A.A.; German, S.V.; Inozemtseva, O.A.; Kochergin, T.P.; Lazareva, E.N.; Tuchin, V.V.; Ginzburg, P.; Skibina, J.S.; et al. Enabling Magnetic Resonance Imaging of Hollow-Core Microstructured

Optical Fibers via Nanocomposite Coating. *Opt. Express* **2019**, *27*, 9868, doi:10.1364/oe.27.009868.

78. Lopez-Torres, D.; Elosua, C.; Villatoro, J.; Zubia, J.; Rothhardt, M.; Schuster, K.; Arregui, F.J. Photonic Crystal Fiber Interferometer Coated with a PAH/PAA Nanolayer as Humidity Sensor. *Sens. Actuators B Chem.* **2017**, *242*, 1065–1072, doi:10.1016/j.snb.2016.09.144.

79. Kostecki, R.; Ebendorff-Heidepriem, H.; Afshar V., S.; McAdam, G.; Davis, C.; Monro, T.M. Novel Polymer Functionalization Method for Exposed-Core Optical Fiber. *Opt. Mater. Express* **2014**, *4*, 1515, doi:10.1364/OME.4.001515.

80. Sciacca, B.; François, A.; Klingler-Hoffmann, M.; Brazzatti, J.; Penno, M.; Hoffmann, P.; Monro, T.M. Radiative-Surface Plasmon Resonance for the Detection of Apolipoprotein E in Medical Diagnostics Applications. *Nanomedicine Nanotechnol. Biol. Med.* **2013**, *9*, 550–557, doi:10.1016/j.nano.2012.10.007.

81. François, A.; Reynolds, T.; Monro, T. A Fiber-Tip Label-Free Biological Sensing Platform: A Practical Approach toward In-Vivo Sensing. *Sensors* **2015**, *15*, 1168–1181, doi:10.3390/s150101168.

82. Nguyen, L.V.; Warren-Smith, S.C.; Cooper, A.; Monro, T.M. Molecular Beacons Immobilized within Suspended Core Optical Fiber for Specific DNA Detection. *Opt. Express* **2012**, *20*, 29378, doi:10.1364/OE.20.029378.

83. Csaki, A.; Jahn, F.; Latka, I.; Henkel, T.; Malsch, D.; Schneider, T.; Schröder, K.; Schuster, K.; Schwuchow, A.; Spittel, R.; et al. Nanoparticle Layer Deposition for Plasmonic Tuning of Microstructured Optical Fibers. *Small* **2010**, *6*, 2584–2589, doi:10.1002/smll.201001071.

84. Younus, M.H.; Ali, G.Ghazi.; Salih, H.A. The Reinforced Optical Fiber Sensing with Bilayer AuNPs/SiC for Pressure Measurement: Characterization and Optimization. *J. Phys. Conf. Ser.* **2021**, *1795*, 012002, doi:10.1088/1742-6596/1795/1/012002.

85. Wu, J.; Li, Y.; Song, B.; Zhang, C.; Wang, Q.; Gao, X.; Huang, K. *Microstructured Optical Fiber Based on Surface Plasmon Resonance for Dual-Optofluidic-Channel Sensing*; In Review, 2022;

86. Arghir, I.; Delport, F.; Spasic, D.; Lammertyn, J. Smart Design of Fiber Optic Surfaces for Improved Plasmonic Biosensing. *New Biotechnol.* **2015**, *32*, 473–484, doi:10.1016/j.nbt.2015.03.012.

87. Kumar, S.; Singh, R.; Kaushik, B.K.; Chen, N.K.; Yang, Q.S.; Zhang, X. Lspr-Based Cholesterol Biosensor Using Hollow Core Fiber Structure. *IEEE Sens. J.* **2019**, *19*, 7399–7406, doi:10.1109/JSEN.2019.2916818.

88. Schroder, K.; Csaki, A.; Schwuchow, A.; Jahn, F.; Strelau, K.; Latka, I.; Henkel, T.; Malsch, D.; Schuster, K.; Weber, K.; et al. Functionalization of Microstructured Optical Fibers by Internal Nanoparticle Mono-Layers for Plasmonic Biosensor Applications. *IEEE Sens. J.* **2012**, *12*, 218–224, doi:10.1109/JSEN.2011.2144580.

89. Candiani, A.; Giannetti, S.; Sozzi, M.; Coscelli, E.; Poli, F.; Cucinotta, A.; Bertucci, A.; Corradini, R.; Konstantaki, M.; Margulis, W.; et al. Microstructured

Optical Fiber Bragg Grating Sensor for DNA Detection.; Gannot, I., Ed.; San Francisco, California, USA, March 20 2013; p. 85760E.

90. Bratashov, D.N.; Burmistrova, N.A.; Bondarenko, S.D.; Khlebtsov, B.N.; Atkin, V.S.; Shuvalov, A.A.; Zanishevskaya, A.A.; Skibina, Y.S.; Goryacheva, I.Y. Microstructured Waveguides with Polyelectrolyte-Stabilized Gold Nanostars for SERS Sensing of Dissolved Analytes. *Materials* **2018**, *11*, doi:10.3390/ma11050734.

91. Ermatov, T.; Noskov, R.E.; Machnev, A.A.; Gnusov, I.; Atkin, V.; Lazareva, E.N.; German, S.V.; Kosolobov, S.S.; Zatsepin, T.S.; Sergeeva, O.V.; et al. Multispectral Sensing of Biological Liquids with Hollow-Core Microstructured Optical Fibres. *Light Sci. Appl.* **2020**, *9*, 173, doi:10.1038/s41377-020-00410-8.

92. Bertucci, A.; Manicardi, A.; Candiani, A.; Giannetti, S.; Cucinotta, A.; Spoto, G.; Konstantaki, M.; Pissadakis, S.; Selleri, S.; Corradini, R. Detection of Unamplified Genomic DNA by a PNA-Based Microstructured Optical Fiber (MOF) Bragg-Grating Optofluidic System. *Biosens. Bioelectron.* **2015**, *63*, 248–254, doi:10.1016/j.bios.2014.07.047.

93. Warren-Smith, S.C.; Kostecki, R.; Nguyen, L.V.; Monro, T.M. Fabrication, Splicing, Bragg Grating Writing, and Polyelectrolyte Functionalization of Exposed-Core Microstructured Optical Fibers. *Opt. Express* **2014**, *22*, 29493, doi:10.1364/oe.22.029493.

94. Schwuchow, A.; Zobel, M.; Csaki, A.; Schröder, K.; Kobelke, J.; Fritzsche, W.; Schuster, K.; Benabid, F.; Bouwmans, G.; Knight, J.C.; et al. *Photonic-Crystal Fibers*; 2006; Vol. 24, pp. 4729–4749;.

95. Khozeymeh, F.; Melli, F.; Capodaglio, S.; Corradini, R.; Benabid, F.; Vincetti, L.; Cucinotta, A. Hollow-Core Fiber-Based Biosensor: A Platform for Lab-in-Fiber Optical Biosensors for DNA Detection. *Sensors* **2022**, *22*, doi:10.3390/s22145144.

96. Pidenko, P.; Vakh, C.; Shishov, A.; Skibina, J.; Burmistrova, N.; Bulatov, A. Microstructured Optical Fibers Sensor Modified by Deep Eutectic Solvent: Liquid-Phase Microextraction and Detection in One Analytical Device. *Talanta* **2021**, *232*, doi:10.1016/j.talanta.2021.122305.

97. Shao, L.; Liu, Z.; Hu, J.; Gunawardena, D.; Tam, H.Y. Optofluidics in Microstructured Optical Fibers. *Micromachines* **2018**, *9*, doi:10.3390/mi9040145.

98. Nguyen, L.V.; Hill, K.; Warren-Smith, S.; Monro, T. Interferometric-Type Optical Biosensor Based on Exposed Core Microstructured Optical Fiber. *Sens. Actuators B Chem.* **2015**, *221*, 320–327, doi:10.1016/j.snb.2015.06.068.

99. Ermatov, T.; Petrov, Y.V.; German, S.V.; Zanishevskaya, A.A.; Shuvalov, A.A.; Atkin, V.; Zakharevich, A.; Khlebtsov, B.N.; Skibina, J.S.; Ginzburg, P.; et al. Microstructured Optical Waveguide-Based Endoscopic Probe Coated with Silica Submicron Particles. *Materials* **2019**, *12*, doi:10.3390/ma12091424.

100. Liu, X.; Ding, W.; Wang, Y.; Gao, S.; Cao, L.; Feng, X.; Wang, P. Characterization of a Liquid-Filled Nodeless Anti-Resonant Fiber for Biochemical Sensing. *Opt. Lett.* **2017**, *42*, 863, doi:10.1364/ol.42.000863.

101. Ni, W.; Yang, C.; Luo, Y.; Xia, R.; Lu, P.; Hu, D.J.J.; Danto, S.; Shum, P.P.; Wei, L. Recent Advancement of Anti-Resonant Hollow-Core Fibers for Sensing Applications. *Photonics* **2021**, *8*, doi:10.3390/photonics8040128.
102. Heck, J.R.; Miele, E.; Mouthaan, R.; Frosz, M.H.; Knowles, T.P.J.; Euser, T.G. Label-Free Monitoring of Proteins in Optofluidic Hollow-Core Photonic Crystal Fibres. *Methods Appl. Fluoresc.* **2022**, *10*, doi:10.1088/2050-6120/ac9113.
103. Shukla, S.K.; Kushwaha, C.S.; Guner, T.; Demir, M.M. Chemically Modified Optical Fibers in Advanced Technology: An Overview. *Opt. Laser Technol.* **2019**, *115*, 404–432, doi:10.1016/j.optlastec.2019.02.025.
104. Li, L.; Zhang, Y. nan; Zhou, Y.; Zheng, W.; Sun, Y.; Ma, G.; Zhao, Y. Optical Fiber Optofluidic Bio-Chemical Sensors: A Review. *Laser Photonics Rev.* **2021**, *15*, doi:10.1002/lpor.202000526.
105. Zhang, N.; Li, K.; Cui, Y.; Wu, Z.; Shum, P.P.; Auguste, J.L.; Dinh, X.Q.; Humbert, G.; Wei, L. Ultra-Sensitive Chemical and Biological Analysis: Via Specialty Fibers with Built-in Microstructured Optofluidic Channels. *Lab. Chip* **2018**, *18*, 655–661, doi:10.1039/c7lc01247k.
106. Wang, Y.; Gao, R.; Xin, X. Hollow-Core Fiber Refractive Index Sensor with High Sensitivity and Large Dynamic Range Based on a Multiple Mode Transmission Mechanism. *Opt Express* **2021**, *29*, 19703–19714, doi:10.1364/OE.426705.
107. Chen, L.; Su, Q.; Liu, S.; Li, L. Infiltrated Hollow Core Fiber Interferometer for High Sensitive Temperature and Refractive Index Sensing. *Optik* **2021**, *243*, 167336, doi:https://doi.org/10.1016/j.ijleo.2021.167336.
108. Zhao, Y.; Li, X.-G.; Cai, L.; Zhang, Y.-N. Measurement of RI and Temperature Using Composite Interferometer With Hollow-Core Fiber and Photonic Crystal Fiber. *IEEE Trans. Instrum. Meas.* **2016**, *65*, 2631–2636, doi:10.1109/TIM.2016.2584390.
109. Liu, X.; WANG, Q.; WANG, D.N. Ultra Compact and Sensitive Optical Fiber Interferometric Refractive Index Sensor. *Optik* **2022**, *254*, 168642, doi:https://doi.org/10.1016/j.ijleo.2022.168642.
110. Zheng, K.; Shang, L. High-Linearity Refractive Index Sensor Based on Analyte-Filled Defect Hollow Core Bragg Fiber. *IEEE Photonics Technol. Lett.* **2017**, *29*, 1391–1394, doi:10.1109/LPT.2017.2723519.
111. Alam, M.K.; Vadivel, K.; Natesan, A.; Sghaireen, M.G.; Ganji, K.K.; Srivastava, K.C.; Nashwan, S.; Khader, Y. Design of Highly Sensitive Biosensors Using Hollow-Core Microstructured Fibers for Plasma Sensing in Aids with Human Metabolism. *Opt. Quantum Electron.* **2023**, *55*, 188, doi:10.1007/s11082-022-04514-w.
112. Gao, R.; Lu, D.; Cheng, J.; Qi, Z. Fiber Optic Refractive Index Sensor Using Optofluidic Anti-Resonant Reflecting Guidance. In Proceedings of the AOPC 2017: Fiber Optic Sensing and Optical Communications; Zhao, Z.-S., Wei, L., Liao, Y., Zhang, W., Jiang, D., Wang, W., Grattan, K.T.V., Eds.; SPIE, 2017; Vol. 10464, p. 104640N.
113. *Practical Raman Spectroscopy*; Gardiner, D.J., Graves, P.R., Eds.; Springer Berlin Heidelberg: Berlin, Heidelberg, 1989; ISBN 978-3-540-50254-8.

114. Cialla-May, D.; Krafft, C.; Rösch, P.; Deckert-Gaudig, T.; Frosch, T.; Jahn, I.J.; Pahlow, S.; Stiebing, C.; Meyer-Zedler, T.; Bocklitz, T.; et al. Raman Spectroscopy and Imaging in Bioanalytics. *Anal. Chem.* **2022**, *94*, 86–119, doi:10.1021/acs.analchem.1c03235.

115. Lawson, E.E.; Barry, B.W.; Williams, A.C.; Edwards, H.G.M. Biomedical Applications of Raman Spectroscopy. *J. Raman Spectrosc.* **1997**, *28*, 111–117, doi:10.1002/(SICI)1097-4555(199702)28:2/3<111::AID-JRS87>3.0.CO;2-Z.

116. Ferraro, J.R.; Nakamoto, K.; Brown, C.W. *Introductory Raman Spectroscopy*; 2nd ed.; Academic Press: Amsterdam ; Boston, 2003; ISBN 978-0-12-254105-6.

117. Knebl, A.; Yan, D.; Popp, J.; Frosch, T. Fiber Enhanced Raman Gas Spectroscopy. *TrAC - Trends Anal. Chem.* **2018**, *103*, 230–238, doi:10.1016/j.trac.2017.12.001.

118. Markin, A.V.; Markina, N.E.; Goryacheva, I.Y. Raman Spectroscopy Based Analysis inside Photonic-Crystal Fibers. *TrAC - Trends Anal. Chem.* **2017**, *88*, 185–197, doi:10.1016/j.trac.2017.01.003.

119. Yan, D.; Popp, J.; Pletz, M.W.; Frosch, T. Highly Sensitive Broadband Raman Sensing of Antibiotics in Step-Index Hollow-Core Photonic Crystal Fibers. *ACS Photonics* **2017**, *4*, 138–145, doi:10.1021/acsphotonics.6b00688.

120. Yang, X.; Zhang, A.Y.; Wheeler, D.A.; Bond, T.C.; Gu, C.; Li, Y. Direct Molecule-Specific Glucose Detection by Raman Spectroscopy Based on Photonic Crystal Fiber. *Anal. Bioanal. Chem.* **2012**, *402*, 687–691, doi:10.1007/s00216-011-5575-1.

121. Khetani, A.; Riordon, J.; Tiwari, V.; Momenpour, A.; Godin, M.; Anis, H. Hollow Core Photonic Crystal Fiber as a Reusable Raman Biosensor. *Opt. Express* **2013**, *21*, 12340, doi:10.1364/oe.21.012340.

122. Shi, C.; Zhang, Y.; Gu, C.; Seballos, L.; Zhang, J.Z. Low Concentration Biomolecular Detection Using Liquid Core Photonic Crystal Fiber (LCPCF) SERS Sensor. In Proceedings of the Optical Fibers and Sensors for Medical Diagnostics and Treatment Applications VIII; SPIE, February 7 2008; Vol. 6852, p. 685204.

123. Hanf, S.; Bögözi, T.; Keiner, R.; Frosch, T.; Popp, J. Fast and Highly Sensitive Fiber-Enhanced Raman Spectroscopic Monitoring of Molecular H $_2$ and CH $_4$ for Point-of-Care Diagnosis of Malabsorption Disorders in Exhaled Human Breath. *Anal. Chem.* **2015**, *87*, 982–988, doi:10.1021/ac503450y.

124. Hanf, S.; Keiner, R.; Yan, D.; Popp, J.; Frosch, T. Fiber-Enhanced Raman Multigas Spectroscopy: A Versatile Tool for Environmental Gas Sensing and Breath Analysis. *Anal. Chem.* **2014**, *86*, 5278–5285, doi:10.1021/ac404162w.

125. Langer, J.; Jimenez De Aberasturi, D.; Aizpurua, J.; Alvarez-Puebla, R.A.; Auguié, B.; Baumberg, J.J.; Bazan, G.C.; Bell, S.E.J.; Boisen, A.; Brolo, A.G.; et al. Present and Future of Surface-Enhanced Raman Scattering. *ACS Nano* **2020**, *14*, 28–117, doi:10.1021/acsnano.9b04224.

126. Cox, F.M.; Argyros, A.; Large, M.C.J.; Kalluri, S. Surface Enhanced Raman Scattering in a Hollow Core Microstructured Optical Fiber. *Opt. Express* **2007**, *15*, 13675, doi:10.1364/OE.15.013675.

127. Yang, X.; Shi, C.; Wheeler, D.; Newhouse, R.; Chen, B.; Zhang, J.Z.; Gu, C. High-Sensitivity Molecular Sensing Using Hollow-Core Photonic Crystal Fiber and

Surface-Enhanced Raman Scattering. *J. Opt. Soc. Am. A* **2010**, *27*, 977, doi:10.1364/JOSAA.27.000977.

128. Hunter, R.; Sohi, A.N.; Khatoon, Z.; Berthiaume, V.R.; Alarcon, E.I.; Godin, M.; Anis, H. Optofluidic Label-Free SERS Platform for Rapid Bacteria Detection in Serum. *Sens. Actuators B Chem.* **2019**, *300*, doi:10.1016/j.snb.2019.126907.

129. Sun, Z.; Kang, C.; Fang, X.; Liu, H.; Guo, J.; Zhang, X. A SERS-Active Capillary for Direct Molecular Trace Detection in Liquids. *Nanoscale Adv.* **2021**, *3*, 2617–2622, doi:10.1039/d1na00082a.

130. Zhang, Y.; Shi, C.; Gu, C.; Seballos, L.; Zhang, J.Z. Liquid Core Photonic Crystal Fiber Sensor Based on Surface Enhanced Raman Scattering. *Appl. Phys. Lett.* **2007**, *90*, 193504, doi:10.1063/1.2738185.

131. Eftekhari, F.; Lee, A.; Kumacheva, E.; Helmy, A.S. Examining Metal Nanoparticle Surface Chemistry Using Hollow-Core, Photonic-Crystal, Fiber-Assisted SERS. *Opt. Lett.* **2012**, *37*, 680, doi:10.1364/OL.37.000680.

132. Khetani, A.; Tiwari, V.S.; Momenpour, A.; Anis, H. Monitoring of Adenosine within Hollow Core Photonic Crystal Fiber by Surface Enhanced Raman Scattering (SERS). In Proceedings of the 2011 11th IEEE International Conference on Nanotechnology; IEEE: Portland, OR, USA, August 2011; pp. 973–977.

133. Tiwari, V.S.; Khetani, A.; Naji, M.; Anis, H. Study of Surface Enhanced Raman Scattering (SERS) within Hollow Core Photonic Crystal Fiber. In Proceedings of the 2009 IEEE Sensors; IEEE: Christchurch, New Zealand, October 2009; pp. 367–370.

134. Yang, X.; Gu, C.; Qian, F.; Li, Y.; Zhang, J.Z. Highly Sensitive Detection of Proteins and Bacteria in Aqueous Solution Using Surface-Enhanced Raman Scattering and Optical Fibers. *Anal. Chem.* **2011**, *83*, 5888–5894, doi:10.1021/ac200707t.

135. Dinish, U.S.; Fu, C.Y.; Soh, K.S.; Ramaswamy, B.; Kumar, A.; Olivo, M. Highly Sensitive SERS Detection of Cancer Proteins in Low Sample Volume Using Hollow Core Photonic Crystal Fiber. *Biosens. Bioelectron.* **2012**, *33*, 293–298, doi:10.1016/j.bios.2011.12.056.

136. Dinish, U.S.; Balasundaram, G.; Chang, Y.T.; Olivo, M. Sensitive Multiplex Detection of Serological Liver Cancer Biomarkers Using SERS-Active Photonic Crystal Fiber Probe. *J. Biophotonics* **2014**, *7*, 956–965, doi:10.1002/jbio.201300084.

137. Kahraman, M.; Mullen, E.R.; Korkmaz, A.; Wachsmann-Hogiu, S. Fundamentals and Applications of SERS-Based Bioanalytical Sensing. *Nanophotonics* **2017**, *6*, 831–852, doi:10.1515/nanoph-2016-0174.

138. Geng, Y.; Xu, Y.; Tan, X.; Wang, L.; Li, X.; Du, Y.; Hong, X. A Simplified Hollow-Core Photonic Crystal Fiber SERS Probe with a Fully Filled Photoreduction Silver Nanoprism. *Sensors* **2018**, *18*, 1726, doi:10.3390/s18061726.

139. Li, P.; Long, F.; Chen, W.; Chen, J.; Chu, P.K.; Wang, H. Fundamentals and Applications of Surface-Enhanced Raman Spectroscopy–Based Biosensors. *Curr. Opin. Biomed. Eng.* **2020**, *13*, 51–59, doi:10.1016/j.cobme.2019.08.008.

140. Schøler, L.V.; Reinert, T.; Ørntoft, M.-B.W.; Kassentoft, C.G.; Árnadóttir, S.S.; Vang, S.; Nordentoft, I.; Knudsen, M.; Lamy, P.; Andreasen, D.; et al. Clinical Implications of Monitoring Circulating Tumor DNA in Patients with Colorectal Cancer. *Clin. Cancer Res.* **2017**, *23*, 5437–5445, doi:10.1158/1078-0432.CCR-17-0510.

141. Cheng, F.; Su, L.; Qian, C. Circulating Tumor DNA: A Promising Biomarker in the Liquid Biopsy of Cancer. *Oncotarget* **2016**, *7*, 48832–48841, doi:10.18632/oncotarget.9453.

142. Johann, D.J.; Steliga, M.; Shin, I.J.; Yoon, D.; Arnaoutakis, K.; Hutchins, L.; Liu, M.; Liem, J.; Walker, K.; Pereira, A.; et al. Liquid Biopsy and Its Role in an Advanced Clinical Trial for Lung Cancer. *Exp. Biol. Med.* **2018**, *243*, 262–271, doi:10.1177/1535370217750087.

143. Gale, D.; Lawson, A.R.J.; Howarth, K.; Madi, M.; Durham, B.; Smalley, S.; Calaway, J.; Blais, S.; Jones, G.; Clark, J.; et al. Development of a Highly Sensitive Liquid Biopsy Platform to Detect Clinically-Relevant Cancer Mutations at Low Allele Fractions in Cell-Free DNA. *PLOS ONE* **2018**, *13*, e0194630, doi:10.1371/journal.pone.0194630.

144. Théry, C.; Witwer, K.W.; Aikawa, E.; Alcaraz, M.J.; Anderson, J.D.; Andriantsitohaina, R.; Antoniou, A.; Arab, T.; Archer, F.; Atkin-Smith, G.K.; et al. Minimal Information for Studies of Extracellular Vesicles 2018 (MISEV2018): A Position Statement of the International Society for Extracellular Vesicles and Update of the MISEV2014 Guidelines. *J. Extracell. Vesicles* **2018**, *7*, doi:10.1080/20013078.2018.1535750.

145. Tkach, M.; Théry, C. Communication by Extracellular Vesicles: Where We Are and Where We Need to Go. *Cell* **2016**, *164*, 1226–1232, doi:10.1016/j.cell.2016.01.043.

146. Tkach, M.; Kowal, J.; Théry, C. Why the Need and How to Approach the Functional Diversity of Extracellular Vesicles. *Philos. Trans. R. Soc. B Biol. Sci.* **2017**, *373*, 20160479, doi:10.1098/rstb.2016.0479.

147. Arraud, N.; Linares, R.; Tan, S.; Gounou, C.; Pasquet, J.M.; Mornet, S.; Brisson, A.R. Extracellular Vesicles from Blood Plasma: Determination of Their Morphology, Size, Phenotype and Concentration. *J. Thromb. Haemost. JTH* **2014**, *12*, 614–627, doi:10.1111/JTH.12554.

148. Serrano-Pertierra, E.; Oliveira-Rodríguez, M.; Rivas, M.; Oliva, P.; Villafani, J.; Navarro, A.; Blanco-López, M.C.; Cernuda-Morollón, E. Characterization of Plasma-Derived Extracellular Vesicles Isolated by Different Methods: A Comparison Study. *Bioeng. Basel Switz.* **2019**, *6*, doi:10.3390/BIOENGINEERING6010008.

149. Tian, Y.; Gong, M.; Hu, Y.; Liu, H.; Zhang, W.; Zhang, M.; Hu, X.; Aubert, D.; Zhu, S.; Wu, L.; et al. Quality and Efficiency Assessment of Six Extracellular Vesicle Isolation Methods by Nano-Flow Cytometry. *J. Extracell. Vesicles* **2020**, *9*, 1697028, doi:10.1080/20013078.2019.1697028.

150. Kang, H.; Kim, J.; Park, J. Methods to Isolate Extracellular Vesicles for Diagnosis. *Micro Nano Syst. Lett.* **2017**, *5*, 1–11, doi:10.1186/S40486-017-0049-7/FIGURES/7.

151. Konoshenko, M.Y.; Lekchnov, E.A.; Vlassov, A. V.; Laktionov, P.P. Isolation of Extracellular Vesicles: General Methodologies and Latest Trends. *BioMed Res. Int.* **2018**, *2018*, doi:10.1155/2018/8545347.

152. Théry, C.; Amigorena, S.; Raposo, G.; Clayton, A. Isolation and Characterization of Exosomes from Cell Culture Supernatants and Biological Fluids. *Curr. Protoc. Cell Biol.* **2006**, *30*, 3.22.1-3.22.29, doi:10.1002/0471143030.CB0322S30.

153. Busatto, S.; Vilanilam, G.; Ticer, T.; Lin, W.L.; Dickson, D.W.; Shapiro, S.; Bergese, P.; Wolfram, J. Tangential Flow Filtration for Highly Efficient Concentration of Extracellular Vesicles from Large Volumes of Fluid. *Cells 2018 Vol 7 Page 273* **2018**, *7*, 273, doi:10.3390/CELLS7120273.

154. Zhang, K.; Yue, Y.; Wu, S.; Liu, W.; Shi, J.; Zhang, Z. Rapid Capture and Nondestructive Release of Extracellular Vesicles Using Aptamer-Based Magnetic Isolation. *ACS Sens.* **2019**, *4*, 1245–1251, doi:10.1021/ACSSENSORS.9B00060.

155. Zabegina, L.; Nazarova, I.; Knyazeva, M.; Nikiforova, N.; Slyusarenko, M.; Titov, S.; Vasilyev, D.; Sleptsov, I.; Malek, A. MiRNA Let-7 from TPO(+) Extracellular Vesicles Is a Potential Marker for a Differential Diagnosis of Follicular Thyroid Nodules. *Cells 2020 Vol 9 Page 1917* **2020**, *9*, 1917, doi:10.3390/CELLS9081917.

156. Zabeo, D.; Cvjetkovic, A.; Lässer, C.; Schorb, M.; Lötvall, J.; Höög, J.L. Exosomes Purified from a Single Cell Type Have Diverse Morphology. *J. Extracell. Vesicles* **2017**, *6*, doi:10.1080/20013078.2017.1329476.

157. Cantin, R.; Diou, J.; Bélanger, D.; Tremblay, A.M.; Gilbert, C. Discrimination between Exosomes and HIV-1: Purification of Both Vesicles from Cell-Free Supernatants. *J. Immunol. Methods* **2008**, *338*, 21–30, doi:10.1016/J.JIM.2008.07.007.

158. Baranyai, T.; Herczeg, K.; Onódi, Z.; Voszka, I.; Módos, K.; Marton, N.; Nagy, G.; Mäger, I.; Wood, M.J.; El Andaloussi, S.; et al. Isolation of Exosomes from Blood Plasma: Qualitative and Quantitative Comparison of Ultracentrifugation and Size Exclusion Chromatography Methods. *PloS One* **2015**, *10*, doi:10.1371/JOURNAL.PONE.0145686.

159. Tauro, B.J.; Greening, D.W.; Mathias, R.A.; Ji, H.; Mathivanan, S.; Scott, A.M.; Simpson, R.J. Comparison of Ultracentrifugation, Density Gradient Separation, and Immunoaffinity Capture Methods for Isolating Human Colon Cancer Cell Line LIM1863-Derived Exosomes. *Methods San Diego Calif* **2012**, *56*, 293–304, doi:10.1016/J.YMETH.2012.01.002.

160. Nordin, J.Z.; Lee, Y.; Vader, P.; Mäger, I.; Johansson, H.J.; Heusermann, W.; Wiklander, O.P.B.; Hällbrink, M.; Seow, Y.; Bultema, J.J.; et al. Ultrafiltration with Size-Exclusion Liquid Chromatography for High Yield Isolation of Extracellular Vesicles Preserving Intact Biophysical and Functional Properties. *Nanomedicine Nanotechnol. Biol. Med.* **2015**, *11*, 879–883, doi:10.1016/J.NANO.2015.01.003.

161. Merchant, M.L.; Powell, D.W.; Wilkey, D.W.; Cummins, T.D.; Deegens, J.K.; Rood, I.M.; McAfee, K.J.; Fleischer, C.; Klein, E.; Klein, J.B. Microfiltration Isolation of Human Urinary Exosomes for Characterization by MS. *PROTEOMICS – Clin. Appl.* **2010**, *4*, 84–96, doi:10.1002/PRCA.200800093.

162. Rekker, K.; Saare, M.; Roost, A.M.; Kubo, A.L.; Zarovni, N.; Chiesi, A.; Salumets, A.; Peters, M. Comparison of Serum Exosome Isolation Methods for microRNA Profiling. *Clin. Biochem.* **2014**, *47*, 135–138, doi:10.1016/J.CLINBIOCHEM.2013.10.020.

163. Petersen, K.E.; Shiri, F.; White, T.; Bardi, G.T.; Sant, H.; Gale, B.K.; Hood, J.L. Exosome Isolation: Cyclical Electrical Field Flow Fractionation in Low-Ionic-Strength Fluids. *Anal. Chem.* **2018**, *90*, 12783–12790, doi:10.1021/ACS.ANALCHEM.8B03146/SUPPL_FILE/AC8B03146_SI_001.PDF.

164. Yamada, T.; Inoshima, Y.; Matsuda, T.; Ishiguro, N. Comparison of Methods for Isolating Exosomes from Bovine Milk. *J. Vet. Med. Sci.* **2012**, *74*, 1523–1525, doi:10.1292/JVMS.12-0032.

165. Wu, M.; Ouyang, Y.; Wang, Z.; Zhang, R.; Huang, P.H.; Chen, C.; Li, H.; Li, P.; Quinn, D.; Dao, M.; et al. Isolation of Exosomes from Whole Blood by Integrating Acoustics and Microfluidics. *Proc. Natl. Acad. Sci. U. S. A.* **2017**, *114*, 10584–10589, doi:10.1073/PNAS.1709210114/SUPPL_FILE/PNAS.201709210SI.PDF.

166. Liu, C.; Guo, J.; Tian, F.; Yang, N.; Yan, F.; Ding, Y.; Wei, J.; Hu, G.; Nie, G.; Sun, J. Field-Free Isolation of Exosomes from Extracellular Vesicles by Microfluidic Viscoelastic Flows. *ACS Nano* **2017**, *11*, 6968–6976, doi:10.1021/ACSNANO.7B02277.

167. Zhao, Z.; Yang, Y.; Zeng, Y.; He, M. A Microfluidic ExoSearch Chip for Multiplexed Exosome Detection towards Blood-Based Ovarian Cancer Diagnosis. *Lab. Chip* **2016**, *16*, 489–496, doi:10.1039/C5LC01117E.

168. Kanwar, S.S.; Dunlay, C.J.; Simeone, D.M.; Nagrath, S. Microfluidic Device (ExoChip) for on-Chip Isolation, Quantification and Characterization of Circulating Exosomes. *Lab. Chip* **2014**, *14*, 1891–1900, doi:10.1039/C4LC00136B.

169. He, M.; Crow, J.; Roth, M.; Zeng, Y.; Godwin, A.K. Integrated Immunoisolation and Protein Analysis of Circulating Exosomes Using Microfluidic Technology. *Lab. Chip* **2014**, *14*, 3773–3780, doi:10.1039/C4LC00662C.

170. Dragovic, R.A.; Gardiner, C.; Brooks, A.S.; Tannetta, D.S.; Ferguson, D.J.P.; Hole, P.; Carr, B.; Redman, C.W.G.; Harris, A.L.; Dobson, P.J.; et al. Sizing and Phenotyping of Cellular Vesicles Using Nanoparticle Tracking Analysis. *Nanomedicine Nanotechnol. Biol. Med.* **2011**, *7*, 780–788, doi:10.1016/J.NANO.2011.04.003.

171. Gardiner, C.; Ferreira, Y.J.; Dragovic, R.A.; Redman, C.W.G.; Sargent, I.L. Extracellular Vesicle Sizing and Enumeration by Nanoparticle Tracking Analysis. *J. Extracell. Vesicles* **2013**, *2*, 19671, doi:10.3402/JEV.V2I0.19671.

172. Akers, J.C.; Ramakrishnan, V.; Nolan, J.P.; Duggan, E.; Fu, C.C.; Hochberg, F.H.; Chen, C.C.; Carter, B.S. Comparative Analysis of Technologies for Quantifying

Extracellular Vesicles (EVs) in Clinical Cerebrospinal Fluids (CSF). *PLOS ONE* **2016**, *11*, e0149866, doi:10.1371/JOURNAL.PONE.0149866.

173. Van Der Pol, E.; Van Gemert, M.J.C.; Sturk, A.; Nieuwland, R.; Van Leeuwen, T.G. Single vs. Swarm Detection of Microparticles and Exosomes by Flow Cytometry. *J. Thromb. Haemost.* **2012**, *10*, 919–930, doi:10.1111/j.1538-7836.2012.04683.x.

174. Tian, T.; Zhu, Y.L.; Hu, F.H.; Wang, Y.Y.; Huang, N.P.; Xiao, Z.D. Dynamics of Exosome Internalization and Trafficking. *J. Cell. Physiol.* **2013**, *228*, 1487–1495, doi:10.1002/JCP.24304.

175. Suetsugu, A.; Honma, K.; Saji, S.; Moriwaki, H.; Ochiya, T.; Hoffman, R.M. Imaging Exosome Transfer from Breast Cancer Cells to Stroma at Metastatic Sites in Orthotopic Nude-Mouse Models. *Adv. Drug Deliv. Rev.* **2013**, *65*, 383–390, doi:10.1016/J.ADDR.2012.08.007.

176. Im, H.; Shao, H.; Park, Y. Il; Peterson, V.M.; Castro, C.M.; Weissleder, R.; Lee, H. Label-Free Detection and Molecular Profiling of Exosomes with a Nano-Plasmonic Sensor. *Nat. Biotechnol. 2014 325* **2014**, *32*, 490–495, doi:10.1038/nbt.2886.

177. Estifeeva, T.M.; Barmin, R.A.; Rudakovskaya, P.G.; Nechaeva, A.M.; Luss, A.L.; Mezhuev, Y.O.; Chernyshev, V.S.; Krivoborodov, E.G.; Klimenko, O.A.; Sindeeva, O.A.; et al. Hybrid (Bovine Serum Albumin)/Poly(N-Vinyl-2-Pyrrolidone- Co-Acrylic Acid)-Shelled Microbubbles as Advanced Ultrasound Contrast Agents. *ACS Appl. Bio Mater.* **2022**, *5*, 3338–3348, doi:10.1021/acsabm.2c00331.

178. Nechaeva, A.M.; Artyukhov, A.A.; Luss, A.L.; Shtilman, M.I.; Svistunova, A.Y.; Motyakin, M.V.; Levina, I.I.; Krivoborodov, E.G.; Toropygin, I.Y.; Chistyakov, E.M.; et al. The Synthesis and Properties of a New Carrier for Paclitaxel and Doxorubicin Based on the Amphiphilic Copolymer of N-Vinyl-2-Pyrrolidone and Acrylic Acid. *Macromol. Chem. Phys.* **2022**, *223*, 2200081, doi:10.1002/MACP.202200081.

179. Artyukhov, A.A.; Nechaeva, A.M.; Shtilman, M.I.; Chistyakov, E.M.; Svistunova, A.Y.; Bagrov, D.V.; Kuskov, A.N.; Docea, A.O.; Tsatsakis, A.M.; Gurevich, L. Nanoaggregates of Biphilic Carboxyl-Containing Copolymers as Carriers for Ionically Bound Doxorubicin. *Materials* **2022**, *15*, 7136.

180. Duff, D.G.; Baiker, A.; Edwards, P.P. A New Hydrosol of Gold Clusters. 1. Formation and Particle Size Variation. *Langmuir* **1993**, *9*, 2301–2309.

181. Turkevich, J.; Stevenson, P.C.; Hillier, J. A Study of the Nucleation and Growth Processes in the Synthesis of Colloidal Gold. *Discuss. Faraday Soc.* **1951**, *11*, 55–75, doi:10.1039/DF9511100055.

182. Obeed, H.H.; Tahir, K.J.; Ridha, N.J.; Alosfur, F.K.M.; Madlol, R. Linear and Nonlinear Optical Properties of Rhodamine 6G. *IOP Conf. Ser. Mater. Sci. Eng.* **2020**, *928*, 072024, doi:10.1088/1757-899X/928/7/072024.

183. Hirayama, K.; Akashi, S.; Furuya, M.; Fukuhara, K. Rapid Confirmation and Revision of the Primary Structure of Bovine Serum Albumin by ESIMS and Frit-

FAB LC/MS. *Biochem. Biophys. Res. Commun.* **1990**, *173*, 639–646, doi:10.1016/S0006-291X(05)80083-X.

184. Hernández, B.; Pflüger, F.; Kruglik, S.G.; Ghomi, M. Characteristic Raman Lines of Phenylalanine Analyzed by a Multiconformational Approach. *J. Raman Spectrosc.* **2013**, *44*, 827–833, doi:10.1002/jrs.4290.

185. Lin, V.J.C.; Koenig, J.L. Raman Studies of Bovine Serum Albumin. *Biopolymers* **1976**, *15*, 203–218, doi:10.1002/bip.1976.360150114.

186. Szekeres, G.P.; Kneipp, J. SERS Probing of Proteins in Gold Nanoparticle Agglomerates. *Front. Chem.* **2019**, *7*, 1–10, doi:10.3389/fchem.2019.00030.

187. Rygula, A.; Majzner, K.; Marzec, K.M.; Kaczor, A.; Pilarczyk, M.; Baranska, M. Raman Spectroscopy of Proteins: A Review. *J. Raman Spectrosc.* **2013**, *44*, 1061–1076, doi:10.1002/jrs.4335.

188. Nemecek, D.; Stepanek, J.; Thomas, G.J. *Raman Spectroscopy of Proteins and Nucleoproteins*; 2013; ISBN 0-471-14086-4.

189. Yang, X.; Zhang, A.Y.; Wheeler, D.A.; Bond, T.C.; Gu, C.; Li, Y. Direct Molecule-Specific Glucose Detection by Raman Spectroscopy Based on Photonic Crystal Fiber. *Anal. Bioanal. Chem.* **2012**, *402*, 687–691, doi:10.1007/s00216-011-5575-1.

190. Khetani, A.; Riordon, J.; Tiwari, V.; Momenpour, A.; Godin, M.; Anis, H. Hollow Core Photonic Crystal Fiber as a Reusable Raman Biosensor. *Opt. Express* **2013**, *21*, 12340, doi:10.1364/oe.21.012340.

191. Chiang, C.Y.; Liu, T.Y.; Su, Y.A.; Wu, C.H.; Cheng, Y.W.; Cheng, H.W.; Jeng, R.J. Au Nanoparticles Immobilized on Honeycomb-like Polymeric Films for Surface-Enhanced Raman Scattering (SERS) Detection. *Polymers* **2017**, *9*, doi:10.3390/polym9030093.

192. Wu, C.; Chen, E.; Wei, J. Surface Enhanced Raman Spectroscopy of Rhodamine 6G on Agglomerates of Different-Sized Silver Truncated Nanotriangles. *Colloids Surf. Physicochem. Eng. Asp.* **2016**, *506*, 450–456, doi:10.1016/j.colsurfa.2016.07.020.

193. He, X.N.; Gao, Y.; Mahjouri-Samani, M.; Black, P.N.; Allen, J.; Mitchell, M.; Xiong, W.; Zhou, Y.S.; Jiang, L.; Lu, Y.F. Surface-Enhanced Raman Spectroscopy Using Gold-Coated Horizontally Aligned Carbon Nanotubes. *Nanotechnology* **2012**, *23*, doi:10.1088/0957-4484/23/20/205702.

194. Le Ru, E.C.; Etchegoin, P.G. SERS Enhancement Factors and Related Topics. In *Principles of Surface-Enhanced Raman Spectroscopy*; 2009; pp. 185–264.

195. Dinish, U.S.; Fu, C.Y.; Soh, K.S.; Ramaswamy, B.; Kumar, A.; Olivo, M. Highly Sensitive SERS Detection of Cancer Proteins in Low Sample Volume Using Hollow Core Photonic Crystal Fiber. *Biosens. Bioelectron.* **2012**, *33*, 293–298, doi:10.1016/j.bios.2011.12.056.

196. White, D.J.; Stoddart, P.R. Nanostructured Optical Fiber with Surface-Enhanced Raman Scattering Functionality. *Opt. Lett. Vol 30 Issue 6 Pp 598-600* **2005**, *30*, 598–600, doi:10.1364/OL.30.000598.

197. Ermatov, T.; Gnusov, I.; Skibina, J.; Noskov, R.E.; Gorin, D. Noncontact Characterization of Microstructured Optical Fibers Coating in Real Time. *Opt. Lett. Vol 46 Issue 19 Pp 4793-4796* **2021**, *46*, 4793–4796, doi:10.1364/OL.433208.
198. Noskov, R.E.; Zanishevskaya, A.A.; Shuvalov, A.A.; German, S.V.; Inozemtseva, O.A.; Kochergin, T.P.; Lazareva, E.N.; Tuchin, V.V.; Ginzburg, P.; Skibina, J.S.; et al. Enabling Magnetic Resonance Imaging of Hollow-Core Microstructured Optical Fibers via Nanocomposite Coating. *Opt. Express* **2019**, *27*, 9868, doi:10.1364/oe.27.009868.
199. Johnson, P.B.; Christy, R.W. Optical Constants of the Noble Metals. *Phys. Rev. B* **1972**, *6*, 4370, doi:10.1103/PhysRevB.6.4370.
200. Mu, Y.; Liu, M.; Li, J.; Zhang, X. Plasmonic Hollow Fibers with Distributed Inner-Wall Hotspots for Direct SERS Detection of Flowing Liquids. *Opt. Lett.* **2021**, *46*, 1369, doi:10.1364/ol.415733.
201. Xu, Y.; Bai, P.; Zhou, X.; Akimov, Y.; Png, C.E.; Ang, L.-K.; Knoll, W.; Wu, L.; Xu, Y.; Bai, P.; et al. Optical Refractive Index Sensors with Plasmonic and Photonic Structures: Promising and Inconvenient Truth. *Adv. Opt. Mater.* **2019**, *7*, 1801433, doi:10.1002/adom.201801433.
202. Hassan, J.Z.; Raza, A.; Ud, Z.; Babar, D.; Qumar, U.; Kaner, N.T.; Cassinese, A.; Hassan, † J Z; Raza, A.; Babar, Z.U.D. Open Access Article. **2023**, doi:10.1039/d2ta07653e.
203. Perlmann, G.E.; Longsworth, L.G. The Specific Refractive Increment of Some Purified Proteins. *J. Am. Chem. Soc.* **1948**, *70*, 2719–2724, doi:10.1021/ja01188a027.
204. Andersen, M.; Painter, L.R.; Nir, S. Dispersion Equation and Polarizability of Bovine Serum Albumin from Measurements of Refractive Indices. *Biopolymers* **1974**, *13*, 1261–1267, doi:10.1002/BIP.1974.360130616.
205. Taylor, L.S.; Langkilde, F.W.; Zografi, G. Fourier Transform Raman Spectroscopic Study of the Interaction of Water Vapor with Amorphous Polymers. *J. Pharm. Sci.* **2001**, *90*, 888–901, doi:10.1002/jps.1041.
206. McDermott, D.P. Vibrational Assignments and Normal-Coordinate Analyses of γ-Butyrolactone and 2-Pyrrolidinones. *J. Phys. Chem.* **1986**, *90*, 2569–2574, doi:10.1021/j100403a006.
207. Sánchez-Márquez, J.A.; Fuentes-Ramírez, R.; Cano-Rodríguez, I.; Gamiño-Arroyo, Z.; Rubio-Rosas, E.; Kenny, J.M.; Rescignano, N. Membrane Made of Cellulose Acetate with Polyacrylic Acid Reinforced with Carbon Nanotubes and Its Applicability for Chromium Removal. *Int. J. Polym. Sci.* **2015**, *2015*, doi:10.1155/2015/320631.
208. Murli, C.; Song, Y. Pressure-Induced Polymerization of Acrylic Acid: A Raman Spectroscopic Study. *J. Phys. Chem. B* **2010**, *114*, 9744–9750, doi:10.1021/jp1034757.
209. Lee, M.; Lee, E.Y.; Lee, D.; Park, B.J. Stabilization and Fabrication of Microbubbles: Applications for Medical Purposes and Functional Materials. *Soft Matter* **2015**, *11*, 2067–2079.

210. Upadhyay, A.; Dalvi, S.V. Microbubble Formulations: Synthesis, Stability, Modeling and Biomedical Applications. *Ultrasound Med. Biol.* **2019**, *45*, 301–343, doi:https://doi.org/10.1016/j.ultrasmedbio.2018.09.022.

211. Kuriakose, M.; Borden, M.A. Microbubbles and Nanodrops for Photoacoustic Tomography. *Curr. Opin. Colloid Interface Sci.* **2021**, *55*, 101464, doi:https://doi.org/10.1016/j.cocis.2021.101464.

212. Chakraborty, B.; Basu, S. Interaction of BSA with Proflavin: A Spectroscopic Approach. *J. Lumin.* **2009**, *129*, 34–39, doi:https://doi.org/10.1016/j.jlumin.2008.07.012.

213. Barik, A.; Priyadarsini, K.I.; Mohan, H. Photophysical Studies on Binding of Curcumin to Bovine Serum Albumin¶. *Photochem. Photobiol.* **2003**, *77*, 597–603.

214. Laborde, B.; Moine-Ledoux, V.; Richard, T.; Saucier, C.; Dubourdieu, D.; Monti, J.P. PVPP−Polyphenol Complexes: A Molecular Approach. *J. Agric. Food Chem.* **2006**, *54*, 4383–4389, doi:10.1021/JF060427A.

215. Slyusarenko, M.; Nikiforova, N.; Sidina, E.; Nazarova, I.; Egorov, V.; Garmay, Y.; Merdalimova, A.; Yevlampieva, N.; Gorin, D.; Malek, A. Formation and Evaluation of a Two-Phase Polymer System in Human Plasma as a Method for Extracellular Nanovesicle Isolation. *Polymers* **2021**, *13*, 1–16, doi:10.3390/polym13030458.

216. Chernyshev, V.S.; Chuprov-Netochin, R.N.; Tsydenzhapova, E.; Svirshchevskaya, E.V.; Poltavtseva, R.A.; Merdalimova, A.; Yashchenok, A.; Keshelava, A.; Sorokin, K.; Keshelava, V.; et al. Asymmetric Depth-Filtration: A Versatile and Scalable Method for High-Yield Isolation of Extracellular Vesicles with Low Contamination. *J. Extracell. Vesicles* **2022**, *11*, doi:10.1002/jev2.12256.

217. Krafft, C.; Wilhelm, K.; Eremin, A.; Nestel, S.; von Bubnoff, N.; Schultze-Seemann, W.; Popp, J.; Nazarenko, I. A Specific Spectral Signature of Serum and Plasma-Derived Extracellular Vesicles for Cancer Screening. *Nanomedicine Nanotechnol. Biol. Med.* **2017**, *13*, 835–841, doi:10.1016/j.nano.2016.11.016.

218. Lee, C.; Carney, R.P.; Hazari, S.; Smith, Z.J.; Knudson, A.; Robertson, C.S.; Lam, K.S.; Wachsmann-Hogiu, S. 3D Plasmonic Nanobowl Platform for the Study of Exosomes in Solution. *Nanoscale* **2015**, *7*, 9290–9297, doi:10.1039/c5nr01333j.

219. Gualerzi, A.; Kooijmans, S.A.A.; Niada, S.; Picciolini, S.; Brini, A.T.; Camussi, G.; Bedoni, M. Raman Spectroscopy as a Quick Tool to Assess Purity of Extracellular Vesicle Preparations and Predict Their Functionality. *J. Extracell. Vesicles* **2019**, *8*, doi:10.1080/20013078.2019.1568780.

220. Czamara, K.; Majzner, K.; Pacia, M.Z.; Kochan, K.; Kaczor, A.; Baranska, M. Raman Spectroscopy of Lipids: A Review. *J. Raman Spectrosc.* **2015**, *46*, 4–20, doi:10.1002/jrs.4607.

221. Stone, N.; Kendall, C.; Smith, J.; Crow, P.; Barr, H. Raman Spectroscopy for Identification of Epithelial Cancers. *Faraday Discuss.* **2004**, *126*, 141–157, doi:10.1039/b304992b.

222. Stremersch, S.; Marro, M.; Pinchasik, B.E.; Baatsen, P.; Hendrix, A.; De Smedt, S.C.; Loza-Alvarez, P.; Skirtach, A.G.; Raemdonck, K.; Braeckmans, K.

Identification of Individual Exosome-like Vesicles by Surface Enhanced Raman Spectroscopy. *Small* **2016**, *12*, 3292–3301, doi:10.1002/smll.201600393.

223. Notingher, I.; Verrier, S.; Haque, S.; Polak, J.M.; Hench, L.L. Spectroscopic Study of Human Lung Epithelial Cells (A549) in Culture: Living Cells versus Dead Cells. *Biopolymers* **2003**, *72*, 230–240, doi:10.1002/bip.10378.

224. Richter, M.; Hedegaard, M.; Deckert-Gaudig, T.; Lampen, P.; Deckert, V. Laterally Resolved and Direct Spectroscopic Evidence of Nanometer-Sized Lipid and Protein Domains on a Single Cell. *Small* **2011**, *7*, 209–214, doi:10.1002/smll.201001503.

225. Takeuchi, H. Raman Structural Markers of Tryptophan and Histidine Side Chains in Proteins. *Biopolym. - Biospectroscopy Sect.* **2003**, *72*, 305–317, doi:10.1002/bip.10440.

226. Harada, I.; Miura, T.; Takeuchi, H. Origin of the Doublet at 1360 and 1340 Cm-1 in the Raman Spectra of Tryptophan and Related Compounds. *Spectrochim. Acta Part Mol. Spectrosc.* **1986**, *42*, 307–312, doi:10.1016/0584-8539(86)80193-3.

227. Enciso-Martinez, A.; Van Der Pol, E.; Hau, C.M.; Nieuwland, R.; Van Leeuwen, T.G.; Terstappen, L.W.M.M.; Otto, C. Label-Free Identification and Chemical Characterisation of Single Extracellular Vesicles and Lipoproteins by Synchronous Rayleigh and Raman Scattering. *J. Extracell. Vesicles* **2020**, *9*, doi:10.1080/20013078.2020.1730134.

228. Mohammadi, M.R.; Malkovskiy, A.V.; Jothimuthu, P.; Kim, K.M.; Parekh, M.; Inayathullah, M.; Zhuge, Y.; Rajadas, J. PEG/Dextran Double Layer Influences Fe Ion Release and Colloidal Stability of Iron Oxide Nanoparticles. *Sci. Rep.* **2018**, *8*, 1–11, doi:10.1038/s41598-018-22644-8.

229. Koenig, L.; Angood, A.C. Spectra of Poly(Ethy1ene Glycols) in Solution. *J. Polym. Sci. Part -2* **1970**, *8*, 1787–1796.

230. Zhbankov, R.G.; Andrianov, V.M.; Marchewka, M.K. Fourier Transform IR and Raman Spectroscopy and Structure of Carbohydrates. *J. Mol. Struct.* **1997**, *436–437*, 637–654, doi:10.1016/S0022-2860(97)00141-5.

231. Siew, D.C.W.; Cooney, R.P.; Taylor, M.J.; Wiggins, P.M. Vibrational Spectroscopic Studies of Aqueous Dextran Sulphate. *J. Raman Spectrosc.* **1994**, *25*, 727–733, doi:10.1002/jrs.1250250737.

232. Nielsen, A.S.; Batchelder, D.N.; Pyrz, R. Estimation of Crystallinity of Isotactic Polypropylene Using Raman Spectroscopy. *Polymer* **2002**, *43*, 2671–2676, doi:10.1016/S0032-3861(02)00053-8.